A search for signs of shape coexistence
in mid-shell tellurium isotopes

Inaugural-Dissertation

zur
Erlangung des Doktorgrades
der Mathematisch-Naturwissenschaftlichen Fakultät
der Universität zu Köln

vorgelegt von

Franziskus Graf von Spee
aus Hamburg

Köln 2024

Abstract

In this work, the structure of mid-shell Te isotopes are investigated. Based on the level schemes, these nuclei seem to be well described by a vibrational model. On the other hand, shape coexistence is suspected, but not firmly established on the basis of experimental data. The nature of the 0_2^+ state of these nuclei plays a key role in this discussion as it is the candidate state for the ground state of the intruding configuration. Thus special attention was payed to the properties of these states in this work.

The experiments presented here are all carried out at the FN Tandem accelerator at Cologne but different reaction mechanisms and experimental methods are used. Recoil Distance Doppler-shift experiments using (^{12}C,^{8}Be) α-transfer reactions on tin targets are performed to determine the lifetimes of low-lying states in tellurium isotopes. This is the first time such reactions are used to populate excited states in mid-shell Te isotopes and thus also the spectroscopic results are presented in detail. It is shown that many low-lying and low-spin states are populated in such reactions. Using the (^{12}C,^{8}Be) α-transfer reaction mechanism it is possible to measure the lifetime of the 2_1^+, 0_2^+ and 2_2^+ state in ^{116}Te. Moreover, upper limits are determined for the lifetimes of, among others, the 4_1^+, 4_2^+ and 2_3^+ state. In ^{118}Te, the lifetime of the 0_2^+ state is measured and again several upper limits are determined. In ^{120}Te it is only possible to determine an upper limit of the lifetime of the 0_2^+ state. The lifetimes of the 2_1^+ and 4_1^+ states in ^{118}Te are additionally measured using a fusion-evaporation reaction. Furthermore, the β decay of ^{116}I is investigated to determine spins of excited states and multipolarities of γ-ray transitions in ^{116}Te. Here, excited 0^+ states in ^{116}Te are unambiguously identified for the first time.

From the experimental data, level schemes are built, $B(E2)$, $B(M1)$ and $\rho^2(E0)$ strengths are calculated. These values are then compared with predictions in the interacting boson model on the one hand — especially in the U(5) limit —, and with typical signatures of shape coexistence on the other hand.

Contents

Contents

Chapter 1

Introduction

The atomic nucleus is a complex object. It consists of a finite number of protons and neutrons, so called nucleons, and its properties are governed by the nucleon-nucleon interaction. The number of nucleons is typically too small to allow a statistical description of the nucleus, but often too large to be studied *ab initio*. Early on in the history of nuclear physics, it became evident that the atomic nuclei exhibit a shell structure, similar to the shell structure of the electrons surrounding the nucleus. The shell structure was successfully described for the first time by Goeppert-Mayer [1] and Jensen [2], that were able to reproduce the so-called magic numbers observed experimentally in the nuclear structure. It was also observed, that nuclei could be excited and that there were different types of excitations of nuclei: Single-particle excitations and collective excitations involving many nucleons. It was then noticed, that many nuclei show collective excitation spectra that are similar to the spectra expected from rotating or vibrating quantum objects. This has lead to the development of geometrical models by Bohr and Mottelson for the description of collective excitations [3]. In these models, the excitation depends on the shape of the nucleus: distinctions can be made between nuclei that appear spherical or deformed, and between prolate and oblate deformations. The concept of the shape of a nucleus has persisted in nuclear physics, and will also play a key role in this work. Also other models for collective excitations like the interacting boson model that is used in this work can be related to the concept of a shape of the nucleus. The idea of the shape of a nucleus was later extended by another observation. It was proposed, that different shapes can coexist within the same nucleus (see e.g. [4]), i.e. that different excited states could belong to different shapes of a nucleus. This phenomenon — later called shape coexistence — was first observed only in a few specific nuclei, but is nowadays believed to be widespread throughout the nuclide chart [5]. However, the unambiguous identification of shape coexistence has proven to be challenging in many cases.

In this work, experiments are presented that search for signs of shape coexistence in mid-shell tellurium isotopes. At first glance, these nuclei seem to be well described by a vibrational model, but also shape coexistence is suspected to play a role. Thus before going into the details of the nuclear structure of mid-shell Te isotopes, two short introductions are given. In the first introduction, the interacting boson model is presented, that is suited to describe collective excitations of vibrational nuclei. Then, the concept of shape

coexistence is introduced paying special attention to the experimental evidences of this phenomenon.

1.1 Introduction to the interacting boson model

The interacting boson model (IBM) was developed in the 1970's by Arima and Iachello [6–9] to describe the collective structure of even-even nuclei. This approach uses the assumption, that all $2N$ valence nucleons in a nucleus are coupled pairwise to N bosons. In the IBM-1, no distiction is made between protons and neutrons. In the simplest version, the bosons can have angular momentum $L = 0$ or $L = 2$ and are hence called s or d bosons, respectively. Despite its rather simplifying approach, the IBM is able to describe properties of a large variety of nuclei along the nuclide chart and is widely used.

The IBM-1 uses the second quantization with six creation operators $s^\dagger, d_l^\dagger$ and annihilation operators $s = \tilde{s}, d_l = (-1)^l \tilde{d}_l$, with l representing the magnetic substate of the d boson that can take integer numbers with $-2 \leq l \leq 2$. A general hamiltonian of the IBM-1 that conserves the boson number N can be expressed in the following way [10, 11]:

$$\hat{H} = \epsilon \hat{n}_d + c_1 \hat{L} \cdot \hat{L} + c_2 \hat{Q}^\chi \cdot \hat{Q}^\chi + c_3 \hat{T}_3 \cdot \hat{T}_3 + c_4 \hat{T}_4 \cdot \hat{T}_4, \tag{1.1}$$

where

$$\hat{n}_d = \sum_m d_m^\dagger d_m$$
$$\hat{L}_m = \sqrt{10}(d^\dagger \times \tilde{d})_m^{(1)}$$
$$\hat{Q}_m^\chi = (s^\dagger \times \tilde{d} + d^\dagger \times \tilde{s})_m^{(2)} + \chi(d^\dagger \times \tilde{d})_m^{(2)}$$
$$\hat{T}_{3m} = (d^\dagger \times \tilde{d})_m^{(3)}$$
$$\hat{T}_{4m} = (d^\dagger \times \tilde{d})_m^{(4)}.$$

Transition strengths can be calculated with the help of the transition operators. The E2 transition operator is given in the Consistent-Q formalism [11] as

$$\hat{T}_{E2} = e \, Q_m^\chi, \tag{1.2}$$

where e denotes the effective charge of the boson.

It is useful to take a closer look at the algebraic properties of the IBM. The 36 products of creation and annihilation operators form a U(6) Lie algebra. This U(6) Lie algebra can

be decomposed in subalgebrae in three different ways (compare e.g. [10] chapter 2.3):

$$U(6) \supset U(5) \supset O(5) \supset SO(3)$$
$$U(6) \supset O(6) \supset O(5) \supset SO(3)$$
$$U(6) \supset SU(3) \supset SO(3)$$

where each subalgebra chain is characterized by a different set of quantum numbers. Associated with each (sub)algebra are Casimir operators that commute with every member of the algebra. Hamiltonians that can be written entirely in terms of Casimir operators of one algebra chain are analytically solvable. Nuclei that can be described with such a Hamiltonian are said to exhibit a dynamical symmetry. The dynamical symmetries are typically denominated by the first subalgebra of the corresponding subalgebra chain, i.e. U(5), O(6), and SU(3). Additionally it was noted, that each of the dynamical symmetries can be associated with a different geometrical interpretation: The U(5) limit can be utilized to describe vibrational nuclei, which usually are located close to shell closures [7]. The SU(3) limit is suited to describe rotational and deformed nuclei, that are mainly located far away from closed shells [8]. The O(6) limit is connected to nuclei exhibiting a γ-unstable form of deformation that can be found in transitional regions [9]. This simplifies a physical interpretation of IBM-1 Hamiltonians significantly.

There are also several extensions of the interacting boson model. It is for example possible in the spdf-IBM-1 to allow the bosons to take angular momentum 1 or 3 that are then called p bosons or f bosons. For the description of even-odd and odd-even nuclei, the interacting boson-fermion model (IBFM) is used where a fermion is coupled to the bosonic configuration. If a distinction is made between bosons consisting of proton pairs and bosons consisting of neutron pairs, the model is called IBM-2.

After the development of the IBM, considerable effort was made to find good examples of nuclei, that exhibit one of the dynamical symmetries of the IBM-1 (compare for the U(5) dynamical symmetry e.g. [12]). Therefore, experimental observables like level schemes and B(E2) values need to be measured, that allow a distinction between the dynamical symmetries. In the vicinity of the Z=50 shell closure, the Te (Z=52) and Cd (Z=48) isotopes have been considered for a long time as good examples of nuclei exhibiting a U(5) symmetry. In the following, the vibrational U(5) limit of the IBM-1 is thus presented.

1.1.1 The U(5) limit

A general U(5) hamiltoninan can be written in the form of the Casimir operators of the U(5) algebra chain (compare Ref. [10] chapter 2.5):

$$\hat{H} = \epsilon C_1[U(5)] + a_1 C_2[U(5)] + \beta C_2[O(5)] + \gamma C_2[O(3)] \tag{1.3}$$
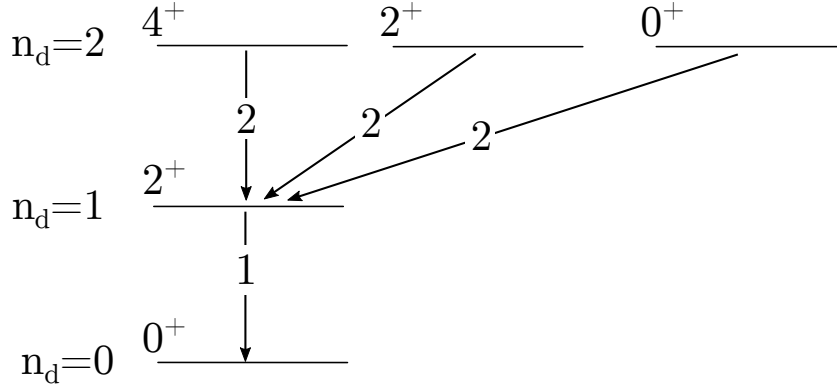
Figure 1.1: Level scheme in the U(5) limit up to the two phonon triplet. The numbers on the transition arrows indicate the $B(E2)$ values relative to the $B(E2; 2_1^+ \rightarrow 0_1^+)$ value. The values are calculated for $\lim_{N \rightarrow \infty}$.

where

$$C_1[U(5)] = \hat{n}_d$$

$$C_2[U(5)] = \hat{n}_d(\hat{n}_d + 4)$$

$$C_2[O(5)] = 2\left(\frac{\hat{L} \cdot \hat{L}}{10} + \hat{T}_3 \cdot \hat{T}_3\right)$$

$$C_2[O(3)] = \hat{L} \cdot \hat{L}.$$

The eigenvalues can be calculated from the expectation values of the Casimir operators and depend on the quantum numbers associated with each Casimir operator:

$$E(N, n_d, \nu, L) = \epsilon n_d + a_1 n_d(n_d + 4) + \beta\nu(\nu + 3) + \gamma L(L + 1) \tag{1.4}$$

These quantum numbers can take only certain, discrete values. For example, n_d can take integer values between 0 and N. All possible values for the other quantum numbers are given in chapter 2 of Ref. [10]. In reality, the eigenvalues are typically dominated by the first term ϵn_d leading to multiplets of states that are denominated by the value of n_d. These multiplets are characteristic for vibrational U(5) nuclei. A U(5) level scheme up to the two-phonon triplet is shown in Fig. 1.1. A first step at the identification of a nucleus that possibly exhibits a U(5) symmetry is thus the identification of candidate states for the one and two-phonon states. The two-phonon triplet, consisting of the $0_2^+, 2_2^+$, and 4_1^+ state should lie at an excitation energy that is approximately twice the excitation energy of the 2_1^+ — i.e. $E(4_1^+)/E(2_1^+) = R_{4/2} \approx 2$ — and the energy spreading is ideally small (compare Ref. [12]).

Another key indicator comes from the $E2$ transition strengths. Analogous to the case of the excitation energies, it is possible to define ratios of the transition strengths (compare chapter 2.6 of Ref. [10]):

$$B_{4/2} = \frac{B(E2; 4_1^+ \to 2_1^+)}{B(E2; 2_1^+ \to 0_1^+)}, \; B_{2/2} = \frac{B(E2; 2_2^+ \to 2_1^+)}{B(E2; 2_1^+ \to 0_1^+)}, \; B_{0/2} = \frac{B(E2; 0_2^+ \to 2_1^+)}{B(E2; 2_1^+ \to 0_1^+)} \quad (1.5)$$

In the U(5) limit, all three ratios are given by

$$B_{4/2} = B_{2/2} = B_{0/2} = 2\frac{N-1}{N}. \quad (1.6)$$

The ratios will approach 2 for large boson numbers N. In the other symmetries, the ratios are in general smaller, especially the $B_{0/2}$ value, which is predicted to be 0 for both a O(6) symmetry and a SU(3) symmetry. Measurements of $B(E2)$ values between the lower lying states are thus a sensitive test for nuclei where a U(5) symmetry is suspected.

1.2 Experimental evidences for shape coexistence
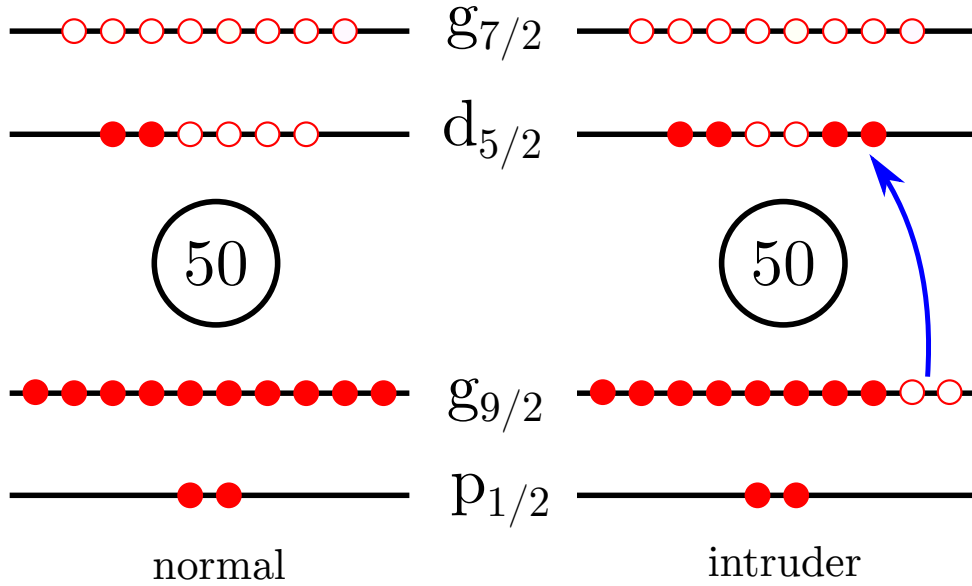
Figure 1.2: Schematic depiction of possible proton $2p - 2h$ excitations in Te isotopes. On the left-hand side, protons are in the normal configuration. On the right-hand side, a proton pair is moved across the $Z = 50$ shell closure from the $1g_{9/2}$ shell to the $2d_{5/2}$ shell. This configuration is called intruder configuration.

The concept of a nuclear shape plays a major role for collective models of nuclei. In collective models, excited states of a nucleus can be understood as rotational or vibrational excitations of a spherical or deformed nucleus [13]. The different excitations depend thus on the shape of the nucleus and different shapes lead to different excitation spectra. The

shape of the nucleus arises from the microscopic configuration of the nucleus. By changing the microscopic configuration, different shapes can appear not only for different nuclei but also within the same nucleus [5]. This phenomenon is known as shape coexistence. Unfortunately, there is no consistent definition of shape coexistence. In general, shape coexistence is attributed to nuclei where, preferably at low energies, different excited states arise from different distinct shapes. This can often be achieved through promotion of pairs of nucleons across a major shell. This results in the creation of $2p - 2h$ excitations that can have a different collective structure than the normal configuration and hence lead to shape coexistence. A schematic depiction of possible $2p - 2h$ excitations in Te is shown in Fig. 1.2.

Experimentally, it is not always easy to establish shape coexistence in a nucleus. Many single data points can also be explained through other possible phenomena. Therefore it is often necessary to collect multiple different experimental evidences ("fingerprints [5]") of shape coexistence. Over the last decades, several reviews have been published that summarize the efforts to understand and detect shape coexistence [5, 14, 15]. For a more complete picture of shape coexistence and the manifestation of shape coexistence throughout the nuclide chart, the reader is referred to these review papers. In the following, some key experimental evidences for shape coexistence that play a role in this work are summarized:

Figure 1.3: Energy systematics of intruder states in Hg isotopes attributed to $2p - 2h$ excitations. Figure adopted from [16]. Blue color is used to mark states associated with the normal configuration, while red color is used for states associated with the intruder configuration.
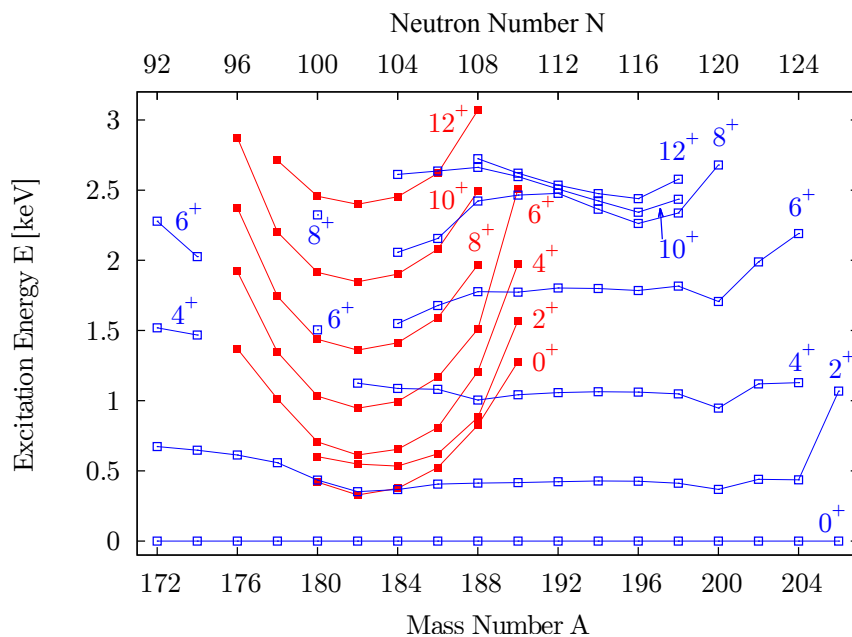
- Energy systematics of intruder configuration

Typically, $2p - 2h$ excitations are found in the vicinity of closed shells. Moving along a closed proton (neutron) shell, the excitation energy of these $2p - 2h$ states depends on the number of valence neutrons (protons) and will become lower with increasing numbers of valence neutrons (protons). This leads to typical parabolic energy systematics of intruding structures built on top of $2p - 2h$ states that exhibit a minimum at neutron (proton) mid-shell along isotopic (isotonic) chains with respect to the normal configuration [17]. A clear example of this behaviour is observed in the Hg isotopes, where the energy minimum for the intruding configuration lies close to mid-shell $N = 104$ [16] (see Fig. 1.3).

- Excited 0^+ states and E0 transition strengths

  In even-even nuclei, the ground states of both the normal and intruder configurations are 0^+ states. Therefore, the presence of an intruding structure in a nucleus should naturally result in additional excited 0^+ states at low energies. Identifying excited 0^+ states is crucial when investigating nuclei for possible shape coexistence [18]. Another powerful piece of evidence are large E0 transition strengths between 0^+ states. The E0 transition strength between two 0^+ states is positively correlated with the difference of the mean-square radii of the nucleus of final and initial state [19]. Since the intruding configuration and the normal configuration can have different mean-square charge radii, a large E0 transition strength can again be an indicator of shape coexistence. In fact, Kibedi *et al.* [20] state that the largest measured $\rho^2(E0)$ values were all measured in nuclei which presumably exhibit shape coexistence.

- In-band transition strengths

  For a collective intruding structure, the in-band transitions are expected to exhibit collective behaviour and accordingly, the transition strengths of in-band transitions should be strong. A measurement of absolute transition strengths can therefore help to identify intruding structures [5]. It is also possible to construct the distinct deformations of the respective structures with the help of the absolute transition strengths. As an example, recently multiple shape coexistence was discovered in ^{110,112}Cd with the help of absolute $B(E2)$ strengths of cascades of transitions feeding excited 0^+ states [21].

As mentioned already above, this list of possible indicators of shape coexistence is not complete. Many more could be named, for example partial cross sections for the intruding and normal configuration in direct reactions or magnetic moments of states belonging to different configurations. Many of these quantities are difficult to obtain and will not play a larger role in this study. A final observation in this context is that nuclei associated with shape coexistence are often not well described by models that do not include shape coexistence as more and more experimental data are gathered. An example
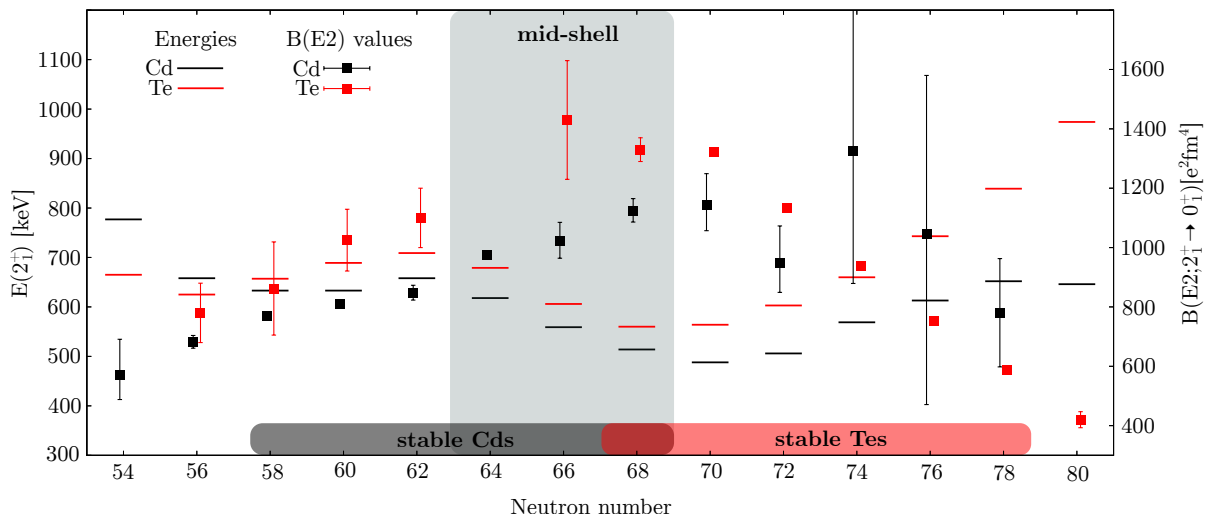
Figure 1.4: Systematics of the excitation energy of the first excited 2^+ states and of $B(E2; 2_1^+ \rightarrow 0_1^+)$ values in Cd and Te isotopes between N=50 and N=82. For context reasons, neutron numbers of stable Cd or Te isotopes and the mid-shell region are marked.

of this phenomenon are the mid-shell Cd isotopes that were initially believed to exhibit a vibrational structure, but additional 0^+ and 2^+ states found in the vicinity of the candidate two-phonon triplet could not be described with such a model without additional assumptions (compare Ref. [5]).

1.3 The nuclear landscape for mid-shell tellurium isotopes

The tellurium isotopes at $Z = 52$ lie just two protons above the proton shell closure of tin at $Z = 50$. In this region, some of the elements with the highest number of stable isotopes can be found. This makes the region very suitable for studies along isotopic chains. Stable Te isotopes range from ^{120}Te with just two neutrons more than neutron-midshell at $N = 66$ to ^{130}Te just four neutrons away from the neutron shell closure at $N = 82$. In this study, ^{116,118,120}Te isotopes were investigated, which are located in the proximity of the neutron midshell at ^{118}Te. With the exception of ^{120}Te, these isotopes are not stable and the very low natural abundancy of ^{120}Te means, that experimental data on these Te isotopes are rather difficult to obtain, as well.

The Cd isotopes lie at $Z = 48$ mirroring the Te isotopes with respect to the Sn proton shell closure. This fact suggests that the nuclear structure of mid-shell Te isotopes should show at least some degree of similarity to the nuclear structure of mid-shell Cd isotopes. A comparison of excitation energies and $B(E2)$ values in mid-shell Te and Cd isotopes shown in Fig. 1.4 supports this simple picture. The excitation energies of the 2_1^+ states and the $B(E2; 2_1^+ \rightarrow 0_1^+)$ values lie in the same range and evolve similarly for the Cd and Te isotopes. The mid-shell ^{112,114,116}Cd isotopes are all stable and therefore experimentally
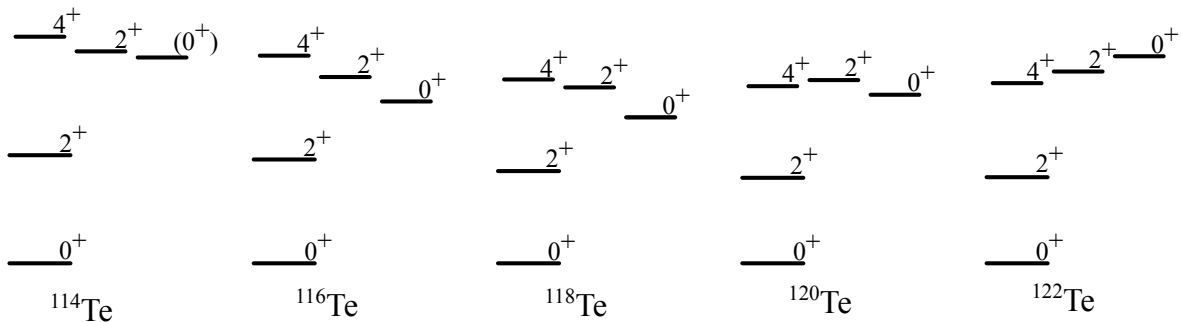
Figure 1.5: Level schemes of low-lying states in mid-shell Te isotopes. Shown are all known levels up to the supposed two-phonon triplet. Data taken from [26–30].

easier to study. Consequently, experimental data on mid-shell Cd isotopes are much more abundant than experimental data on mid-shell Te isotopes. It makes therefore sense to have a closer look at the nuclear structure of mid-shell Cd isotopes before investigating the related Te isotopes.

The mid-shell Cd isotopes have been considered as examples of nuclei exhibiting a U(5) symmetry many times. For instance, in the original paper on the U(5) limit by Arima and Iachello, the nucleus ^{110}Cd is given as an example [7]. In their systematical search for nuclei exhibiting a U(5) symmetry, Kern *et al.* [12] fit the level energies of excited states of several mid-shell Cd isotopes with a U(5) Hamiltonian (compare Eq. (1.4)) finding in some cases good agreement. In ^{118}Cd, the first observation of a full three-phonon quintuplet was claimed [22]. But the nuclear structure of mid-shell Cd isotopes is more complicated. Very early on, additional 0^+ and 2^+ states were discovered in the vicinity of the supposed two phonon triplet [23, 24]. These were attributed to intruder configurations from $2p-2h$ excitations. The experimental evidence for these intruder structures increased over time and the presence of intruder structures in Cd isotopes is undisputed nowadays [5]. In some Cd isotopes, even multiple intruding structures have been identified [21]. It is however unclear, whether the underlying normal configuration can still be viewed as a U(5) symmetry [25] or whether the vibrational picture is insufficient [21].

In Fig. 1.5, low-lying states of mid-shell Te isotopes are presented. For context, also ^{114}Te and ^{122}Te are shown, even though the study of these nuclei is not part of this work. Similarly to the Cd isotopes, the $R_{4/2}$ ratio is in all cases relatively close to the vibrational limit of 2 and the 4_1^+, 2_2^+, 0_2^+ states provide candidate states for the two-phonon triplet of a U(5) nucleus. For ^{118,120,122}Te, a description in the U(5) limit was indeed performed in Refs. [31–33].

On the other hand, the discovery of intruder states in Cd and Sn isotopes has lead to the conclusion, that such intruder states should exist in mid-shell Te isotopes as well [34]. First candidates of intruder states were found in the 0_2^+ states, as their excitation energy

depends on the neutron number and exhibits a clear minimum at mid-shell $N = 66$ [34]. This interpretation contradicts the previous view of the 0_2^+ states as members of the two-phonon triplet in a vibrational-like structure. A clarification of the nature of the 0_2^+ states thus seems to be critical for a better understanding of the structure of mid-shell Te isotopes.

A clear identification of additional candidate states belonging to an intruder structure in Te isotopes has proven to be difficult [5]. This may be due to two factors: first, spectroscopic data for mid-shell Te isotopes are relatively limited compared to the more extensive data available for mid-shell Cd and Sn isotopes [5]; second, mixing effects of normal and intruder configurations are suspected to play a significant role in these Te isotopes [35] that might obscure the typical signature of intruder states. In fact, *Rikovska et al.* [35] performed an IBM-2 calculation including configuration mixing of the normal configuration with an intruder configuration that was able to reproduce the excitation energies and relative $B(E2)$ values in mid-shell Te isotopes known at the time. It is clear that in this region — especially in the neutron-deficient Te isotopes — further spectroscopic data are needed to clarify the possible presence of intruder states. For instance, a 0_2^+ state has not yet been unambiguously identified in ^{114,116}Te [26, 27].

Differentiating between the possible explanations for the low-lying excited states in mid-shell Te isotopes is difficult using only excitation energies of excited states. Valuable insight can be gathered also from absolute transition strengths. In a simple U(5) pattern the ratios $B_{4/2}$, $B_{2/2}$ and $B_{0/2}$ (compare Sec. 1.1.1) should all be close to 2. The measured $B_{4/2}$ ratios in ^{118,120,122}Te agree with this picture [33, 36–38] while in ^{114}Te, the measured $B_{4/2} < 1$ is difficult to interpret [39] and not compatible with any collective model. Data on the $B_{2/2}$ ratios in the mid-shell Te region [31, 33, 37] are less abundant and, in some cases, ambiguous. Data on the $B_{0/2}$ ratios have not been published for any isotope so far, except for ^{118}Te, where the half-life value of $t_{1/2}(0_2^+) = 55(45)\,\mathrm{ps}$ used to calculate the $B(E2; 0_2^+ \to 2_1^+)$ value has an uncertainty of over 80% and is described as preliminary by the authors. However, $B_{0/2}$ ratios are of particular interest, as the interpretation of the 0_2^+ states as intruder states allows these ratios to take values different from 2, with the exact value depending on the mixing of the intruder structure with the normal configuration [18]. Additional insights into possible intruder states can be gained from the absolute strengths of transitions to candidate intruder states, which are expected to be enhanced. Thus, the elevated $B(E2, 2_3^+ \to 0_2^+)$ values in ^{118,122}Te have supported the interpretation that the 2_3^+ states are collective states built on top of an intruding 0_2^+ state [5, 31, 33]. Further measurements of in-band transition strengths for candidate intruder structures in mid-shell Te isotopes are currently lacking.

Another piece of evidence relevant for the nuclear structure are the $\rho^2(E0)$ values, as enhanced $\rho^2(E0)$ values are often linked to shape coexistence and the mixing of intruder and normal configurations. But data on $\rho^2(E0; 0_2^+ \to 0_1^+)$ in mid-shell Te isotopes are

again limited, with the only available information coming from the preliminary half-life value of $t_{1/2}(0_2^+) = 55(45)\,\mathrm{ps}$ mentioned earlier.

It is thus the scope of this work to improve the understanding of the nuclear structure of mid-shell Te isotopes, with particular emphasis on identifying potential intruder states. To this end, both new spectroscopic measurements and new measurements of absolute transition strengths, along with $\rho^2(E0)$ values, are conducted. Special attention is given to the 0_2^+ states in this region, which are considered candidate ground states for the possible intruder configuration.

Chapter 2

Experimental observables and methods

In the previous chapter, different characteristics of some phenomena of nuclear structure are presented that play a role in mid-shell Te isotopes. It is the task of experimenters, to detect these characteristics through experiments. Therefore, suitable experimental observables have to be found. In some cases, this is relatively straight forward: for example, the level energies of excited states can in most cases be reconstructed from γ-ray spectra and γ-γ-coincidence data observing the decay of the excited state. In other cases, the quantities cannot be measured as directly: Conclusions about spin and parity of initial and final state of a γ-ray transition can be drawn from the anisotropic distribution of emitted γ rays. And in the case of absolute transition strengths, multiple experimental observables are needed to calculate the quantities of interest. Often, $B(EL/ML)$ values are used that are directly related to the reduced matrix element between initial and final state of an EL/ML transition and are given by

$$B(EL/ML; I_i \rightarrow I_f) = \frac{1}{2I_i + 1} \langle \Psi_f || \hat{EL}/\hat{ML} || \Psi_i \rangle^2. \tag{2.1}$$

Experimentally, $B(EL/ML)$ values can be determined from the level lifetime τ, the branching ratio b between the different depopulating transitions, the inner conversion coefficient α_{IC}, and the γ-ray energy E_γ via

$$B(EL; I_i \rightarrow I_f) = \frac{L((2L+1)!!)^2}{8\pi(L+1)} \frac{b}{1+\alpha_{IC}} \left(\frac{\hbar c}{E_\gamma}\right)^{(2L+1)} \frac{\hbar}{\tau}, \tag{2.2}$$

where $B(EL)$ values are given in $e^2 b^L$. $B(ML)$ values can be calculated in a similar way in units of $\mu_N^2 b^{L-1}$. If the γ-ray connecting initial and final state can have multiple different multipolarities, the $B(EL)$ and $B(ML)$ value also depend on the mixing ratio δ that is defined as

$$\delta^2 = \frac{T(L+1)}{T(L)}, \tag{2.3}$$

where $T(L)$ is the transition probability for a γ ray with multipolarity L. In this case, the branching ratio b in Eq. (2.2) is replaced by a partial branching ratio

$$b_L = \frac{b}{1 + \delta^2} \qquad \text{or} \qquad b_{L+1} = \frac{b\delta^2}{1 + \delta^2}.$$

To quantify the strength of an $E0$ transitions, usually $\rho(E0)^2$ values are given that are defined via

$$\rho(E0) = \frac{\langle \Psi_f || \hat{E0} || \Psi_i \rangle}{e R_0^2}, \tag{2.4}$$

where R_0 is the radius of the nucleus. This value can be calculated using a known competing $E2$ transition via the equation

$$\rho(E0)^2 = \frac{X(E0/E2)B(E2)}{e^2 R_0^4} \tag{2.5}$$

where the dimensionless ratio $X(E0/E2)$ [40] can be determined from electron spectroscopy.

In the following sections, methods for the experimental determination of level lifetimes and analysis of angular correlations are presented.

2.1 Recoil Distance Doppler-shift method

The recoil distance Doppler-shift technique (RDDS) is a method to measure the lifetimes of excited states in nuclei in the picosecond range. A detailed description of the RDDS technique and related topics is given in Ref. [41]. For this method, the nucleus of interest is produced in a nuclear reaction of a particle beam with a sufficiently thin target foil. The nucleus of interest then leaves the target foil and recoil in vacuum towards a stopper foil placed at a well defined distance x, where the nucleus is stopped. The target-to-stopper distance is adjustable and is controlled by a so-called plunger device. The nucleus is desirably produced in an excited state and decays via γ-ray cascades to the ground state. Around the target chamber, γ-ray detectors are placed at angles Θ with respect to the beam axis. The detected γ rays stemming from the nucleus of interest will be Doppler-shifted in energy, if the γ decay occurs before the nucleus is stopped in the stopper foil, and unshifted for decays at rest inside the stopper foil. The energy E_γ^s of the shifted γ ray depends on the unshifted energy E_γ^u, on the angle θ between the momentum of the recoiling nucleus and the momentum of the γ ray and on the velocity $\beta = v/c$ of the recoiling nucleus and is given by

$$E_\gamma^s = E_\gamma^u \frac{\sqrt{1-\beta^2}}{1-cos(\theta)\beta}.$$ (2.6)

Note that the angle θ between the momentum of the recoiling nucleus and the momentum of the emitted γ ray and the angle Θ between the beam axis and the γ-ray detectors are very similar in most cases. If the γ-ray detectors are placed at angles different from 90° with respect to the beam axis, observed γ-ray transitions in the nucleus of interest have thus two components, a shifted flight component I^{fl} and an unshifted stop component I^{st}. For a decaying transition of an excited state i, the ratio of the stop component to the total intensity is called decay curve $R(t)$ and depends on the flight time t of the nucleus of interest:

$$R_i(t) = \frac{I_i^{st}(t)}{I_i^{st}(t) + I_i^{fl}(t)}$$ (2.7)

For very short flight times, i.e. much shorter than the lifetime of the state i, nearly all decays will happen in the stopper and thus $\lim_{t\to 0} R_i(t) = 1$. For long flight times, longer than all involved lifetimes, most decays will happen in flight and thus $\lim_{t\to\infty} R_i(t) = 0$. By taking measurements at many different target-to-stopper distances, the decay curve can be sampled.

It is in general also possible to use a degrader foil instead of a stopper foil that only reduces the kinetic energy of the nucleus of interest by a certain amount without stopping it completely. This possibility was not used in this work and will not be discussed here. Further information is given in Ref. [41].

2.1.1 The capacitance method and absolute foil separation measurement

In an RDDS experiment, it is essential to have reliable information on the target-to-stopper distance x. To ensure a well defined target-to-stopper distance, it is important that the target and stopper foil are smooth surfaces and that target and stopper foil are aligned in parallel. Therefore, target and stopper foil are usually stretched over cones that will be mounted in the plunger device (compare Ref. [41]). The position of the cones can be adjusted manually to align target and stopper foil. It is useful to distinguish between relative target-to-stopper distances and absolute target-to-stopper distances. This distinction is made, because in most cases the relative distances can be determined with higher precision, while the absolute distances hold more information.

To determine relative distances, it is sufficient to monitor the position of the movable foil, which is usually the target foil. In case of the Cologne coincidence plunger device (see Sec. 3.2), the position of the target foil is monitored with a magnetic transducer as well as an intrinsic measurement in the linear actuator. In this way, a relative distance

measurement can be performed. However, during the experiment, the heating of the target usually leads to thermal expansion of the plunger apparatus and the same motor position will thus in general not be the same relative distance between the two foils. These deviations can be corrected for with the capacitance method [41, 42]. A pulsed voltage signal on one foil will induce a small voltage on the other foil. The magnitude of this signal depends on the capacitance between the foils which in turn depends on the distance of the two foils. A reference measurement (usually called distance calibration) of the induced voltages at certain relative distances before the start of the experiment is used to keep the relative distances constant during the measurement, by keeping the induced voltage signal constant. This distance calibration is usually performed using the magnetic transducer. During the measurement, only the voltage signal in combination with the distance calibration is used to monitor the target-to-stopper distance.

To determine absolute distances, the minimum separation of the two foils needs to be determined. The point of minimum separation is usually reached at the point of electrical contact, which can be determined by driving the target foil closer to the stopper foil, until the induced voltage signal shows, that the two foils are in electrical contact. This usually corresponds to a mean separation of target and stopper foil of some micrometers due to surface roughness. For a more precise measurement, the fact can be used that if the target-to-stopper distance is much smaller than the foil diameter, the induced voltage is anti-proportional to the absolute distance of the foils ($1/V \propto R$). Deviations from the linear behaviour arise from the finite diameter of the foils and from stray capacitances in the target chamber, mostly between the foil holding structure and outer parts of the foil outside the streched area. The distance between the electrical contact and the mechanical contact (hereafter called offset) can be estimated by a linear extrapolation of the dependency of $1/V$ on the distance towards $1/V = 0$. Such an extrapolation is shown in Fig. 2.1 using the data from the ^{114}Sn(^{12}C,^{8}Be)^{118}Te α-transfer experiment as an example. The offset is given by the distance between the last measurement point of the distance calibration and the intersection of the linear extrapolation with the x-axis. For this extrapolation, stray capacitances can be taken into account with a constant value that is added to the measured voltage (left hand side of Fig. 2.1). For more details, the reader is referred to Refs. [41–43].

2.1.2 Alpha-transfer experiments and the RDDS method

One of the main goals of this work is the measurement of lifetimes of low-lying yrast and off-yrast states in mid-shell ^{116,118,120}Te isotopes with the RDDS technique. In order to carry out such measurements successfully, a suitable nuclear reaction must be found that produces these nuclei and populates the states of interest. Ideally, the beam required for this should be available at the FN tandem accelerator in Cologne. Unfortunately,
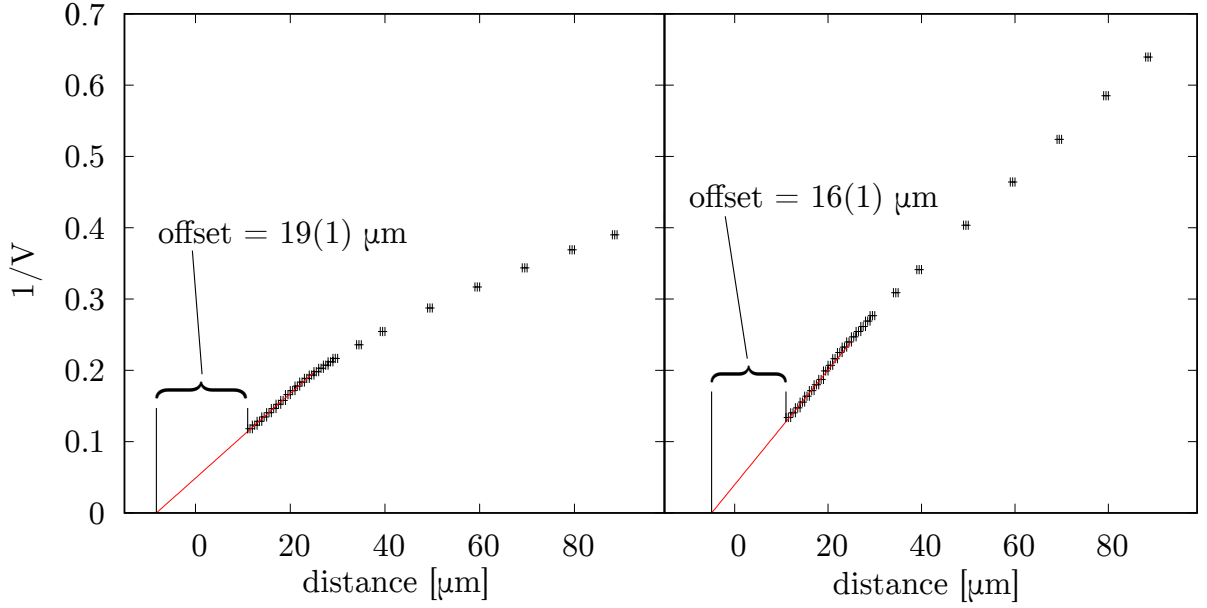
Figure 2.1: Distance calibration used for the α-transfer experiment ^{114}Sn(^{12}C,^{8}Be)^{118}Te. On the left hand side, the original data are plotted; on the right hand side, a constant modification of the induced voltage was introduced, to take into account the holding and stray capacitance. The distance calibration extends to 500 µm. Here, a shorter range is shown to make the determination of the offset more visible. In green the linear extrapolation of the distance to small distances is shown. The distance between the last measuring point and the intersect of the extrapolation with the x-axis represents the offset.

all experiments carried out so far on ^{116,118,120}Te did not use reactions that would be suitable for such an experiment. Fusion-evaporation reactions with ^{12}C or heavier beams used e.g. in Refs. [36, 44, 45] provide enough recoil velocity, but populate mainly yrast states and do not populate the low-lying off-yrast states of interest. These states were observed only in reactions with lighter beams or through population in β decay used e.g. in Refs. [32, 46–48], but such experiments do not provide the necessary recoil velocities for an RDDS measurement.

Instead, in this work (^{12}C,^{8}Be) α-transfer experiments with ^{112,114,116}Sn targets were used to produce the nuclei of interest. Such reactions have not been performed to populate excited states in Te isotopes, but have been used in other regions of the nuclide chart (compare e.g. Ref. [49]). The chosen (^{12}C,^{8}Be) α-transfer reaction mechanism has the disadvantage that the cross sections for the production of the nuclei of interest of such reactions cannot be as high as the cross sections of some fusion-evaporation reactions for the same nuclei of interest. However, this reaction mechanism also offers some decisive advantages. In transfer reactions it is usually possible to detect the beam-like fragments (BLFs). This serves a dual purpose. The data are cleaned from other reactions happening

at the same time and the kinematics are fixed — i.e. precise information on the recoil velocity of the nucleus of interest is obtained. A detection of BLFs under backward angles selects kinematics with higher recoil velocities of the corresponding target-like fragments (TLFs) and ensures that the corresponding TLFs move in the direction of the stopper foil.

Another advantage of the α-transfer reaction mechanism for RDDS measurements lies in the population pattern. Typically, in α-transfer reactions only relatively low-lying and low-spin states are populated while in fusion-evaporation reactions, that are often used for RDDS measurements, higher-lying and higher-spin states are populated. The population pattern of fusion-evaporation reactions typically leads to slower feeding times. In some cases, the slow feeding makes a lifetime analysis of lower-lying states that are fed via delayed feeding impossible. On the contrary, a typical population pattern of α-transfer reactions leads to fast feeding times. This means that it is less likely that large feeding corrections are needed in a lifetime analysis and less likely that the lifetime information of lower-lying states is lost due to a feeding state with a long lifetime. A good example of this behavior can be seen later in Sec. 4.2 where two RDDS experiments on ^{118}Te are performed — one using a fusion evaporation reaction and one using an α-transfer reaction (see also Fig. 4.2).

To perform (^{12}C,^{8}Be) α-transfer experiments that produced ^{116,118,120}Te isotopes, a beam of ^{12}C and ^{112,114,116}Sn targets were needed. The beam of ^{12}C is available at the FN Tandem accelerator in Cologne. The beam energy was chosen just below the Coulomb barrier at around 44 MeV to ensure relatively large cross sections but avoid large cross sections for fusion-evaporation reactions on tin. Suitable ^{112,114,116}Sn targets for an RDDS experiment can be manufactured but during this work problems arose from exactly these targets. The next section is dedicated to these tin targets and the problems encountered.

2.1.3 A note on the target thickness of evaporated tin targets

To perform a successful RDDS experiment, multiple experimental requirements have to be met by the chosen reaction that populates the nucleus of interest and by the experimental setup. Plunger target foils need to be robust enough to be stretched over the target cone. The stretching of target and stopper foil ensures that the two foils can be brought to controlled, small target-to-stopper distances. On the other hand, the target foil needs to be thin enough, that none of the recoiling nucleus of interest are stopped already within the target itself. Self-supporting target foils used for RDDS experiments at the FN Tandem accelerator at the University of Cologne typically have a thickness of about $1\,\mathrm{mg/cm^2}$ to ensure these criteria. These targets are usually produced by rolling. If a target material is not suitable for rolling or a self-supporting target foil cannot be produced for other reasons, a second option lies in evaporated targets. In this case, the target material is evaporated on a suitable supporting foil that is facing the beam in the experiment. Supporting foils should be able to be stretched over the target cone and the material of the supporting

foil should be chosen so that possible reactions on that foil do not hamper the reaction of interest on the target material. Typical materials for supporting foils (so called "frontings") are for example tantalum or gold. The thickness of the layer of evaporated target material is calculated from the mass difference before and after the evaporation process dividing by the area onto which the material was evaporated. The target thickness is then used to calculate expected energy losses of the beam and the recoiling nucleus of interest. This allows to estimate the velocity of the recoiling nucleus of interest after it leaves the target foil which is needed for the RDDS analysis. Such estimates are routinely performed during the planning of an RDDS experiment to ensure a successful experiment. They can be performed for example with the LISE++ program [50].

In this work, $(^{12}\text{C},^8\text{Be})$ α-transfer reactions on tin targets were extensively used to investigate excited states in tellurium isotopes with the RDDS method. For these experiments, evaporated tin on tantalum targets were used. The kinematics of these reactions were calculated before the experiments: the slowest recoiling nuclei stem in general from a reaction directly at the front (i.e. "upstream") of the target layer with α-particles emitted at 120° with respect to the beam line, which is the maximum acceptance angle of the PIN diodes (hereafter called "solar cells") that are used for particle detection (see Sec. 3.3). The nuclei of interest then traverse the maximum distances through the target material, leading to maximal losses of kinetic energy. For the case of a $^{112,114,116}\text{Sn}$ target, Te nuclei produced via an α-transfer reaction have a kinetic energy of about 0.077 MeV/u immediately after the reaction if the ^8Be particles are emitted at 120°. The Te nuclei then lose energy in the tin target layer where the exact amount of energy lost depends on the distance travelled through the target layer. The range in tin for Te nuclei with this energy lies at about 2.0 mg/cm^2 according to LISE++ [50]. To avoid stopping in the target layer, the thickness of the target layer must thus be chosen to be significantly smaller than 2.0 mg/cm^2.

Two experiments that are part of this thesis were performed where stopping in the target was noticed and thus unfortunately no precise lifetime values could be extracted from the data. The first one used the $^{114}\text{Sn}(^{12}\text{C},^8\text{Be})^{118}\text{Te}$ α-transfer reaction, the second reaction was the $^{116}\text{Sn}(^{12}\text{C},^8\text{Be})^{120}\text{Te}$ α-transfer reaction. The nominal thicknesses of the ^{114}Sn and ^{116}Sn targets were 0.8 mg/cm^2 and 0.5 mg/cm^2, respectively. In both cases, a tantalum foil with a thickness of around 1.5 mg/cm^2 was used as a fronting. Even taking into account the angular spread of the target-like fragments with respect to the beam axis and uncertainties in the thickness of the tin layer of 50 %, all target-like fragments should have been able to exit the target foil. However, the spectrum shown in Fig. 2.2 demonstrates clearly for the example of ^{120}Te that stopping occurred in the target. All observed transitions in ^{120}Te show an unshifted component, even though no stopper was in place. It is likely that the reason for this phenomenon lies in the uneven distribution of tin during the evaporation process. This can lead to very different local thickness of the layer of the target material, leading to events, where the recoiling target-like nuclei are
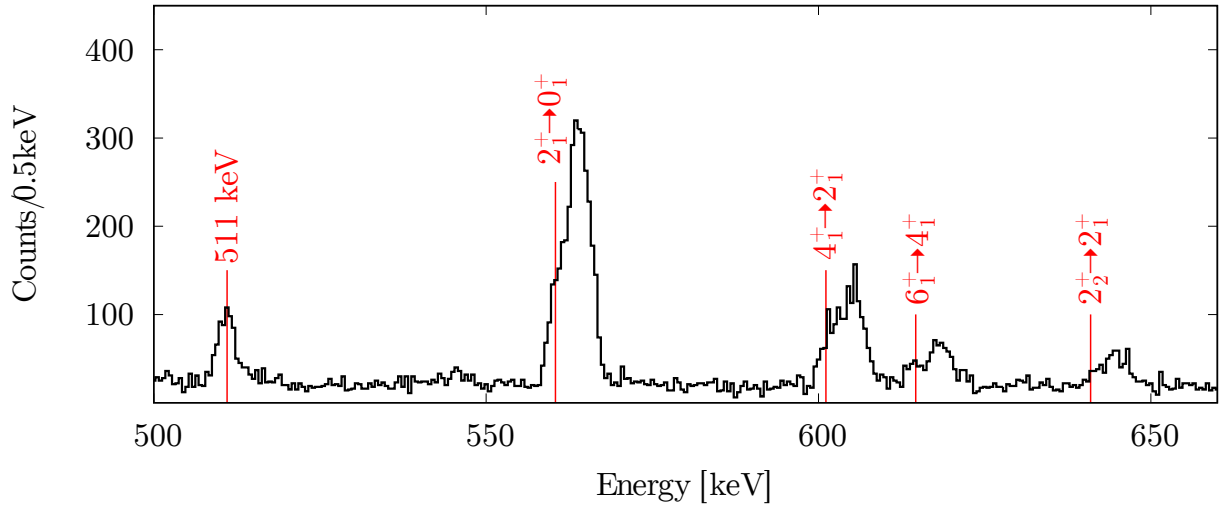
Figure 2.2: Spectrum in ^{120}Te observed in the ^{116}Sn(^{12}C,^{8}Be)^{120}Te α-transfer reaction. A gate condition is set in the solar cells for the detection of a particle. The nominal target thickness was $0.5\,\text{mg/cm}^2$ ^{116}Sn evaporated on $1.6\,\text{mg/cm}^2$ Ta. There is no stopper foil present.

stopped in the target layer.

To avoid this problem, several precautions were used for later experiments using α-transfer reactions on evaporated tin targets. During the evaporation process the temperature of the oven was adjusted to to achieve a more uniform distribution of the target material. In addition, a measurement without a stopper was carried out before each experiment to ensure that there was no stopping in the target.

2.2 Analysis methods for recoil distance Doppler-shift experiments

There are different approaches how lifetime values can be extracted from decay curves. Which of the different approaches can be used and which gives the most precise lifetime value depends on the individual situation. Here, a short overview is given on the approaches used in this work.

2.2.1 Effective lifetimes

Before the different analysis methods are presented, the concept of effective lifetimes is briefly introduced, that sometimes plays a role in RDDS experiments. The term "effective lifetime" refers to the measured lifetime in an RDDS experiment without taking into account any necessary feeding corrections. In this context, the term "real lifetime" is often used for the lifetime τ of an excited state to differentiate between the lifetime τ and the effective lifetime τ_{eff}. The effective lifetime τ_{eff} of an excited state can be calculated

using the assumption, that the excited state is populated only directly or that the feeding lifetimes are very short. Then the decay curve in Eq. (2.7) is equal to a simple exponential decay

$$R(t) = e^{-t/\tau_{eff}}. \tag{2.8}$$

This approach neglects all feeding contributions and the resulting effective lifetime of an excited state is therefore always longer than the lifetime of the same excited state. The effective lifetime is hence not a physical quantity since it depends on the feeding pattern of the specific experiment. It may also be influenced by the target-to-stopper distance used for the measurement, since the decay curve in general does not follow an exponential decay. For several reasons, it can sometimes still be useful to calculate effective lifetimes: effective lifetimes are easy to calculate during an experiment to get a first guess for a lifetime value. They can also be used to approximate feeding lifetimes. And in cases where a feeding correction is not possible, the effective lifetimes serve as upper limits for the "real" lifetime of the excited state.

2.2.2 Bateman equations
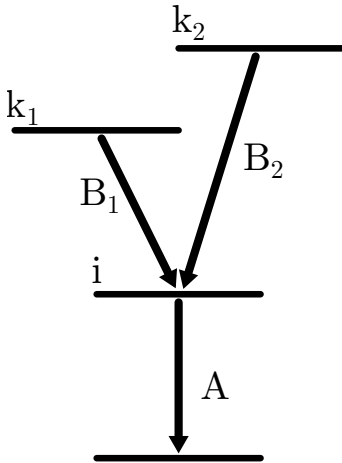
Figure 2.3: Exemplary level scheme with a level of interest i and feeding levels k_1, k_2.

The common starting point for all methods that determine lifetime values from RDDS experiments are the Bateman equations [51], describing the time-dependent population n of a level i. The level i has a lifetime $\tau_i = 1/\lambda_i$ and is fed in general from several levels k with lifetimes $\tau_k = 1/\lambda_k$. An exemplary level scheme is depicted in Fig. 2.3. The population of the level i is then described by the differential equation

$$\dot{n}_i(t) = -\lambda_i n(t) + \sum_k \lambda_k b_{ki} n_k(t). \tag{2.9}$$

To solve the differential equation for the level i, similar equations have to be solved for all feeding levels and a system of coupled differential equations results. The solution of this system of coupled differential equations depends on the lifetimes τ_k, the branching ratios b_{ki} and initial populations $n_k(t = 0)$ of all feeding levels and the lifetime of the level of interest τ_i. Stop component I^{st} and flight component I^{fl} of a γ-ray transition depopulating the level of interest i observed in the RDDS measurement can then be calculated by integrating the time-dependent

population $n_i(t)$ of the level of interest i. Therefore, for transition A from Fig. 2.3

$$A^{fl}(t_0) = \int_0^{t_0} \lambda_i n_i(t)dt,$$
$$A^{st}(t_0) = \int_{t_0}^{\infty} \lambda_i n_i(t)dt,$$

(2.10)

where t_0 is the flight time of the nucleus of interest. To extract the lifetime of a state of interest i, the branching ratios, lifetimes and initial populations of all feeding levels have to be known or assumed. Additionally, the information of the absolute flight times is needed. Absolute flight times can be calculated from absolute target-to-stopper distances determined with the capacitance method (compare Sec. 2.1.1) and the recoil velocity which is determined measuring the Doppler-shift of γ rays. Then with Eqs. (2.9) and (2.10) the calculated decay curves $R(t)$ (Eq. (2.7)) can be compared to the measured data taking into account also the effects of angular distributions and detector efficiencies. Typically only the lifetime of the state of interest is a free parameter in the fit procedures.

2.2.3 Differential Decay Curve Method

A second method to extract lifetime information from RDDS data is the Differential Decay Curve Method (DDCM) [41, 52]. The DDCM can be derived again from the Bateman equations and uses implicit properties of the decay curve $R(t)$ to determine the lifetime that is given as

$$\tau_i = \frac{-A^{st}(t_0) + \sum_k b_{ki} B_k^{st}(t_0)}{\frac{d}{dt} A^{st}(t_0)},$$

(2.11)

using again the exemplary level scheme of Fig. 2.3.

The DDCM has several advantages over an analysis using directly the Bateman equations. Lifetimes extracted with the DDCM do not depend on absolute flight times, but only on relative flight times, that in experiments are more precisely known than absolute flight times (compare Sec. 2.1.1). The quantities needed for a determination of the lifetime in the DDCM are also all experimental observables, which is not the case for an analysis using directly Bateman equations.

2.2.4 Differential Decay Curve Method with γ-γ coincidences

The use of γ-γ coincidences simplifies the DDCM analysis significantly [41]. An energy gate is set on the flight component of a direct feeder of the level of interest i — in the example of Fig. 2.3 for example transition B_1. Then a subtraction of stop components of feeders becomes obsolete and Eq. (2.11) simplifies to

$$\tau_i = \frac{\{B_1^{fl}, A^{st}\}(t_0)}{\frac{d}{dt}\{B_1^{fl}, A^{fl}\}(t_0)}.$$

(2.12)

Here, $\{B, A\}$ denotes the coincident intensity of the transitions A and B, where B is a transition directly feeding the level of interest i and A is a transition depopulating i. The use of γ-γ coincidences additionally avoids problems arising from unobserved side feeding.

2.2.5 Summing of different distances

A special case is a lifetime analysis, where the spectra from different distances are summed. This method is only applied if the statistics of the transition of interest is not sufficient in the spectra of single distances. It has been developed by *J. Litzinger* [53]. The observable from Eq. 2.7 then becomes

$$R_{sum} = \frac{I_{sum}^{st}}{I_{sum}^{st} + I_{sum}^{fl}},$$

(2.13)

where the index *sum* indicates, that the spectrum used to determine these intensities is the sum of all spectra of the single distances. For each distance i the values R_i can also be calculated using the Bateman equations and assuming a feeding pattern and a lifetime of the state of interest. Then, the observable R_{sum} can also be calculated via

$$R_{sum} = \sum_i w_i R_i,$$

(2.14)

where w_i are weights that take into account the different measuring times and reaction rates of the single-distance measurements. The calculated value can then be fitted to the observed value using the lifetime of the state of interest as a free parameter. This way, a lifetime value for the state of interest is determined. An uncertainty of the lifetime value is obtained using Monte-Carlo methods. Note that in this approach there is no decay curve of the state of interest that could give information on possible long feeding contributions. If no information on the feeding is known, only an effective lifetime can be determined.

2.3 Angular correlations of γ-γ cascades

One way to obtain information on spins of excited states is the measurement of angular distributions of γ rays depopulating or populating these excited states. The emission of γ rays from a nucleus is in general not isotropic and is governed by the multipolarity of the emitted γ ray that is restricted by the spin of final and initial state. A measurement of the angular distributions of γ rays allows thus to obtain information on the multipolarity of γ
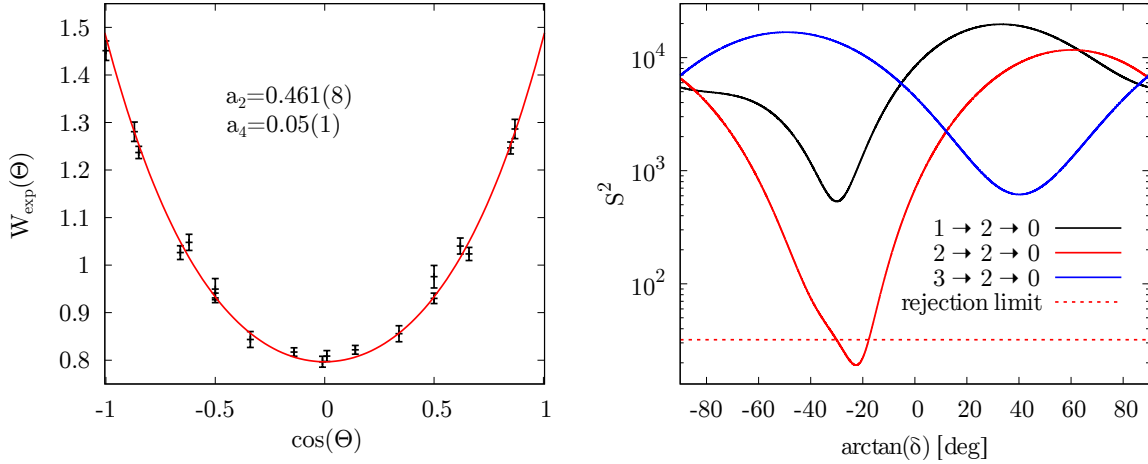
Figure 2.4: *Left:* Angular correlation of the $2_3^+ \to 2_1^+ \to 0_1^+$ (934-609 keV) cascade in ^{214}Po. The intensity of the cascade W_{exp} is plotted against the angle Θ of the angular group. The data were taken from a ^{226}Ra calibration source measurement in the CATHEDRAL spectrometer [54]. The resulting fit parameters are $a_2 = 0.461(8), a_4 = 0.05(1)$.
Right: Comparison of the experimental a_2, a_4 parameters to different spin hypotheses. Shown is the dependence of the loss function S^2 on the mixing ratio δ for three different spin hypotheses. Only a $2 \to 2 \to 0$ cascade with a mixing parameter of $\delta = -0.42(6)$ is not rejected. This slightly improves the value given in Ref. [55] of $|\delta| = 0.37(24)$.

rays, the multipole mixing ratios of the transition and spin and parity of initial and final state. However, if the orientation of the nuclei is not known or isotropically distributed, this information is lost. For isotropically distributed nuclei, it is possible to extract similar information from the measurement of γ-γ cascades (compare e.g. [56]). The detection of the first γ ray fixes a quantization axis and the probability distribution of the angle of emission of the second γ ray $w(\theta)$ can be described with the help of the Legendre polynomials P_k [57]:

$$w(\theta) = \sum_k a_k P_k(\cos\theta). \tag{2.15}$$

The parameters a_k are determined by the multipolarities and multipole mixing ratios of the involved γ rays and the spins of initial, intermediate, and final state. Exact ways to calculate the parameters a_k are given for example in Ref. [58].

An exemplary angular correlation of a γ-γ cascade observed in ^{214}Po is shown on the left hand side of Fig. 2.4. This cascade was measured using a ^{226}Ra source and the CATHEDRAL spectrometer [54] that will be introduced in the next chapter (see Sec. 3.1). The used γ-ray detectors have finite opening angles, leading to an attenuation of the measured distribution [57]. Equation (2.15) is then rewritten as
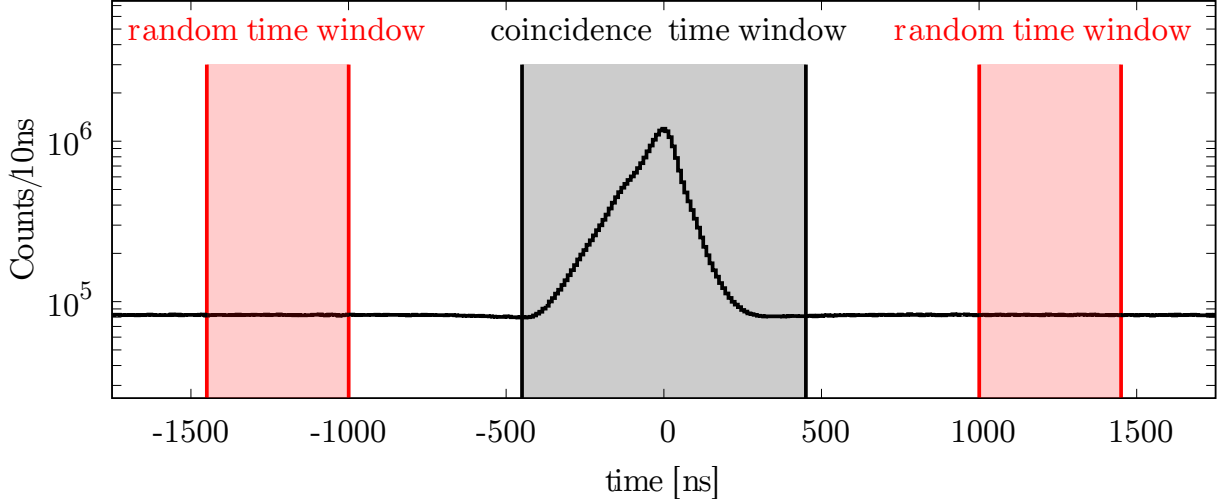
Figure 2.5: Time difference spectrum of two HPGe detectors in the β decay experiment on ^{116}Te. Coincidence spectra are build from events that lie in the coincidence time window. Events in the random time window are used to correct the coincidence events for random coincidences and to correct the angular correlation data of the different angular groups for the different detector efficiencies and number of detector pairs.

$$W_{exp}(\theta) = \sum_k q_k a_k P_k(\cos\theta), \qquad (2.16)$$

where $W_{exp}(\theta)$ is the measured angular correlation and q_k are attenuation coefficients that depend on the geometry of the experimental setup. These can be calculated from geometrical considerations or experimentally determined using known angular correlations. The experimental angular correlation is then used to fit experimental parameters a_k (compare Fig. 2.4). The measured parameters a_k are compared to calculated parameters using different spin hypotheses and multipole mixing ratios using a combined probability distribution S^2 [59]. Such an S^2 minimization is shown on the right hand side on Fig. 2.4. If the minimum S^2 value lies below a rejection limit, the spin hypothesis is not rejected. Ideally, only one hypothesis of spin and multipole mixing values reproduces the experimental parameters a_k with sufficient precision allowing an unambiguous determination of the involved spins and multipole mixing ratios.

2.3.1 Event mixing approach

In experiments measuring angular correlations, usually detectors are not moved around to obtain data for different angles θ. Instead, data are taken with spectrometers with multiple γ-ray detectors. For a measurement where the nuclei of interest are not oriented, relevant data can only be obtained from γ-γ coincidence data involving (at least) two detectors. The number of detector pairs is then given by $N(N-1)/2$ for a setup with N detectors.

The different angles of these detector pairs provide the necessary data points for an angular correlation measurement. In this case of an experiment without a defined orientation axis, detector pairs with the same angle between the two detectors are grouped into so-called angular groups. The measured intensity of the cascade of interest has to be corrected then for the number of detector pairs of the angular group and for the energy-dependent efficiency of the detectors. The efficiencies can in principle be determined before or after the experiment with an efficiency calibration using a known source. If efficiencies are determined in this way, possible errors can arise from time-dependencies of the efficiency (e.g. the efficiency might depend on the count rate of a detector).

The event-mixing approach [60] is an elegant method to extract efficiency data directly from the data of the experiment itself avoiding the problems described earlier in many cases. Coincidence spectra are usually built by selecting only data where two or more events were detected within the same time window ("at the same time"). The length of the time window is usually given by the time resolution of the detectors. Often, these data are then corrected for random time events that are obtained from a time window in a safe distance from the coincidence time window. A time difference spectrum with a coincidence time window and a random time window is shown in Fig. 2.5. The random time events will be isotropically distributed assuming that the nuclei themselves are indeed isotropically distributed. Intensities in random time events of a certain angular group will therefore only depend on the efficiencies of the involved detectors and the number of detector pairs in the angular group and contain thus exactly the information needed for an efficiency correction. From a macroscopic perspective, the random time window and the coincidence window are also still close together and time-dependent changes of detector efficiencies will have the same effect on random time events as on coincident events. Spectra from random time events can thus be used to correct data of different angular groups for the different detector efficiencies. The event-mixing approach has been successfully used for the analysis of angular correlations in ^{116}Te described in Sec. 4.1.

Chapter 3

Experimental setups and equipment

In this chapter, the experimental equipment used in this work is presented. All experiments were conducted at the 10 MV FN Tandem accelerator at the Institut für Kernphysik (IKP) in Cologne, utilizing ion beams from the accelerator as well as the setups and equipment available on-site.

3.1 Gamma-ray spectrometers
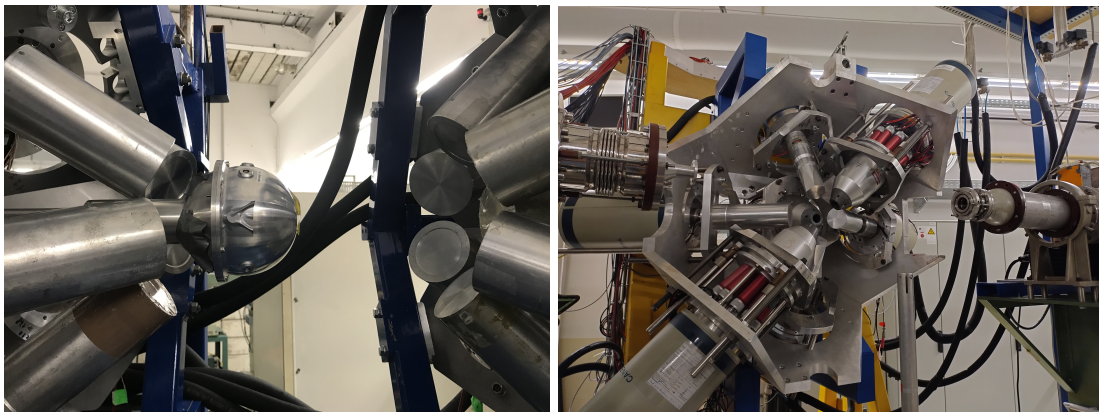
Figure 3.1: *Left*: The Plunger spectrometer with the Cologne coincidence Plunger device mounted inside. The downstream hemisphere (on the right) is slightly opened.
Right: One hemisphere of the opened HORUS spectrometer (in-beam direction left) equipped with seven HPGe detectors. Two of the detectors in this photo are additionally surrounded by Bismuth Germanate (BGO) shields.

Nowadays, γ-ray spectroscopy is a powerful technique that is widely used to study the properties of a nucleus. In this study, three different γ-ray spectrometers at the IKP Cologne were used. In the following section, a short description of these spectrometers and the design idea behind each one of them is presented.

- The Plunger spectrometer
  Until recently, RDDS experiments in Cologne were conducted using the Plunger spectrometer specifically designed for this purpose. For RDDS experiments, high γ-energy resolutions are required to distinguish between shifted and unshifted components of γ-ray transitions. Since the Doppler shift is often only in the range of a few
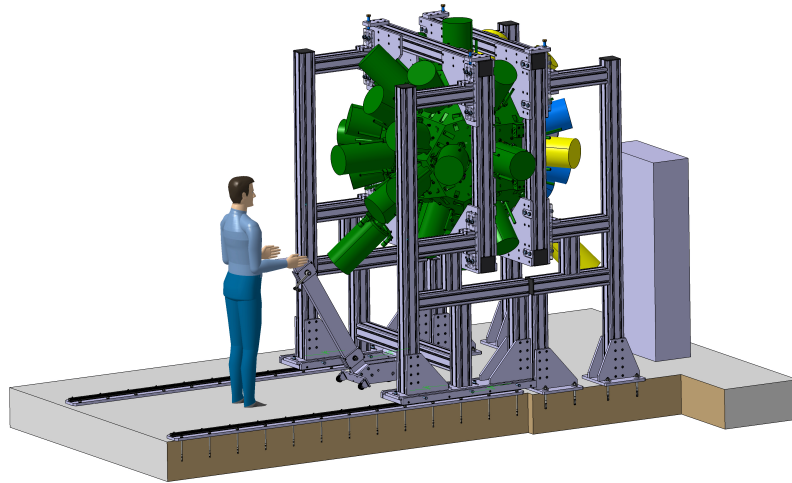
Figure 3.2: Schematic drawing of the Cologne CATHEDRAL spectrometer.

keV, germanium detectors are very well suited for such measurements. Furthermore, the Doppler shift is determined by the angle between the emitted γ-ray and the momentum of the nucleus of interest (compare Eq. (2.6)) which is in general in beam direction. It is therefore necessary that the γ-ray detectors are placed at angles far away from 90°. Further, having multiple detectors at the same angle Θ with respect to the beam axis is of advantage, so that the statistics of single detectors can be summed. Multiple detectors placed at the same angle Θ are commonly called a ring. The Plunger spectrometer was therefore equipped with eleven High-Purity Germanium (HPGe) detectors that were arranged in two rings under 142° and 45° with respect to the beam axis. A picture of the Plunger spectrometer is shown in Fig. 3.1 where the Cologne coincidence plunger device is mounted in the Plunger spectrometer. A list of the detector positions and of the common ring denominations is given in Appendix A.

- The HORUS spectrometer
  The High-Efficiency Observatory for γ-Ray Unique Spectroscopy (HORUS spectrometer) is a γ-ray spectrometer equipped with 14 γ-ray detectors arranged in a cube geometry, positioned along the eight edges and six faces of a cube. This configuration is well-suited for performing angular correlation measurements, as pairs of detectors are organized into angular groups with angles of 55°, 70°, 90°, 110°, 125°, and 180°, covering the full range from 0° to 180°. For details see Refs. [61, 62]. An overview of the detector positions and angular groups in the HORUS spectrometer is also given in Appendix A.

- The Cologne CATHEDRAL spectrometer
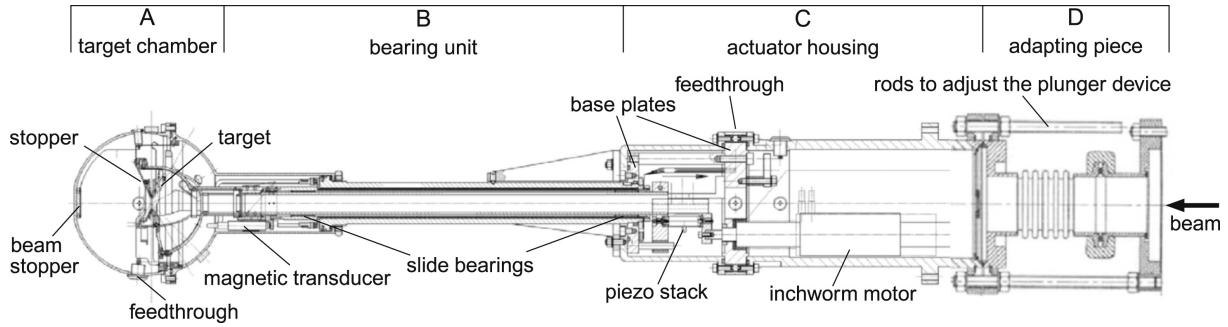
Figure 3.3: Schematic drawing of the Cologne Coincidence plunger device. The figure is taken from Ref. [41]. Note that in the present version of the Cologne coincidence plunger device, the inchworm motor is replaced by a linear actuator fulfilling the same role.

The Cologne CATHEDRAL (Coincidence Array at the Tandem accelerator for High-Efficiency Doppler Recoil And Labr fast-timing measurements) spectrometer is the successor to the Plunger spectrometer. It is designed to measure lifetimes with the RDDS method and the fast-timing method using cerium-doped Lanthanum-Bromide (LaBr$_3$(Ce), for the sake of simplicity often shortened to LaBr) detectors simultaneously. A total amount of 24 HPGe detectors can be mounted in four rings at angles Θ of 30°, 55°, 125° and 150° where each ring consists of six detectors. The γ-ray efficiency using HPGe detectors is thus significantly increased with respect to the γ-ray efficiency of the Plunger spectrometer. Data from these rings will be sensitive for RDDS measurements. Additionally, eight LaBr-detectors can be mounted in a ring at 90° to obtain data for fast-timing analyses. The regular and symmetrical arrangement of the HPGe detectors in the CATHEDRAL spectrometer also allows for the evaluation of data from angular correlation measurements using angular groups, which are specified along with the detector positions in Appendix A. This spectrometer has been introduced in 2023 and a commissioning run was performed. A publication on the commissioning run and on technical details is in preparation [54].

3.2 The Cologne coincidence plunger device

For all RDDS measurements during this work, the Cologne coincidence plunger device was used. A schematic drawing of the Cologne coincidence plunger is shown in Fig. 3.3. A detailed description of the Cologne coincidence plunger device is given in Ref. [41]. As mentioned in Sec. 2.1, plunger devices are designed to regulate the target-to-stopper distances in RDDS experiments. In the Cologne coincidence plunger device, target and stopper foil are stretched on cones and mounted inside the target chamber. The holding structure of the target cone can be adjusted to align target and stopper foil in a parallel orientation. The target foil can be moved with a linear actuator to change the target-to-stopper distance while the position of the stopper foil is fixed. The relative movement of
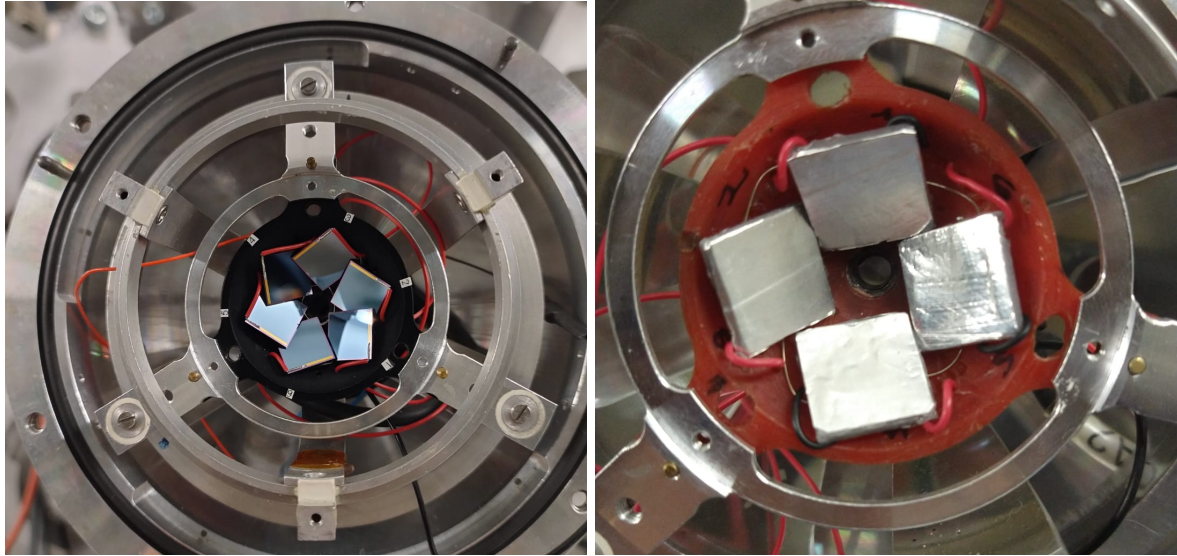
Figure 3.4: Pictures of two different solar cell arrays mounted inside the Cologne coincidence plunger device. On the left-hand side a configuration of the solar-cell array with six solar cells is shown, on the right-hand side a solar-cell array with four aluminum-covered solar cells is shown. The insulation preventing the aluminum to touch the solar cells takes away some space, leading to a configuration with four solar cells. The target cone (not shown) is mounted downstream of the solar cell array (i.e. between the camera and the solar-cell array).

the target foil is measured with two independent devices: with an optical sensor inside the linear actuator itself and with an inductive transducer. Absolute foil separations are extrapolated with the capacitance method [41, 42]. The linear actuator is situated outside the target chamber to minimize the amount of material inside the target chamber that screens γ rays and thus effectively reduces the γ-ray efficiency.

3.3 Solar-cell array

The Cologne coincidence plunger device can additionally be equipped with a solar-cell array, that is mounted directly upstream of the target. The solar cells cover angles between approximately 120° and 160° with respect to the beam axis and can detect charged particles stemming from reactions of the beam with the target foil. In the usual configuration, six solar cells are placed in the solar-cell array (see Fig. 3.4). Each solar cell has an active area of $9\,\text{mm} \times 10\,\text{mm}$ and a thickness of about $0.5\,\text{mm}$. The energy resolution typically lies in the order of some $100\,\text{keV}$ and can sometimes be slightly improved by applying a small voltage (approx. up to $25\,\text{V}$). The sensitivity and energy resolution of the solar cells will dramatically worsen over time if the solar cells are exposed to heavier charged particles.

It is possible to mount a screening aluminum foil on the solar cells that prevents higher-Z particles from entering into the solar cells. The thickness of the aluminum foil can be
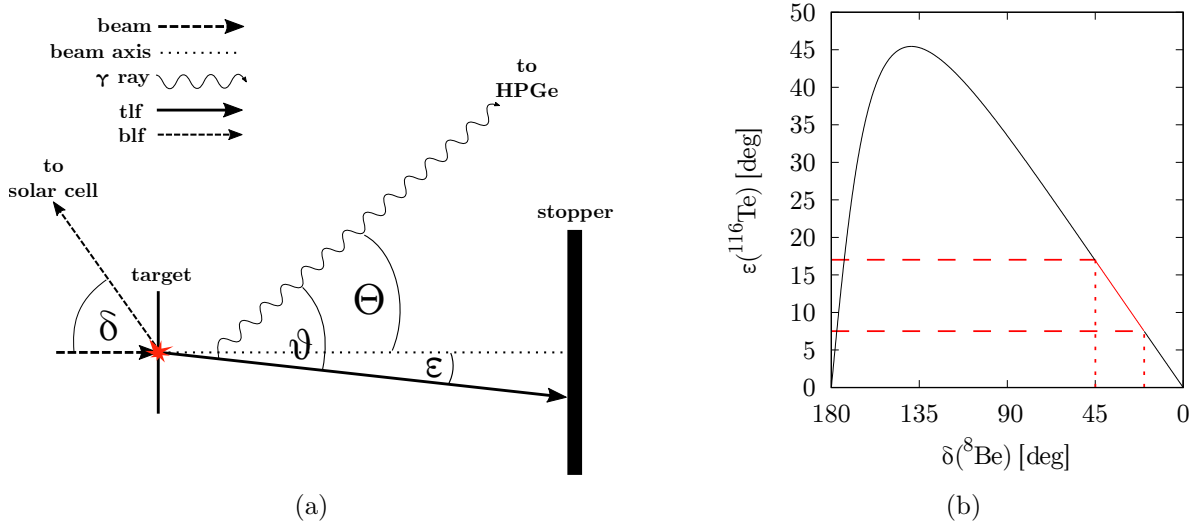
Figure 3.5: (a) Schematic depiction of an RDDS experiment that uses a transfer reaction and subsequent detection of beam-like fragments (blf) in solar cells. In this case, the angle of the HPGe detector to the beam axis Θ is not the same as the angle between the momentum of the target-like fragment (tlf) and a detected photon in said detector θ. (b) Exemplary dependency of the angle ϵ, representing the deviation of the tlf from the beam axis, on the angle of the blf for the α-transfer reaction $^{112}Sn(^{12}C,^{8}Be)^{116}Te$ @ 44 MeV. The opening angle of the solar cells is marked in red.

chosen to be suitable for the experiment. This will clean the solar-cell spectra from signals stemming from heavier charged particles and will also significantly improve the durability of the solar cells since exposure to heavier charged particles is mainly responsible for the degradation of the solar cells. Since the solar cells need to be insulated from the aluminum foil, some space is lost to an insulating frame separating the solar cells from the aluminum foil and only four solar cells can be mounted inside the solar-cell array in this case (see Fig. 3.4).

3.3.1 Application of the solar-cell array for RDDS experiments using transfer reactions

In a transfer reaction, the incident beam particles react with the target nuclei transferring a small number of nucleons from a beam particle to a target nucleus. Additionally, some momentum is transferred depending on the scattering angles. Such transfer reactions — typically two-neutron-transfer and α-transfer reactions — have been used in recent years for RDDS measurements in Cologne [63–70]. For several reasons, it is useful to detect the beam-like fragment (blf): a detection of the blf under a known angle fixes the kinematics of the reaction - namely the recoil velocity and the scattering angle of the target-like fragment (tlf). The nucleus of interest is typically a tlf and the flight time of the nucleus of interest to the stopper foil depends thus on its recoil velocity and scattering angle. Additionally, a

gate on the particle detectors cleans γ-ray spectra from possible contaminations stemming from other reactions like fusion-evaporation reactions, that can have much higher cross sections than the transfer reaction. A placement of the particle detectors under backwards angles is favorable, since a scattering of the blf in backwards angles leads to higher recoil velocities and smaller deviations of the tlf from the beam axis (see Fig. 3.5). The energy of the blfs that is detected in the particle detectors depends on the number and type of transferred nucleons and can thus in theory provide information on the exact type of the observed transfer reaction. However, the energy signal detected by the particle detectors depends additionally on the scattering angle and on the energy loss in the target foil. RDDS experiments require target and stopper foil to have a certain thickness, which will lead to different energy losses of the blfs in the target foil depending on the exact point of interaction of the individual transfer reaction. Furthermore, the opening angles of the used solar cells are rather large. On top of that, blfs stemming from scattering processes in the stopper foil lead to additional signals in the particle spectrum. These effects make a differentiation in the particle spectra between blfs stemming from different direct reactions difficult. As a result, solar-cell-gated γ-ray spectra often show transitions stemming from multiple different reactions leading to possible contaminations of transitions of interest. To still obtain clean γ-ray spectra, different approaches can be tried:

- Events stemming from direct reactions of the beam in the stopper foil can be suppressed by choosing a stopper material that is lighter than the target material. This approach was used in Refs. [66, 69]. At higher energies, the solar cells placed at backward angles will detect only blfs stemming from scattering processes in the heavier target foil . At lower energies, BLFs from scattering processes in the lighter stopper foil will also be detected. An energy gate on higher energies in the particle spectrum will thus select only events stemming from scattering processes in the target foil. In this approach a differentiation between different direct reactions of the beam with the target material is usually not possible. Additionally, the light stopper material typically leads to high reaction rates of fusion-evaporation reactions of the beam with the stopper material.

- Particle-γ-γ coincidences are probably the most powerful approach to obtain clean spectra. However, given the smaller cross sections and γ multiplicities of transfer reactions, the achieved level of statistics is often not sufficient for a successful application of particle-γ-γ coincidences.One of the primary objectives in designing the CATHEDRAL spectrometer was to achieve higher γ-ray efficiency. This increased efficiency is essential for enabling the analysis of transfer reactions using particle-γ-γ matrices in typical experiments conducted in Cologne.

- In the special case of a (^{12}C,^{8}Be) α-transfer reaction, the ^{8}Be BLF will decay immediately into two α particles. The charge difference between the α particles and other

BLFs (e.g. ^{12}C,^{10}Be) is sufficiently large that a screening foil in front of the particle detectors with the right thickness will stop all heavier BLFs (e.g. ^{12}C,^{10}Be) and only let through the α particles leading to very clean γ-ray spectra. For this approach the signals of the particle detectors need to be relatively low-noise, since the deposited energy of the α particles is relatively small. This approach is used in this work.

3.3.2 Doppler correction
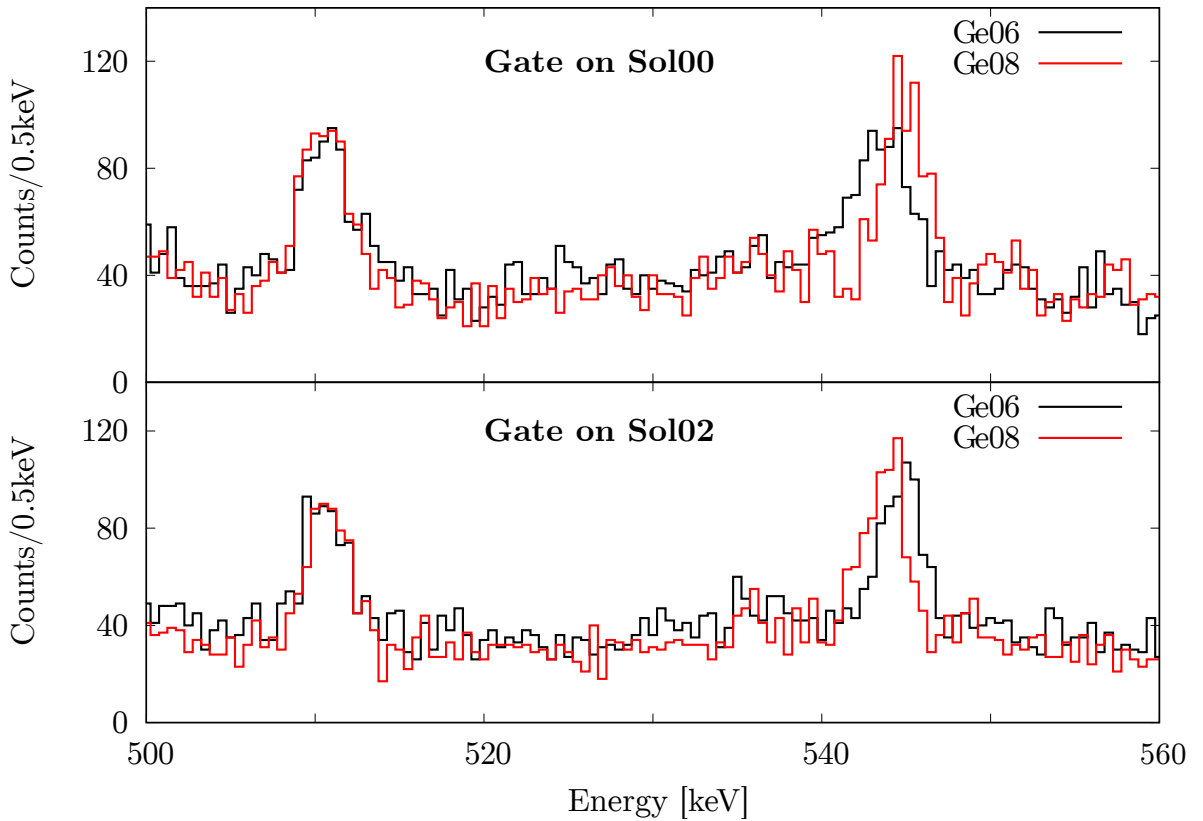
Figure 3.6: Coincidence spectrum comparing the spectra of two Germanium detectors — Ge06 and Ge08 — in the transfer experiment in ^{116}Te. Both Germanium detectors are placed at a zenith angle $\Theta = 45°$ with respect to the beam axis but at different azimuth angles Φ. In the upper (lower) panel, a gate condition is set on the solar cell Sol00 (Sol02). The statistics of all target-to-stopper distances larger than 100 µm were summed. See text for details.

For RDDS measurements, the knowledge of the recoil velocity v and the angle θ between the momentum of the recoiling nucleus and the momentum of the emitted photon is of great importance to determine precise lifetime values. Usually, spectrometers are constructed in a way so that detectors are placed in rings - i.e. several detectors have the same angle Θ to the beam axis. If the average momentum of the recoiling nuclei of interest coincides with the beam axis in a good approximation, the average angle between the emitted photon

and the momentum of the recoiling nucleus ϑ will be the same as the angle between the detector and the beam axis Θ. In transfer experiments, a particle gate on the signal of a blf selects events, where the momentum of the recoiling nuclei is not parallel to the beam axis since the particle detector cannot be placed on the beam axis (see Fig. 3.5). The angle between the momentum of the emitted photon and the momentum of the recoiling nucleus will in general not coincide with the angle Θ of the detector array and will be different depending on the exact zenith angle Θ and azimuth angle Φ of both the particle detector and the γ-ray detector with respect to the beam axis. This leads to different Doppler shifts for different pairs of particle and γ-ray detectors. This effect is shown in Fig. 3.6, where spectra from two different HPGe detectors are compared for gates on two different solar cells. The HGPe detectors are placed in the same ring, i.e. with the same zenith angle $\Theta = 45°$ with respect to the beam axis, but with different azimuth angles Φ. The spectra show γ rays observed in the α-transfer experiment populating ^{116}Te. While the lines stemming from the electron-positron annihilation at $511\,\text{keV}$ are perfectly aligned, the position of the shifted components of the $2_2^+ \rightarrow 2_1^+$ ($540\,\text{keV}$) transition differ for each solar-cell-HPGe pair. If spectra resulting from different solar-cell-HPGe detector pairs are summed, the widths of flight components are broadened.

In these cases, often Doppler-corrected spectra are presented. The Doppler correction adjusts for the Doppler shift, ensuring that the energies of γ-rays are shown in the inertial frame of the recoiling nucleus in the γ-ray spectrum. Such a Doppler correction was performed for the RDDS experiment on ^{116}Te. Often, the Doppler-correction factors are calculated from the kinematics for the given detector angles. For the solar-cell array mounted inside the Cologne coincidence plunger device, the position of the solar cells is not known with precision, the opening angles of the solar cells are quite large and the effective interaction angle is not known. Therefore, in the case of ^{116}Te, the factors were experimentally determined from spectra similar to the spectra shown in Fig. 3.6. The result of the Doppler correction is shown in Fig. 3.7 where Doppler corrected spectra are compared to non-corrected spectra. The Doppler-corrected spectra show the γ-ray transitions at their nominal positions — i.e. "unshifted" — while the the γ-ray transitions in the non-corrected spectra appear shifted. Additionally, the Doppler correction leads to a narrowing of the flight component of γ-lines: the width of the γ-lines shown in Fig. 3.7 is reduced from $6.3(2)\,\text{keV}$ in the non-corrected spectra to $5.3(2)\,\text{keV}$ in Doppler-corrected spectra. Not shown in Fig. 3.7 are stopped components of γ-lines that will be broadened by a Doppler-correction.

In the analysis of the experiment on ^{116}Te, Doppler-corrected spectra are used to better identify short-lived transitions with transition energies typically around $1\,\text{MeV}$ or higher. Since these transitions decay nearly completely in flight, the enhanced resolution of flight components in Doppler-corrected spectra is a valuable asset for a spectroscopic analysis and enables the identification of several new transitions in ^{116}Te (see Sec. 4.1). Doppler-
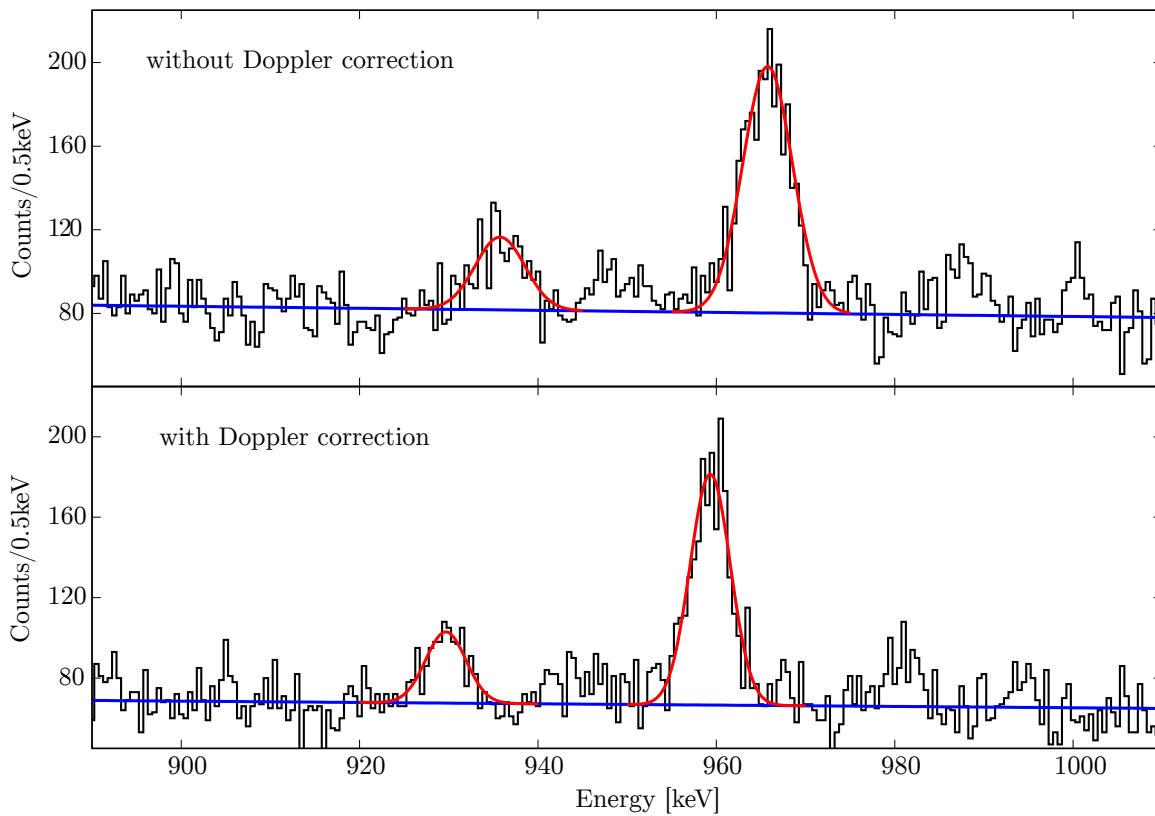
Figure 3.7: Coincidence spectra showing γ-ray transitions in ^{116}Te. A gate condition was set on the solar cells. All target-to-stopper distances are summed up. Two transitions can be seen at 959 keV and 930 keV. The peaks belonging to these two transitions are fitted with a red curve. Since the lifetimes of the observed transitions are relatively small, only the flight component and no stopped component is observed. In the Doppler-corrected spectra, the width is smaller leading to a better visibility of the less intense transition at 930 keV.

corrected spectra are also used for the determination of feeding intensities needed for feeding corrections of the RDDS analysis. The intensities of stopped and flight components required for the RDDS analysis of this experiment are determined using only non-corrected spectra. The same analysis is also possible using Doppler-corrected spectra. In extreme cases, where in non-corrected spectra the flight component is too smeared out for a reliable determination of the intensity, it is possible to determine the intensity of the flight component in Doppler-corrected spectra and the intensity of the stopped component in non-corrected spectra. The latter approach is not used in this work.

Chapter 4

Experimental results

In this chapter, the experimental results from the various performed studies within this work are presented. The chapter is preceded by a chronological overview of the experiments carried out and of their main results:

RDDS measurement on ^{118}Te using a fusion-evaporation reaction

The goal of the first performed experiment was the measurement of the $B(E2; 2_1^+ \rightarrow 0_1^+)$ and $B(E2; 4_1^+ \rightarrow 2_1^+)$ value in ^{118}Te to improve their experimental uncertainty. The employed reaction mechanism is well understood and the experiment was successfully conducted. The results of this experiment can be found in Sec. 4.2.

First RDDS measurement on ^{118}Te using an α-transfer reaction

After some preparatory test experiments with transfer reactions, another RDDS experiment on ^{118}Te was performed, this time using a (^{12}C,^{8}Be) α-transfer reaction. The main goal of the experiment was the lifetime measurement of the 0_2^+ state. Even though it was shown, that the 0_2^+ was populated in the reaction, a determination of a lifetime of the 0_2^+ state was not possible, because of the target issues described in Sec. 2.1.3. The results from this experiment are not included in this work because the repetition of this experiment produced better results in all respects.

RDDS measurement on ^{120}Te using an α-transfer reaction

A second RDDS experiment employing an α-transfer reaction was performed to measure the lifetime of the 0_2^+ state in ^{120}Te. Unfortunately, also this time target issues were present and only limited information on the lifetime of the 0_2^+ state was extracted. The nature of the target issue was finally understood. The results from this experiment can be found in Sec. 4.3.

RDDS measurement on ^{116}Te using an α-transfer reaction

After the target issues had finally been understood, a third RDDS experiment employing an α-transfer reaction was performed — this time on ^{116}Te. In this experiment, the lifetimes of the 0_2^+ state, 2_1^+ state and 2_2^+ state were measured. The results of this experiment are presented in Sec. 4.1.

γ-ray spectroscopy of ^{116}Te following the β decay of ^{116}I

Excited states in ^{116}Te were populated in β decay. The angular correlation analysis of the obtained data allowed the first unique identification of the 0_2^+ state and the first determination of mixing ratios needed for the calculation of absolute transition strengths.

The results of this experiment are presented in Sec. 4.1.

Second RDDS measurement on ^{118}*Te using an α-transfer reaction*

With a new target, a last RDDS measurement on ^{118}Te was performed. The lifetime of the 0_2^+ state was successfully measured. The results of this measurement are included in Sec. 4.2.

4.1 Publication I: Structures of low-lying states in ^{116}Te

Two experiments were performed on properties in ^{116}Te. A lifetime measurement using the RDDS method and a measurement of angular correlations of γ rays following the β decay of ^{116}I. As the results of these measurements have already been published, they will not be described here again. Instead, the relevant publication is directly included. The individual contributions of the different coauthors to the publication are detailed in the following list.

- A. Blazhev prepared the targets for both experiments

- F. von Spee planned, set up and performed the RDDS experiment together with M. Beckers, C. Fransen, C.-D. Lakenbrink, F. Dunkel and A. Esmaylzadeh

- F. von Spee analyzed the RDDS experiment

- F. von Spee planned the β decay experiment

- F. von Spee set up and performed the β decay experiment with the help of M. Weinert, M. Schiffer, G. Hackenberg, L. Knafla and A. Esmaylzadeh

- F. von Spee analyzed the data of the β decay experiment with the help of L. Knafla

- F. von Spee discussed the results with N. Warr, J. Jolie and A. Dewald

- F. von Spee performed the IBM-1 calculations

- F. von Spee wrote the article

Structure of low-lying states in ^{116}Te

F. von Spee [*], M. Beckers, A. Blazhev, A. Dewald, F. Dunkel, A. Esmaylzadeh, C. Fransen, G. Hackenberg, J. Jolie, L. Knafla, C.-D. Lakenbrink, M. Schiffer, N. Warr, and M. Weinert

Institut für Kernphysik, Universität zu Köln, Zülpicher Straße 77, 50937 Köln, Germany

Low-lying excited levels in ^{116}Te were studied by measuring level lifetimes with the recoil-distance Doppler-shift method in the ^{112}Sn(^{12}C, ^{8}Be)^{116}Te α-transfer reaction and angular correlations following the β decay of ^{116}I. Both experiments were performed at the Cologne FN Tandem accelerator. Several new levels were discovered below 3.2 MeV excitation energy, spins and multipole mixing ratios were determined via angular correlations. Lifetimes were measured for the $2_1^+, 0_2^+, 2_2^+$, and 4_1^+ and upper limits for lifetimes were determined for higher lying levels. The experimental findings are compared to calculations in the U(5) limit of the interacting boson model and are also discussed in the framework of shape coexistence which is expected in midshell Te isotopes.

I. INTRODUCTION

The low-lying level structure of midshell Te isotopes resembles that of a vibrational nucleus in a similar fashion to the midshell Cd isotopes, that mirror the Te isotopes with respect to the $Z = 50$ proton shell closure. In the Cd isotopes it is well known that this vibrational picture is not sufficient to describe the low lying structure and that instead many observables indicate that shape coexistence is needed to understand the low-lying structure of midshell Cd isotopes [1]. Additional 0^+ and 2^+ states were found [2] close to the $0_2^+, 2_2^+$, and 4_1^+ states that were presumed to be the two phonon triplet. These states were in some cases strongly populated in the (^{3}He, n) transfer reaction [3]. This can be an indication that these states belong to 2p-4h intruder structures [1]. Band structures were found on top of excited 0^+ states [4], also with the help of $B(E2)$ strengths of the in-band transitions [5]. Experimental signatures of shape coexistence in the Cd isotopes are well summarized for example in Refs. [1,6].

Since the Te isotopes mirror the Cd isotopes with respect to the $Z = 50$ proton shell closure, the discovery of shape coexistence in midshell Cd isotopes has lead to the suspicion that shape coexistence is also present in midshell Te isotopes. Over 30 years ago, Rikovska *et al.* identified intruder states using existing level systematics and relative $B(E2)$ values [7]. As of today, experimental evidence for shape coexistence in Te, however, is still not nearly as clear as it is in the Cd isotopes. The $B(E2, 4_1^+ \rightarrow 2_1^+)/B(E2, 2_1^+ \rightarrow 0_1^+)$ $(B_{4/2})$ ratios are inconsistent along the isotopic chain: in ^{118}Te a $B_{4/2}$ ratio of 2.1(6) was measured by Pasternak *et al.* [8] in agreement with a vibrational picture while Möller *et al.* measured a $B_{4/2}$ ratio of 0.84(14) in ^{114}Te that cannot be explained by any collective model [9]. From a second lifetime measurement in ^{118}Te the absolute transition strength $B(E2, 2_3^+ \rightarrow 0_2^+) = 60^{+30}_{-17}$ W.u. [10] was measured. This

value could indicate that the 2_3^+ state is indeed a first member of an intruder band built on top of the 0_2^+ state. For most other suspected intruding structures in midshell Te, possible in-band transitions have not yet been observed or absolute transition strengths are missing. The status quo of experimental evidence for shape coexistence in Te isotopes—or the absence of such experimental evidence—is well summarized in [1].

For ^{116}Te, experimental data are especially scarce. Here, any data analysis of γ rays is particularly challenging, since the $4_1^+ \rightarrow 2_1^+$ and $2_1^+ \rightarrow 0_1^+$ transitions lie less than 2 keV apart at 680.8 and 678.9 keV [11]. The two more extensive studies focusing on the low-lying structure of ^{116}Te are a decay study performed by Zimmerman [12] and an in-beam experiment using a (^{3}He, $3n$) reaction performed by Lönnroth *et al.* [13]. These studies were able to identify a couple of low-lying off-yrast states, but data seem incomplete and partially contradict each other. Other experiments have been focusing more on high-spin states [14–17] and only provide limited insight into the low-lying level structure. Data on absolute transition strengths have not been published up to now.

It is the aim of this study to investigate the low-lying structure in ^{116}Te and measure lifetimes of low-lying excited states. For this purpose, low-lying states in ^{116}Te were populated in two different experiments using the ^{112}Sn(^{12}C, ^{8}Be)^{116}Te α-transfer reaction and β decay from ^{116}I. From these two data sets, the level scheme was extended and spins and parities were assigned with the help of γ-γ angular correlations. Absolute transition strengths were extracted, using the obtained lifetime values, branching ratios, and multipole mixing ratios. The new experimental data help to improve the understanding of the low-lying level structure.

II. EXPERIMENT

To analyze the low-lying structure in ^{116}Te, two experiments were performed at the FN tandem accelerator

*fspee@ikp.uni-koeln.de

in Cologne. In a first experiment with the recoil-distance Doppler-shift (RDDS) technique, the nucleus was produced in an α-transfer reaction $^{112}\text{Sn}(^{12}\text{C}, ^{8}\text{Be})^{116}\text{Te}$ with a beam energy of 44 MeV. The target foil was 0.3 mg/cm^2 ^{112}Sn on a 1.4 mg/cm^2 Ta fronting. The ^{112}Sn target material was 80% isotopically enriched. The stopper was a 5 mg/cm^2 Ta foil. The foils were mounted inside the Cologne Plunger device [18] and nine different target-to-stopper distances between 9 and 509 μm were measured. The target-to-stopper distance was monitored during the experiment using the capacitance method introduced by Alexander and Bell [19]. Eleven high-purity Germanium (HPGe) detectors were placed at angles of 45° and 142° with respect to the beam axis to observe Doppler-shifted and unshifted γ rays. The relative efficiency of the HPGe detectors varied between 55% and 90%. Four PIN diodes ("solar cells") were mounted at backwards angles between 120° and 160° to detect α particles stemming from the decay of ^{8}Be. The solar cells were covered with a 40 μm aluminum foil to prevent heavier beam-like fragments, e.g., ^{12}C, ^{10}Be, from entering into the solar cells. Data were collected triggerless for about 16 h for each target-to-stopper distance.

In a second experiment, ^{116}Te was populated in the β decay of ^{116}I with a half-life of 2.9 s. The reaction $^{107}\text{Ag}(^{12}\text{C}, 3n)^{116}\text{I}$ with a beam energy of 52 MeV was used to produce ^{116}I. The products of fusion-evaporation reactions were stopped in the 10 mg/cm^2 thick ^{107}Ag target. In this experiment, a pulsed beam was used where the times of beam-on and beam-off were 5 s each. The HORUS spectrometer [20] was used to detect γ rays following the β decay of reaction products. Data were again collected triggerless for about 24 h.

III. ANALYSIS

The data of the α-transfer experiment were sorted into particle-γ and particle-γ-γ matrices. In total, 10^7 particle-γ events were collected. A Doppler correction was performed using the average recoil velocity of the nuclei after leaving the target and differentiating between different solar-cell-Germanium pairs. Doppler-corrected spectra were used to identify shorter lived, weakly populated transitions and measure their intensities. For the RDDS analysis, noncorrected spectra were used. The average ^{116}Te recoil velocity was determined to be 1.1(1) % c. The measured particle spectrum is shown in Fig. 1. Protons from fusion-evaporation reactions can be found below channel 700, α particles can be found throughout the whole spectrum. At around channel 600, a structure can be seen that is introduced by the feedback system of the plunger device. The feedback system is implemented as described in Ref. [18] and uses a pulse signal for the capacitance measurement. The pulse signal of the plunger feedback system couples with the solar cells and introduces a signal, that can be observed in the solar-cell spectra. The pulse signal was chosen in a way, that the signal induced in the solar cells lies outside of the gate region used for the analysis. A gate onto energies above channel 700 allows to select only events stemming from α-transfer reactions. Figure 2 shows the Doppler-corrected coincidence spectrum of the indicated gate, with the statistics of all detectors and target-to-stopper
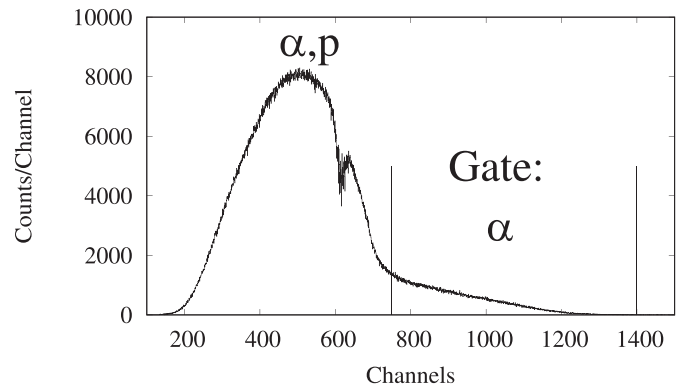

FIG. 1. Particle spectrum observed by the solar cells. Protons from fusion-evaporation reactions like $^{112}\text{Sn}(^{12}\text{C}, np)^{122}\text{Cs}$, $^{112}\text{Sn}(^{12}\text{C}, 2p)^{122}\text{Xe}$ were found at energies below channel 700. The gate was set for higher energies, to select only α particles. The corresponding coincident spectrum in the HPGe detectors is show in Fig. 2. The structure at around channel 600 is introduced by the electronics of the Plunger device.

distances summed. The intensities of lines belonging to transitions in ^{116}Te are shown in Table I.

Data of the β-decay experiment were sorted into γ-γ matrices. In this experiment, 2×10^{10} γ-γ events were recorded. In the $^{107}\text{Ag}(^{12}\text{C}, X)Y$ reaction, many different nuclei between ^{116}I and ^{110}Sb were populated. In the data that were collected off-beam, γ rays from consequent β decays were detected. To clean the data, γ-γ coincidences were used. A spectrum in coincidence with the $2_1^+ \rightarrow 0_1^+$ transition (679 keV) in ^{116}Te can be seen in Fig. 3. The intensities of lines belonging to transitions in ^{116}Te populated in the β decay of ^{116}I are shown in Table II.

A. Angular correlation analysis

The cube geometry of the HORUS spectrometer leads to six different angles between pairs of detectors (angular groups) at 55°, 70°, 90°, 110°, 125°, and 180°.

TABLE I. All observed γ-ray transitions in ^{116}Te from the α-transfer reaction. Intensities are given relative to the 680 keV doublet since it is the most precisely determined intensity. The uncertainties of the intensities of the $4_1^+ \rightarrow 2_1^+$ transition (681 keV) and the $2_1^+ \rightarrow 0_1^+$ transition (679 keV) are correlated. The uncertainties on the measured transition energies are only given for those γ rays that are newly observed and if the transition energy could not be determined through known level energies.

E_γ [keV]	Intensity	E_γ [keV]	Intensity	E_γ [keV]	Intensity
338	0.82(9)	679	68(3)	1133	6.0(2)
381	2.69(13)	681	32(3)	1171(2)	0.63(10)
540	10.9(3)	760	1.4(2)	1198	1.8(2)
453	0.86(12)	930(2)	1.08(10)	1294(2)	1.9(2)
578	0.66(9)	959	3.7(2)	1441	3.0(2)
594	2.7(3)	981	0.68(9)	1588	1.1(2)
643	5.3(3)	1050(2)	0.94(13)	1902	1.6(2)
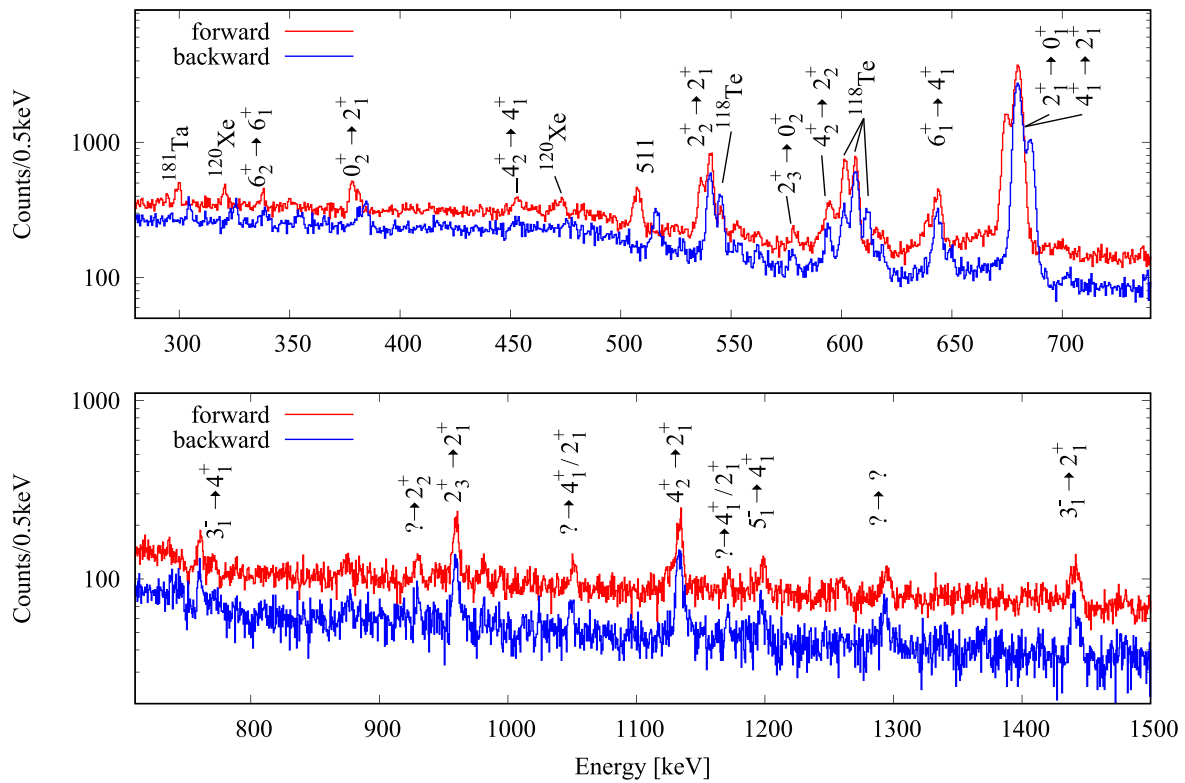
FIG. 2. Doppler-corrected γ-ray spectrum obtained in coincidence with solar cells in the α-transfer experiment. All target-to-stopper distances are summed for the full statistics. An artificial vertical offset of 40 counts has been added to the spectrum of the detectors at forward angle to make the figure more illustrative. Note that the Doppler correction leads to a broadening of the stopped component and a narrowing of the flight component. The flight component is on the nominal energy and the stopped component is shifted. Transitions in ^{116}Te are denoted by spin and parity of the initial and final state, states with unknown spin and parity are denoted with a question mark. Contaminating transitions—stemming from, e.g., target impurities—are denoted by the nucleus in which they take place.

These angular groups were used to perform a γ-γ angular correlation analysis of the data gathered in the β-decay experiment. The angular groups were normalized by the number of detectors and efficiency corrected using the event mixing approach as described in [21,22]. Standard corrections of random coincidences and Compton background were applied. The measured angular dependent intensities were then fitted using the angular correlation probability distribution:

$$W(\theta) = A_0 \left[1 + \sum_{k=2,4} q_k a_k P_k(\cos\theta) \right], \qquad (1)$$

where P_k are Legendre polynomials, a_k are the angular correlation coefficients. A detailed introduction to the theory of angular correlations can be found in Ref. [23]. The
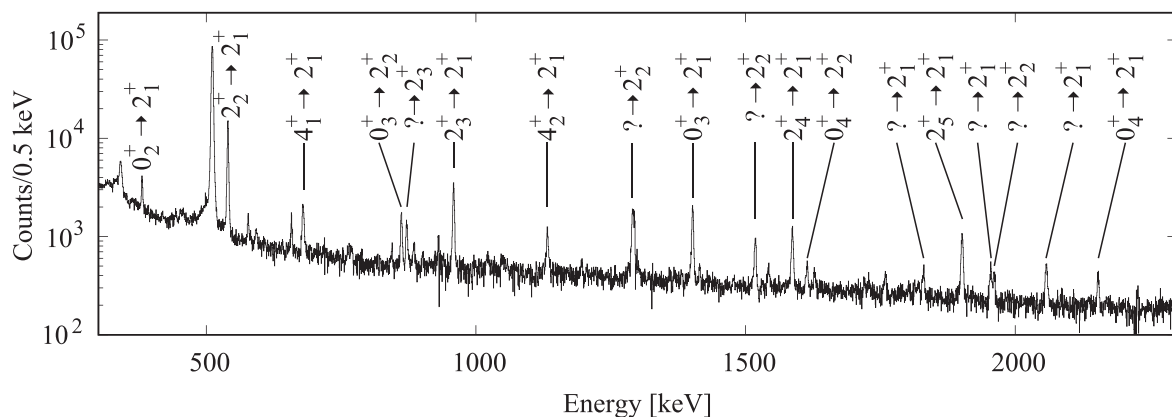
FIG. 3. Spectrum showing γ rays in coincidence with the 679 keV transition in ^{116}Te observed in the β-decay experiment. The statistics of all detectors were summed for this figure. Note that for illustrative purposes not all visible γ rays were marked.

TABLE II. All γ-ray transitions in ^{116}Te observed in the β-decay experiment. Percentage intensities are given relative to the 679 keV transition.

| E_γ [keV]	Intensity	E_γ [keV]	Intensity	E_γ [keV]	Intensity
380.9(1)	1.04(10)	871.3(2)	1.06(10)	1628.0(5)	0.27(3)
419(1)	$\leqslant 0.1$	958.5(2)	3.8(3)	1728.7(6)	0.25(3)
443(1)	$\leqslant 0.2$	1132.4(3)	1.16(10)	1759.4(7)	0.51(6)
452(1)	$\leqslant 0.25$	1195.6(4)	0.25(3)	1829.9(6)	0.49(5)
539.9(1)	9.8(4)	1290.0(5)	2.7(4)	1901.6(4)	1.8(2)
577.6(1)	0.5(1)	1401.7(4)	2.9(2)	1954.7(5)	0.61(6)
592.5(2)	0.26(3)	1414.7(4)	0.26(3)	1961.4(4)	0.63(10)
678.8(1)	100	1517.9(4)	1.40(10)	2057.7(5)	0.92(10)
680.6(3)	0.7(2)	1542.7(5)	0.34(4)	2153.8(6)	0.6(1)
769(1)	0.2(1)	1586.8(5)	1.8(2)	2736(1)	1.0(2)
861.8(1)	1.41(15)	1614.1(5)	0.47(5)		

attenuation coefficients q_k were geometrically determined to be $q_2 = 0.95(1)$ and $q_4 = 0.85(1)$. It turned out that only cascades containing the ground state transition $2^+_1 \to 0^+_1$ (679 keV) had enough statistics to be used in this analysis. At first, a free fit of the parameters a_2 and a_4 was performed (columns 2 and 3 of Table III). Examples of such a fit are shown in Fig. 4 for different cascades. Then, several spin and multipole mixing ratio hypotheses were tested with an S^2 versus $\arctan(\delta)$ minimization procedure, as described in [24]. In Fig. 5 such an S^2 test is shown for the case of the 959-679 keV cascade. The resulting spin hypotheses that were not rejected and the corresponding multipole mixing ratios for each cascade are shown in columns 4 and 5 of Table III.

B. Level scheme and spin assignment

With the new data, the level scheme of ^{116}Te was extended. A level scheme is displayed in Fig. 7 showing only excited states and transitions observed in this study.

TABLE III. Results of the angular correlation analysis of transitions in coincidence with the $2^+_1 \to 0^+_1$ transition (679 keV).

γ [keV]	a_2	a_4	$J_1 \to J_2 \to J_3$	δ
381	0.44(10)	1.02(10)	$0 \to 2 \to 0$	–
540	$-0.13(3)$	0.26(3)	$2 \to 2 \to 0$	$5.0^{+1.0}_{-0.8}$
959	0.51(5)	0.13(6)	$2 \to 2 \to 0$	$-0.7(1)$
1132	0.1(2)	0.0(2)	$(1, 2, 3, 4) \to 2 \to 0$	–
1402	0.38(6)	1.15(6)	$0 \to 2 \to 0$	–
1587	0.35(5)	$-0.03(12)$	$2 \to 2 \to 0$	$-0.15(15)$
1759	0.1(2)	$-0.3(2)$	$(1, 2, 3, 4) \to 2 \to 0$	–
1830	0.5(2)	0.5(2)	$(0, 2) \to 2 \to 0$	–
1902	0.33(8)	$-0.02(10)$	$2 \to 2 \to 0$	$-0.10(15)$
1955	0.1(2)	$-0.4(3)$	$(1, 2, 3, 4) \to 2 \to 0$	–
2058	0.1(1)	0.0(1)	$(1, 2, 3, 4) \to 2 \to 0$	–
2154	0.6(2)	1.2(2)	$0 \to 2 \to 0$	–

1. Levels at 678.9 and 1359.7 keV

The ordering of the two γ rays belonging to the $2^+_1 \to 0^+_1$ and $4^+_1 \to 2^+_1$ transitions is not always consistent in the literature. Most studies [12–15,17] have identified the 679 keV γ ray with the $2^+_1 \to 0^+_1$ transition and the 681 keV γ ray with the $4^+_1 \to 2^+_1$ transition. However, in [16] this ordering is swapped. Both our measurements confirm the majority of measurements that assign the 679 keV line to the $2^+_1 \to 0^+_1$ transition and the 681 keV line to the $4^+_1 \to 2^+_1$ transition.

2. Level at 1060 keV

The decay of this level to the 2^+_1 (381 keV) has been observed by Zimmerman [12] in β decay before. Zimmerman assigns $J^\pi = 0^+$ to this state based on systematics as well as spin and parity analysis and observes a feeding transition (578 keV) from the level at 1637 keV, to which he assigns a 2^+ state. The assignment of 0^+ to the level at 1060 keV remained somewhat disputed, since Lönnroth *et al.* [13] assigned 3^+ to the level at 1637 keV and did not observe a level at 1060 keV. In this study, a level at 1060 keV and feeding from the level at 1637 keV was observed in both reactions. The angular correlations of the 381-679 keV cascade clearly identify this state as an excited 0^+ state (compare Fig. 4).

3. Level at 1219 keV

This level was first identified by Gowdy *et al.* [25] and the assignment of 2^+ to this state is undisputed. The angular correlation measured in this study show that the $2^+_2 \to 2^+_1$ transition (540 keV) is nearly a pure $E2$ transition. A $2^+_2 \to 0^+_1$ transition (1219 keV) has not been observed in any previous experiment and was also not observed in this study. An upper limit of 1% relative to the intensity of the $2^+_2 \to 2^+_1$ transition (540 keV) was established for the branching of the $2^+_2 \to 0^+_1$ transition (1219 keV) based on the observation limit of this experiment.

4. Level at 1637 keV

As mentioned before, the two studies that have observed this level by Zimmerman [12] and Lönnroth *et al.* [13] disagree on the spin assignment. In this study, the two decays of the level at 1637 keV to the 0^+_2 and 2^+_1 states with transition energies of 578 keV and 959 keV were observed in both experiments. The observed branching ratio of 15(3)% to the 0^+_2 state with respect to the transition to the 2^+_1 state is in agreement with the value reported by Zimmerman [12]. Angular correlations of the 959-679 keV cascade show that the level at 1637 keV has spin 2 and that the decay to the 2^+_1 state (959 keV) is a mixed $E2/M1$ transition with a multipole mixing ratio of $\delta = -0.7(1)$ (compare Fig. 4). The S^2 minimization for this cascade is shown in Fig. 5 clearly identifying that this state has spin 2.

5. Levels at 1811 keV and 2340 keV

Before assigning a spin to the level at 1811 keV, it is useful to assign spin and parity to the level at 2340 keV first. In this study, the level at 2340 keV has been observed only in the α-transfer reaction, where the level was only weakly
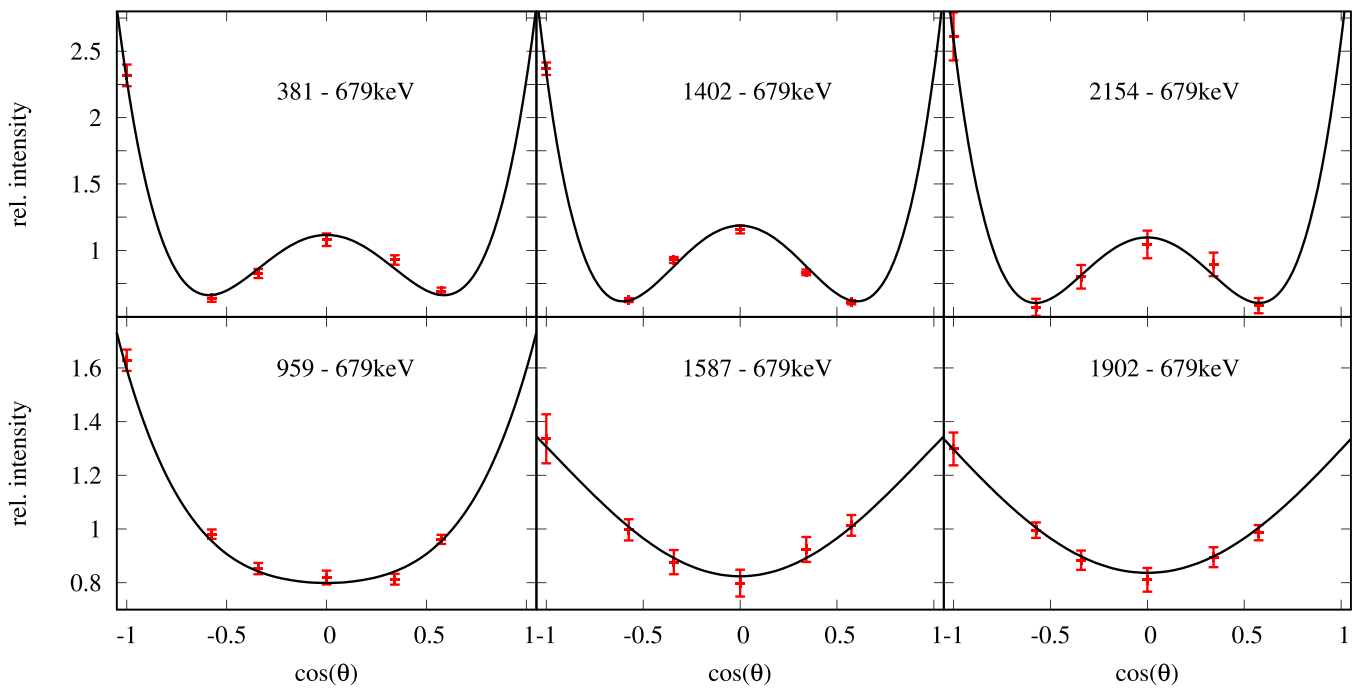
FIG. 4. Angular correlations of γ-γ cascades in ^{116}Te. Experimental intensities are shown in red. The parameters of the best fit, which is shown in black, can be found in Table III.

populated. Decays to the 6_1^+ state and 4_1^+ state were observed. The level was first observed by Lönnroth *et al.* [13] who tentatively assigned spin and parity of 5^+ to the state. More recent studies, however, identify the state at 2340 keV as 6^+ state [15,17] and observe feeding from 8^+ states. Here, this
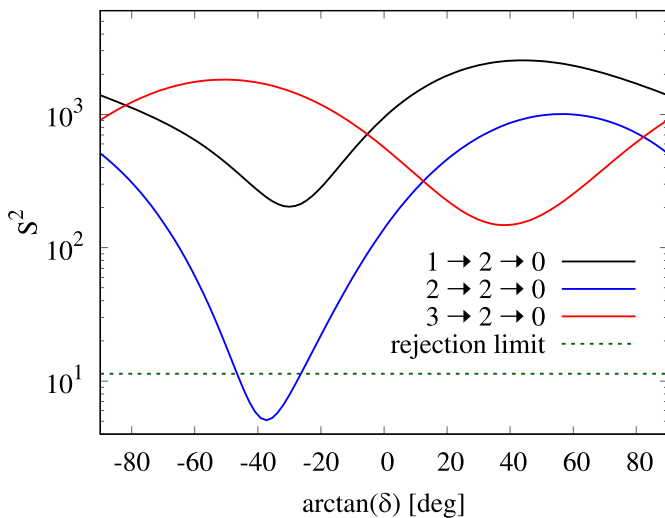

FIG. 5. Spin and multipole mixing ratio determination for the 959-679 keV cascade via angular correlations: For different spin hypotheses of $J_i \rightarrow 2 \rightarrow 0$ cascades, the resulting S^2 minimization is shown depending on the multipole mixing ratio $\delta^2 = \frac{T(L_{\min}+1)}{T(L_{\min})}$. Here, $T(L)$ is the probability to have a transition with angular momentum L. All hypotheses above the 99% confidence limit are rejected and spin 2 is adopted for the 1637 keV state. The multipole mixing ratio is extracted from the minimum S^2 value and the uncertainty is taken at $S_{\min}^2+1$.

latter assignment is adopted. The level at 2340 keV represents thus the 6_2^+ state.

Besides the decays to the 6_1^+ and 4_1^+ state, in two studies [13,15] also a cascade of two transitions with energies of 527 keV and 593 keV was observed connecting the 6_2^+ state at 2340 keV with the 2_2^+ state at 1219 keV. The ordering of these two γ-ray transitions is swapped in the two earlier studies. In [13] the intermediate level is placed at 1811 keV, but in [15] it is placed at 1746 keV. The level at 1811 keV is confirmed by Zimmerman [12] and was also observed in this study in both investigated reactions, but no level at 1746 keV was identified. It is therefore assumed here, that the level at 1746 keV does not exist and that the level at 1811 keV is fed from the level at 2340 keV. This $6_2^+ \rightarrow 4_2^+$ transition was not observed in this study because the statistics were not sufficient. Since the level at 1811 keV has decay branches to the 2_1^+ and 2_2^+ state and is fed from a 6^+ state, here the state is assigned spin and parity of 4^+. In this study, the decays to the 2_2^+ state (1132 keV) and 2_1^+ state (593 keV) were observed in both experiments. The angular correlation of the 1132-679 keV cascade shows no clear anisotropy, but does not contradict a $4 \rightarrow 2 \rightarrow 0$ cascade. It has to be noted though that the branching ratios of the decaying transitions to the 2_1^+ state (1132 keV), 2_2^+ state (593 keV), and 4_1^+ state (452 keV) of this level do not agree for the different reactions (compare Tables I and II). Possible explanations are unobserved contaminations or a level doublet at 1811 keV.

6. Level at 2081 keV

The level has previously been observed by Zimmerman [12] through the decay transitions to the 2_1^+ state (1402 keV) and 2_2^+ state (862 keV) and was assigned spin 1 or 2. But the
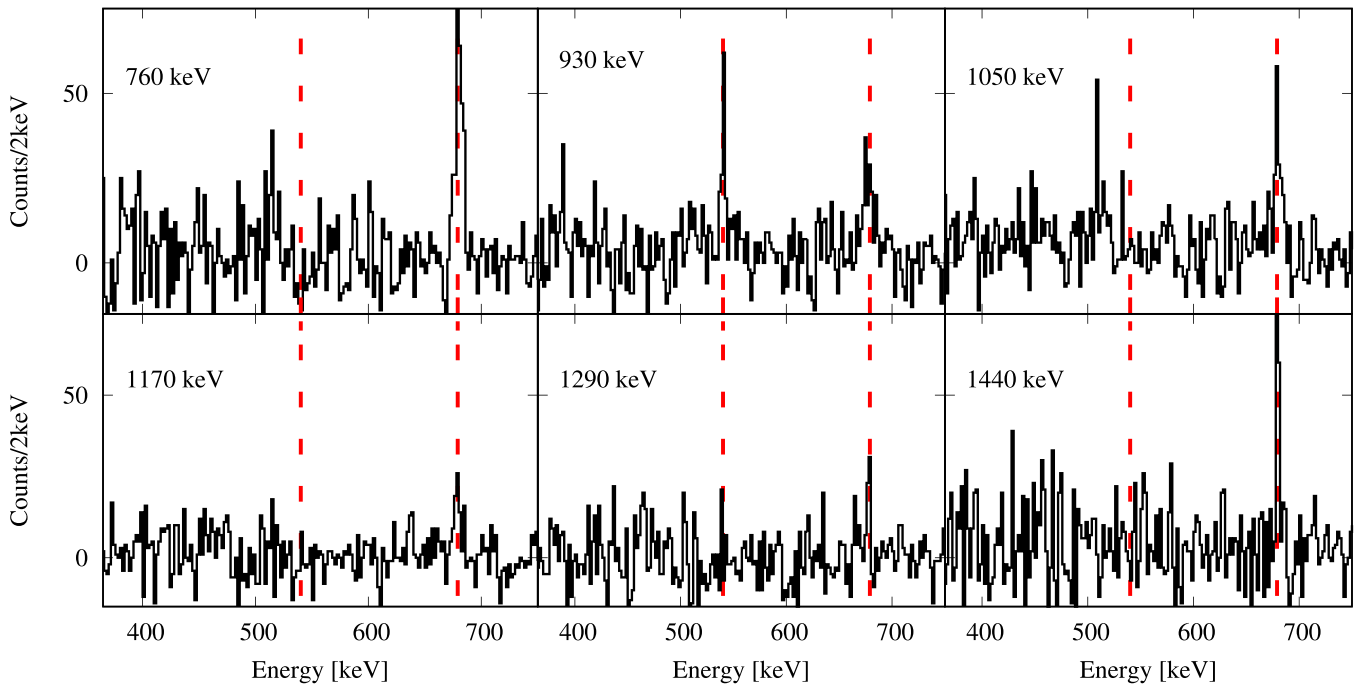
FIG. 6. Doppler corrected spectra obtained from particle-γ-γ coincidences in the α-transfer experiment. The γ gate is set on the transition shown in the upper left corner of each panel, the transition energy is rounded to 10 keV. The particle gate just requires a particle to be detected in the solar cells. The positions of the 680 keV doublet and the $2_2^+ \to 2_1^+$ transition at 540 keV are marked with red dashed lines. The statistics of all HPGe detectors and all target-to-stopper distances are summed.
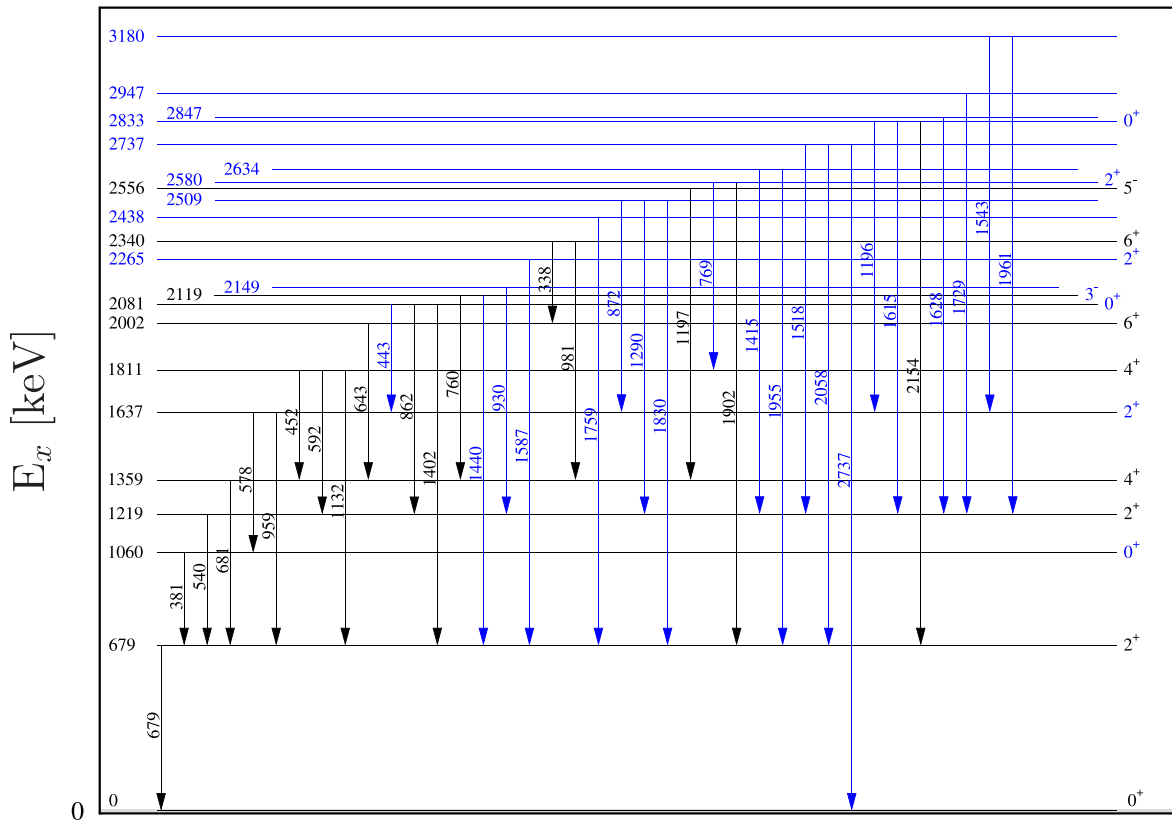
FIG. 7. Level scheme of ^{116}Te observed in the current study. New results are marked with blue color. Blue transitions indicate, that the transition was observed for the first time. Blue level energies and level lines correspond to levels that were placed for the first time. Blue spin and parity imply that the spin and parity were assigned for the first time or clarified. Indentation of lines and numbers is used to improve the readability of the figure.

angular correlation of the 1402-679 keV cascade measured in this study in the β-decay experiment clearly shows that the level at 2081 keV has spin 0 (compare Fig. 4).

7. Level at 2119 keV

This level has been observed by Lönnroth et al. [13] via the 760 keV decay transition to the 4_1^+ state. In the present study, the level was confirmed in the α-transfer experiment. Two decays were observed: the known 760 keV decay to the 4_1^+ state and a previously unknown decay transition (1441 keV) to the 2_1^+ state. The 1441 keV transition matches the energy difference of the level at 2119 keV and the 2_1^+ state and was observed in coincidence with at least one member of the 680 keV doublet in particle-γ-γ coincidences (see Fig. 6). The branching to the 2_1^+ is roughly twice as strong as the previously known decay to the 4_1^+ state. From the spin of the two final states, it is possible to conclude that the level at 2119 keV should have a spin between 2 and 4.

In their study, Lönnroth *et al.* [13] not only measured γ-ray transitions but also conversion electrons and assigned $E1$ to the transition of the level at 2119 keV to the 4_1^+ state (760 keV) with the help of angular distribution coefficients and conversion coefficients. They tentatively assigned 5^- to the state at 2119 keV, but with the present results, a spin of 5 can be excluded and we assign a 3^- to the state.

It is noticeable that the branching ratios of the level at 2119 keV do not resemble branching ratios of the 3_1^- states in neighboring Te isotopes (see [26,27]). To avoid possible assignment errors, further measurements of properties of the state at 2119 keV would be helpful.

8. Level at 2149 keV

In the α-transfer experiment a new transition with an energy of 930 keV was observed. Particle-γ-γ coincidences show coincidences with both 540 keV and 680 keV (compare Fig. 6). A new level is thus placed above the 2_2^+ state at 2149 keV.

9. Level at 2265 keV

This level was observed for the first time in this study. The 1587 keV transition connecting this new state with the 2_1^+ state is observed in both experiments. The angular correlation of the 1587-679 keV cascade suggests that the level has spin 2 and decays with nearly pure $L = 1$ to the 2_1^+ state and was thus assigned a 2^+ (compare Fig. 4).

10. Level at 2509 keV

A level at 2509 keV has not been reported in previous works so far. In this work, three decays to the 2_1^+, 2_2^+, and 2_3^+ with transition energies of 1830 keV, 1290 keV, and 873 keV were identified. The statistics of the angular correlation of the 1830-679 keV cascade are quite poor, but show clear anisotropy. The 1290-540 keV cascade is unfortunately contaminated by random events stemming from the very strong $2_1^+ \rightarrow 0_1^+$ transition in ^{116}Sn and could not therefore be analyzed. The 871-959 keV cascade shows no clear anisotropy.

The anisotropy observed in the 1830-679 keV cascade implies that a spin of 0 and 2 is the most likely.

11. Level at 2580 keV

A transition with an energy of 1902 keV was observed but not placed by Zimmerman [12], since statistics were not sufficient to obtain information from γ-γ coincidences.

In this study, γ-γ coincidences clearly show that the 1902 keV transition is only in coincidence with the 679 keV ground state transition. Angular correlations of the 1902-679 keV cascade are consistent with the level at 2580 keV having spin 2 and the decay to the 2_1^+ state having a nearly pure dipole character (compare Fig. 4). A small branching to the 4^+ state at 1811 keV was identified. The level was also observed in the α-transfer reaction.

12. Level at 2736 keV

This level was observed for the first time in this study in β decay. In γ-γ coincidences, the decays to the 2_1^+ and 2_2^+ state were observed. In the γ-ray singles spectra the decay to the ground state was observed, suggesting that this state has spin 1 or 2.

13. Level at 2832 keV

The 2154 keV transition was observed before by Zimmerman but not placed, because the statistics in γ-γ coincidences was not sufficient. In this study, the 2154 keV transition had observed coincidences with the 679 keV ground state transition only, and a level was thus placed at 2832 keV. The angular correlation shows of the 2154-679 keV cascade measured in this study show, that the level has spin 0 (compare Fig. 4). Additionally, decay branches to the 2_2^+ (1614 keV) and 2_3^+ (1196 keV) states were identified.

14. Levels at 2438 keV, 2634 keV, 2847 keV, 2947 keV, 3180 keV

Levels with these excitation energies were not observed in previous works. The levels were populated only in β decay and were placed with the help of γ-γ coincidences. Angular correlations could not be used to assign a spin to the levels.

15. Transitions with energy 1050 keV, 1171 keV, 1294 keV

These transitions were observed only in the transfer experiment. For all three transitions the Doppler shift corresponded to the kinematics of the ^{112}Sn(^{12}C, ^{8}Be) ^{116}Te α-transfer reaction. Therefore it is very likely that the transitions are indeed transitions in ^{116}Te. In Fig. 6 coincidence spectra are shown. The data suggest that the line at 1050 keV is in coincidence with at least one member of the 680 keV doublet but it was not possible to conclude whether it was in coincidence with just the $2_1^+ \rightarrow 0_1^+$ transition or also the $4_1^+ \rightarrow 2_1^+$ transition. The statistics do not allow to draw a final conclusion on coincident transitions of the 1171 keV and the 1294 keV lines.

C. Lifetime analysis

Lifetimes were measured in the α-transfer experiment using the RDDS method. For a detailed overview of RDDS measurements, the reader is referred to Ref. [18]. In this

experiment, the solar cells registered only protons and α particles stemming from fusion-evaporation reactions as well as α particles stemming from (^{12}C, ^{8}Be) transfer reactions and the subsequent decay of ^{8}Be into two α particles. A gate on higher energies in the solar cells cleared the spectra of fusion evaporation events, as explained at the beginning of Sec. III and only events from the α-transfer reaction remained. Additionally, the energy condition on the solar cells selected events where the target-like nuclei of interest moved with relatively high recoil velocities and more in the beam direction, since the solar cells were mounted at backwards angles.

Data were taken for relative target-to-stopper distances of 1 µm, 8 µm, 18 µm, 30 µm, 70 µm, 120 µm, 200 µm, 300 µm, and 500 µm. The uncertainty of the relative target-to-stopper distances is smaller than 1 µm for small distances and about 1% for distances larger than 100 µm. The absolute distances were determined by extrapolating the dependency of the capacitance on the relative distance. The offset between relative and absolute distances was determined to be 8(5) µm. For details to the capacitance method and the determination of absolute target-to-stopper distances, the reader is referred to Refs. [18,19,28].

The average recoil velocity was determined to be $v/c = 1.1(1)\%$ from the Doppler-shift of transitions populated in the transfer experiment. For the transitions of interest, decay curves $R(x)$ were calculated, where I_s and I_u are the shifted and unshifted components of the transitions of interest, that depend on the distance x:

$$R(x) = \frac{I_u(x)}{I_s(x) + I_u(x)}. \tag{2}$$

Lifetimes τ_i of the level i were analyzed with the differential decay curve method (DDCM) (compare [18]) using the NAPATAU code [29] depending only on precisely known relative target-to-stopper distances and not on the less precisely known absolute distances:

$$\tau_i = \frac{-R_i(x) + \sum_k b_{ki} R_k(x)}{\frac{d}{dx} R_i(x)} \frac{1}{v}. \tag{3}$$

Here, $R_i(x)$ is the decay curve at the distance x for the level i and v is the recoil velocity of the nucleus. The level i is generally fed by several levels k. The factors b_{ki} represent the percentage of the population of the level i that stems from the feeding of the level k. The results of the DDCM analysis were crosschecked with a Monte Carlo approach simulating the Bateman equations as performed in [30]. The Bateman equations,

$$\dot{n}_i(t) = -\lambda_i n_i(t) + \sum_k b_{ki} \lambda_k n_k(t), \tag{4}$$

describe the population $n_i(t)$ of a level i with a lifetime $\tau_i = \frac{1}{\lambda_i}$ with feeding levels k. In the Monte Carlo simulation, the measured lifetimes, initial populations, and intensities of feeding transitions of all feeding levels were varied within the experimental uncertainty in order to simulate the decay curve of the state of interest that then only depends on the lifetime of the state of interest. The results of the simulation can be compared to the experimental data and a best fit for the lifetime can be
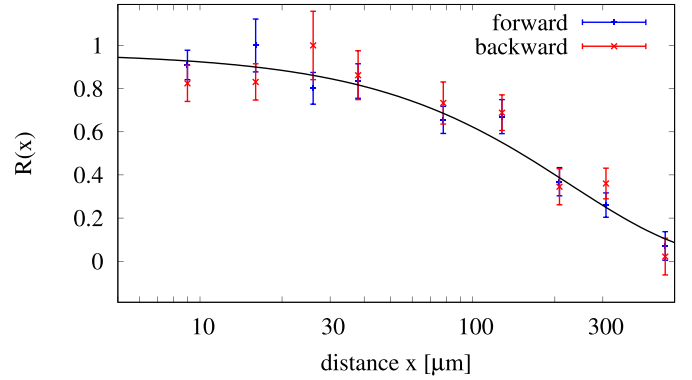

FIG. 8. Decay curve $R(x)$ of the 0_2^+ state for detectors at forward and backward angles depending on absolute distances x. The uncertainty on the absolute distances is not represented in this picture. The uncertainty of the offset is about 5 µm and much larger than the uncertainty of the relative distances which is below 1 µm.

found. In this approach, absolute target-to-stopper distances have to be used.

For the lifetime of the 6_1^+ state, the intensities of the shifted and unshifted components of the $6_1^+ \rightarrow 4_1^+$ transition (643 keV) were determined in particle-gated γ-ray spectra, but uncertainties in the lifetime of the 6_2^+ state, feeding the 6_1^+ state via the observed $6_2^+ \rightarrow 6_1^+$ transition (338 keV) and possible unobserved feeding limited the analysis to give only an upper limit of 8 ps for the lifetime. Also for the 4_2^+ state, only an upper limit of the lifetime could be determined: the discrepancy between the lifetime values obtained using the DDCM and the Monte Carlo simulation of the Bateman equation was too large to give a more reliable value for the lifetime. The lifetime was determined to be smaller than 11 ps.

The lifetimes of the 2_2^+ and 0_2^+ states were analyzed using particle-gated spectra and correcting for the observed feeding from the 4_2^+ state and the 2_3^+ state, respectively, that were determined experimentally. An upper limit of possible unobserved long lived feeding has been estimated by the observation limit and is accounted for in the uncertainty. Due to the direct character of the α-transfer reaction it is however not likely that unobserved long lived feeding plays a larger role. The development of the decay curve of the 0_2^+ state depending on the target-to-stopper distance is shown in Fig. 8.

The lifetime of the 2_1^+ state was measured using particle-γ-γ coincidences and a full gate on both components of the $2_2^+ \rightarrow 2_1^+$ (540 keV) transition. This avoids the complications arising from the analysis of the doublet at 680 keV. Furthermore it excludes the possibility of unobserved long lived feeding but also greatly reduces the statistics, that now become the main contribution to the uncertainty. The lifetime was determined to be 5(2) ps. In Fig. 9 spectra are shown, that demonstrate how the ratio of shifted and unshifted components develops with increasing distance.

With a value for the lifetime of the 2_1^+ it was possible to give an estimation for the lifetime of the 4_1^+ state analyzing the 680 keV doublet. The separation between the $4_1^+ \rightarrow 2_1^+$ and $2_1^+ \rightarrow 0_1^+$ transitions is far smaller than the separation between the respective Doppler-shifted and unshifted
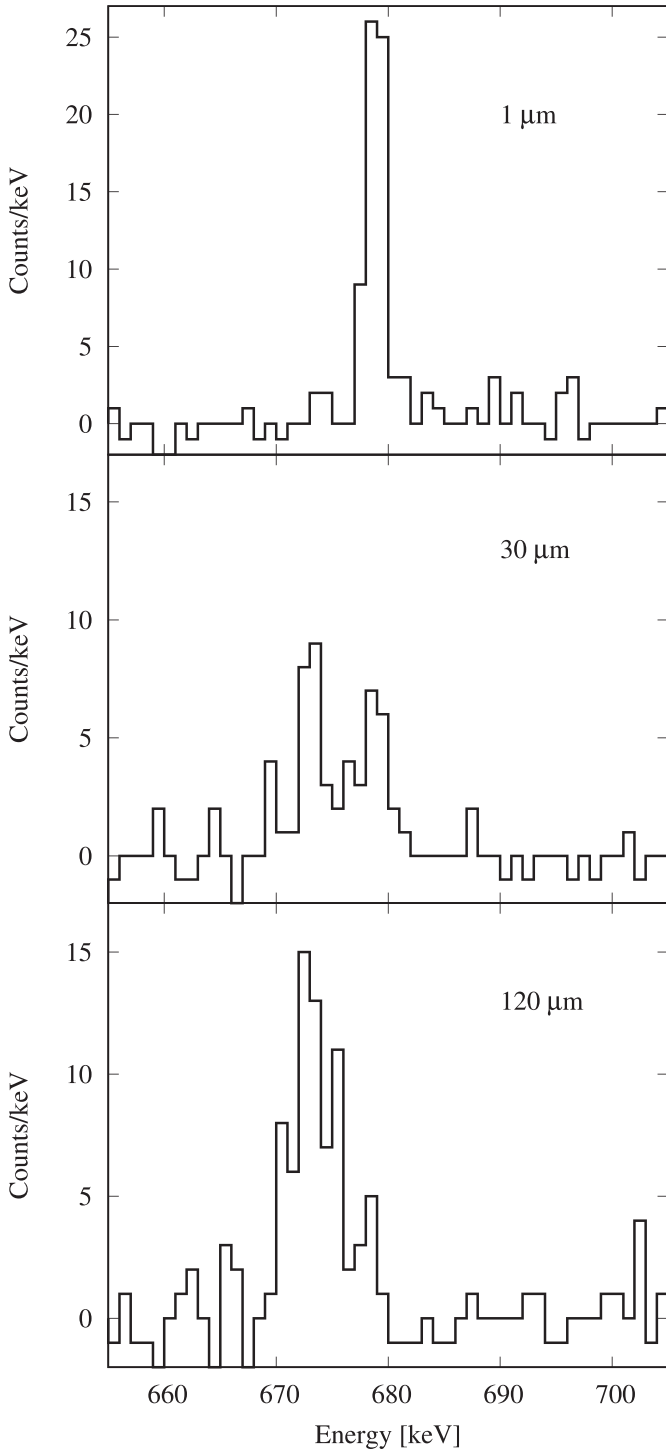
FIG. 9. Spectra of the $2_1^+ \rightarrow 0_1^+$ transition for different relative target-to-stopper distances from detectors at backward angles. A full gate on both components was set on the $2_2^+ \rightarrow 2_1^+$ (540 keV) transition and a solar cell condition. Since the spectra are not Doppler-corrected, the shifted component is significantly broader than the unshifted component.

components so that it was possible to reliably determine the summed intensity of the shifted components of both transitions and the summed intensity of the unshifted components of both transitions. These were used to perform a Monte Carlo

TABLE IV. Lifetime values of the results of the DDCM and Monte Carlo Bateman analysis. The upper limits vary with the observed intensities of the decaying transitions. The results of the two analysis methods are not independent. If a DDCM analysis was possible, the result of the DDCM is used and only crosschecked with the Monte Carlo simulation. The adopted values are indicated. Note that the transitions with energies 1050, 1171 and 1294 keV could not be placed in the level scheme and hence do not appear in Fig. 7.

J_i^π or E_γ	τ (DDCM) [ps]	τ (Bateman) [ps]	Adopted [ps]
2_1^+	5(2)	7(4)	5(2)
0_2^+	69(9)	69(11)	69(9)
2_2^+	12.3(15)	12(2)	12.3(15)
4_1^+		$1 < \tau < 9$	$1 < \tau < 9$
2_3^+		<2	<2
4_2^+	7(2)	4(2)	<11
6_1^+		<8	<8
5_1^-		<10	<10
930		<10	<10
1050		<10	<10
1171		<10	<10
1294		<20	<20
3_1^-		<5	<5
2_4^+		<10	<10
2_5^+		<10	<10

simulation of the Bateman equations together with the known value of the lifetime of the 2_1^+ state to determine the lifetime of the 4_1^+ state. A lower limit of 1 ps and an upper limit of 9 ps were determined for the lifetime of the 4_1^+ state. The value for the lifetime of the 4_1^+ correlates with the value of the lifetime of the 2_1^+ state.

For the remaining states it was only possible to determine upper limits of the lifetimes since they were shorter than the lifetimes measurable in this experiment. The measured lifetimes are summarized in Table IV.

With the new spin assignments, branching ratios, lifetimes, and multipole mixing ratios, absolute transition strengths can be calculated. All experimental findings are summarized in Table V.

IV. DISCUSSION

A level scheme of ^{116}Te using the new experimental data from this study is shown in Fig. 7. Experimental level energies and $B(E2)$ values suggest, that the 0_2^+, 2_2^+, and 4_1^+ states are suitable candidates for a two-phonon triplet within the U(5) limit of the IBM-1 model [34] (compare Fig. 10). A calculation has been performed using the general U(5) Hamiltonian [35]

$$\mathbf{H} = \epsilon \mathbf{n_d} + \alpha \mathbf{n_d}(\mathbf{n_d} + 4) + \beta\left(\tfrac{1}{5}\mathbf{LL} + 2\mathbf{T_3T_3}\right) + \gamma \mathbf{LL} \quad (5)$$

with the parameters $\varepsilon = 0.62$ MeV, $\alpha = -0.015$ MeV, $\beta = 0.011$ MeV, $\gamma = 0.009$ MeV, and $e_B = 10.35$ $e$fm^2 a reasonable agreement of experimental data and IBM-1 prediction was found. The calculations were performed with the ARBMODEL code [36]. Figure 10 shows a comparison of experimental level energies and $B(E2)$ values with results of the calculation. In general, both level ordering and $B(E2)$ values from the

TABLE V. All observed experimental values in ^{116}Te in this study. The branching ratios relatively to the strongest observed decay are given in column "b", β stands for populated in β decay and t stands for populated in transfer reaction.

E_{level} [keV]	J_i^π	E_γ [keV]	E_f [keV]	J_f^π	b	τ [ps]	EL	δ	B(EL) [W.u.]	Reaction
678.8(1)	2_1^+	678.8(1)	0.0	0_1^+	100	5(2)	$E2$		33^{+22}_{-10}	β,t
1059.7(1)	0_2^+	380.9(1)	678.8	2_1^+	100	69(9)	$E2$		43^{+6}_{-5}	β,t
1218.7(1)	2_2^+	539.9(1)	678.8	2_1^+	100	12.3(15)	$E2$	$5.2^{+1.0}_{-0.8}$	41^{+6}_{-5}	β,t
							$M1$		$6^{+4}_{-2} \times 10^{-4}$	
1359.4(3)	4_1^+	680.6(3)	678.8	2_1^+	100	$1 < \tau < 9$	$E2$		$20 < B(E2) < 170$	β,t
1637.3(2)	2_3^+	419	1218.7	2_2^+	< 3	< 2	$M1 + E2$			β
		577.6(1)	1059.7	0_2^+	15(3)		$E2$		> 20	β,t
		958.5(2)	678.8	2_1^+	100(2)		$E2$	$-0.7^{+0.1}_{-0.1}$	> 3	β,t
							$M1$		>0.01	
1811.2(3)	4_2^+	452	1359.4	4_1^+	14(3)	<11	$M1 + E2$			β,t
		592.5(2)	1218.7	2_2^+	35(15)		$E2$		>5	β,t
		1132.4(3)	678.8	2_1^+	100(3)		$E2$		>0.7	β,t
2002.2[a]	6_1^+	643.1[a]	1359.4	4_1^+	100	< 8	$E2$		>27	t
2080.5(2)	0_3^+	443.3	1637.3	2_3^+	< 7		$E2$			β
		861.8(1)	1218.7	2_2^+	49(5)		$E2$			β
		1401.7(4)	678.8	2_1^+	100(7)		$E2$			β
2119.1[a]	3_1^{-} [c]	759.7[b]	1359.4	4_1^+	47(7)	< 5	$E1$[bc]		$>5 \times 10^{-5}$	t
		1441(2)	678.8	2_1^+	100(7)		$E1$[c]		$>1.8 \times 10^{-5}$	t
2149(2)		930(2)	1218.7	2_2^+	100	<10				t
2265.6(5)	2_4^+	1586.8(5)	678.8	2_2^+	100	<10	$M1(+E2)$	$-0.15(15)$	$>7 \times 10^{-4}$	β,t
2339.9[a]	6_2^+	337.9[a]	2002.2	6_1^+	100(11)		$M1 + E2$			t
		980.5[a]	1359.4	4_1^+	83(11)		$E2$			t
2438.2(7)		1759.4(7)	678.8	2_1^+	100					β
2508.6(3)		871.3(2)	1637.3	2_3^+	39(4)		$E2$			β
		1290.0(5)	1218.7	2_2^+	100(15)		$E2$			β
		1829.9(6)	678.8	2_1^+	18(2)		$E2$			β
2556.1[a]	5_1^{-} [b]	1196.7[b]	1359.4	4_1^+	100	<10	$E1$[b]			t
2580.4(4)	2_5^+	769(1)	1811.2	4_2^+	11(6)	<10	$E2$		>0.8	β
		1901.6(4)	678.8	2_1^+	100(11)		$M1(+E2)$	$-0.10(15)$	$>4 \times 10^{-4}$	β,t
2633.4(4)		1414.7(4)	1218.7	2_2^+	43(5)					β
		1954.7(5)	678.8	2_1^+	100(10)					β
2736.5(5)		1517.9(4)	1218.7	2_2^+	100(7)					β
		2057.7(5)	678.8	2_1^+	66(7)					β
		2736(1)	0.0	0_1^+	71(14)					β
2832.8(5)	0_4^+	1195.6(4)	1637.3	2_3^+	42(5)		$E2$			β
		1614.1(5)	1218.7	2_2^+	78(8)		$E2$			β
		2153.8(6)	678.8	2_1^+	100(17)		$E2$			β
2846.7(5)		1628.0(5)	1218.7	2_2^+	100					β
2947.4(6)		1728.7(6)	1218.7	2_2^+	100					β
3179.1(5)		1542.7(5)	1637.3	2_3^+	54(6)					β
		1961.4(4)	1218.7	2_2^+	100(16)					β
unplaced transitions:										
		1050(2)				<10				t
		1171(2)				<10				t
		1294(2)				<20				t

[a]Adopted from [11].

[b]Adopted from [13].

[c]The assignment of 3^- to the level at 2119 keV and the subsequent assignment of E1 to the decay transition to the 2_1^+ state are based on the assignment of E1 to the 760 keV transition by Lönnroth et al. [13]. See text for details.

IBM-1 calculations agree with the experimental values. The most prominent differences are the missing of a candidate for the 3^+ state of the three phonon quintuplet and the placement of the 0_3^+ state. It is however possible, that the correct candidates for the three phonon quintuplet have not been identified

yet. Another difference is the decay pattern of the 2_3^+. The $B(E2, 2_3^+ \rightarrow 2_1^+)$ was measured to be larger than three W.u. in this study, but this transition is forbidden in the IBM-1.

So far, the 0_2^+ was treated as a member of the two phonon triplet of the U(5) limit of the IBM-1. A second possible
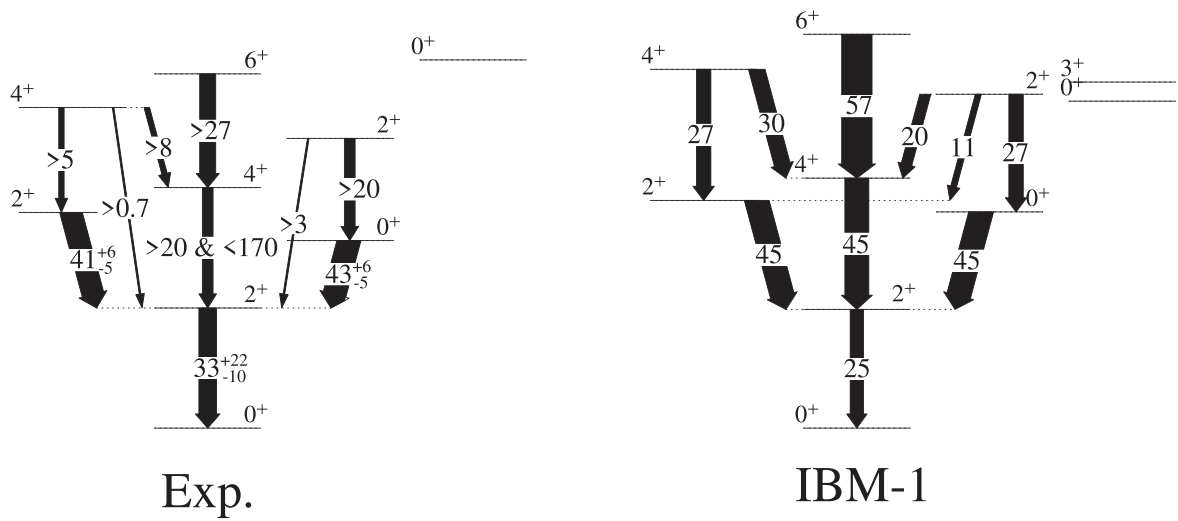
FIG. 10. Comparison of the IBM-1 calculation with the experimental results. $B(E2)$ strengths are given in W.u. For simplicity, for the experimental data the $4_2^+ \rightarrow 4_1^+$ transition is assumed to be a pure $E2$ transition as no multipole mixing ratio was determined.

explanation for the low-lying 0_2^+ state can be intruder states from 4p-2h excitations across the $Z = 50$ proton shell closure. Such intruder states have been suggested in some cases in the Te isotopes (compare, e.g., [1]) but have not been identified unambiguously yet. The strongly collective $E2$ transition from the 2_3^+ state to the 0_2^+ state can be interpreted as the beginning of a band structure on top of the 0_2^+. Further supporting arguments for an intruder structure are the energy systematics of the 0_2^+ and 2_3^+ states in the Te isotopes that show a parabolic behavior with a minimum at midshell ^{118}Te (compare Fig. 11). This behavior has been observed already by Rikovska *et al.* [7] and this study extends the picture by clearly identifying the spin of the candidate states for the intruding 0_2^+ and 2_3^+ state. If the 0_2^+ state is interpreted as a state belonging to an intruding structure, a suiting candidate for a 0_2^+ state belonging to the two phonon triplet of the structure of the ground state is missing.
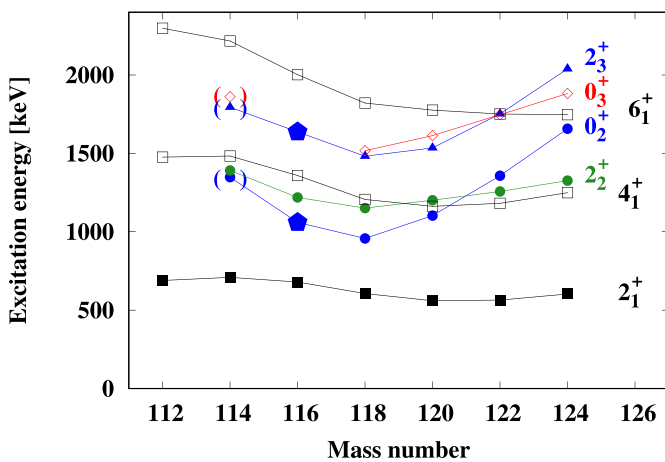

FIG. 11. Systematics of low-lying levels in midshell Te isotopes [11,26,27,31–33]. States where the spin and parity assignment could be improved in this study are marked with a ⬡ symbol. Several states in ^{114}Te are marked in brackets since the spin assignment is tentative.

Both approaches—a description completely within the U(5) limit and the introduction of shape coexistence—provide a sufficient explanation of the experimental data. To further test both hypotheses, more experimental data are needed. For example, other reaction mechanisms could be able to identify suited candidates for the 3^+ and 0^+ member of the three-phonon quintuplet in the U(5) approach. The systematics of the 0_3^+ state along the Te isotopic chain do indeed suggest, that a 0^+ state is missing in ^{116}Te at around 1.5–1.7 MeV (compare Fig. 11). The $B(E2)$ values of transitions in the yrast band were determined in this study only with relatively large uncertainties. More precise values could therefore help to further test the predictions of a description within the U(5) limit.

An enhanced $\rho(E0)$ value of the $0_2^+ \rightarrow 0_1^+$ transition is often an indicator for different shapes of the respective 0^+ states and depends on the mixing of those states [1]. The direct $E0$ transition from the 0_2^+ to the ground state has, however, not been measured yet. More spectroscopy is needed to establish a possible band structure on top of the 0_2^+ state. A candidate for an intruding 4^+ state is missing and hence also the needed in-band decays of the intruding structure. The (^{3}He, n) reactions are also known to strongly populate intruder states [1]. A measurement of the relative cross sections of the direct population of the 0_1^+ and 0_2^+ states is another possible indicator for shape coexistence.

The role that (^{12}C, ^{8}Be) α-transfer reactions play at investigating nuclear structure has not fully been understood so far. Stahl *et al.* [37] find that the ^{12}C(^{136}Xe, ^{140}Ba) ^{8}Be reaction strongly populates the 2_{ms}^+ mixed-symmetry state, though not as strong as predicted by Alonso *et al.* [38]. In this study, the 2_4^+ and 2_5^+ states were populated in the α-transfer reaction and both decay with nearly pure $M1$ transitions to the 2_1^+ state. However, for none of these states a transition to the ground state has been found and the absolute $M1$ strengths are unknown since only an upper limit for the lifetimes was established.

Astier *et al.* [39,40] find that the α-transfer reaction ^{208}Pb(^{18}O, ^{14}C)^{212}Po populates states that can be identified to belong to α clustering structures. They manifest through strong $E1$ transitions to states with the same spin but different parity. Candidates for such states could be the newly discovered states in the transfer reaction in this study, but for many of them, it was not possible to assign multipolarities to the decaying transitions and to determine their spin and parity. Astier also observed a strong population of the 3_1^- state, which could also be observed in this experiment.

V. CONCLUSION

The level structure of low-lying and low spin states in ^{116}Te has been investigated. Several new states were found.

Spins and multipole mixing ratios were measured with the help of angular correlations. Absolute transition strengths of low-lying states have been calculated using lifetimes measured in an RDDS experiment. The resulting data allow an interpretation of the nucleus in the U(5) limit of the IBM-1 but do not contradict the possibility of shape coexistence. To clarify the picture, more experimental data are needed.

[1] P. E. Garrett, M. Zielińska, and E. Clément, An experimental view on shape coexistence in nuclei, Prog. Part. Nucl. Phys. **124**, 103931 (2022).

[2] B. L. Cohen and R. E. Price, Studies of low-lying levels of even-even nuclei with (d, p) and (d, t) reactions, Phys. Rev. **118**, 1582 (1960).

[3] H. Fielding, R. Anderson, C. Zafiratos, D. Lind, F. Cecil, H. Wieman, and W. Alford, 0^+ states observed in Cd and Sn nuclei with the (^{3}He, n) reaction, Nucl. Phys. A **281**, 389 (1977).

[4] R. A. Meyer and L. Peker, Evidence for the coexistence of shapes in even-mass Cd nuclei, Z. Phys. A At. Nucl. **283**, 379 (1977).

[5] P. E. Garrett, T. R. Rodríguez, A. Diaz Varela, K. L. Green, J. Bangay, A. Finlay, R. A. E. Austin, G. C. Ball, D. S. Bandyopadhyay, V. Bildstein, S. Colosimo, D. S. Cross, G. A. Demand, P. Finlay, A. B. Garnsworthy, G. F. Grinyer, G. Hackman, B. Jigmeddorj, J. Jolie, W. D. Kulp *et al.*, Shape coexistence and multiparticle-multihole structures in ^{110,112}Cd, Phys. Rev. C **101**, 044302 (2020).

[6] J. L. Wood, K. Heyde, W. Nazarewicz, M. Huyse, and P. van Duppen, Coexistence in even-mass nuclei, Phys. Rep. **215**, 101 (1992).

[7] J. Rikovska, N. J. Stone, P. M. Walker, and W. B. Walters, Intruder states in even-even Te nuclei, Nucl. Phys. A **505**, 145 (1989).

[8] A. A. Pasternak, J. Srebrny, A. D. Efimov, V. M. Mikhajlov, E. O. Podsvirova, C. Droste, T. Morek, S. Juutinen, G. B. Hagemann, M. Piiparinen, S. Törmänen, and A. Virtanen, Lifetimes in the ground-state band and the structure of ^{118}Te, Euro. Phys. J. A **13**, 435 (2002).

[9] O. Möller, N. Warr, J. Jolie, A. Dewald, A. Fitzler, A. Linnemann, K. O. Zell, P. E. Garrett, and S. W. Yates, E2 transition probabilities in ^{114}Te: A conundrum, Phys. Rev. C **71**, 064324 (2005).

[10] C. Mihai, A. A. Pasternak, S. Pascu, D. Filipescu, M. Ivaşcu, D. Bucurescu, C. Căta Danil, I. Căta-Danil, D. Deleanu, D. G. Ghiţă, T. Glodariu, N. Mărginean, R. Mărginean, A. Negret, T. Sava, L. Stroe, G. Suliman, and N. V. Zamfir, Lifetime measurements by the Doppler-shift attenuation method in the ^{115}Sn($\alpha, n\gamma$)^{118}Te reaction, Phys. Rev. C **83**, 054310 (2011).

[11] J. Blachot, Nuclear Data Sheets for A = 116, Nucl. Data Sheets **111**, 717 (2010).

[12] B. E. Zimmerman, The energy level structures of even-even tellurium and odd-odd iodine and antimony nuclei: ^{114}Te, ^{116}Te, ^{114}I, and ^{114}Sb, Ph.D. thesis, University of Maryland (1992).

[13] T. Lönnroth, A. Virtanen, and J. Hattula, Coexistence of vibrational and quasiparticle structures in neutron-deficient ^{114,115,116,117}Te, Phys. Scr. **34**, 682 (1986).

[14] P. Chowdhury, W. F. Piel, and D. B. Fossan, Collective properties of $1g_{\frac{9}{2}}$ proton-hole excitations: High-spin states in ^{116,118,120,122}Te and ^{120}Xe nuclei, Phys. Rev. C **25**, 813 (1982).

[15] A. Sharma, J. Singh, H. Kaur, J. Goswamy, D. Mehta, N. Singh, P. N. Trehan, E. S. Paul, and R. K. Bhowmik, High spin states in ^{116,118}Te, Z. Phys. A Hadrons and Nuclei **354**, 347 (1996).

[16] J. M. Sears, D. B. Fossan, I. Thorslund, P. Vaska, E. S. Paul, K. Hauschild, I. M. Hibbert, R. Wadsworth, S. M. Mullins, A. V. Afanasjev, and I. Ragnarsson, High-spin spectroscopy of $^{116}_{52}$Te, Phys. Rev. C **55**, 2290 (1997).

[17] C. B. Moon, T. Komatsubara, T. Shizuma, K. Uchiyama, N. Hashimoto, M. Katoh, K. Matsuura, M. Murasaki, Y. Sasaki, H. Takahashi, Y. Tokita, and K. Furuno, In-beam gamma-ray spectroscopy of ^{116}Te, Z. Phys. A Hadrons and Nuclei **358**, 373 (1997).

[18] A. Dewald, O. Möller, and P. Petkov, Developing the recoil distance doppler-shift technique towards a versatile tool for lifetime measurements of excited nuclear states, Prog. Part. Nucl. Phys. **67**, 786 (2012).

[19] T. Alexander and A. Bell, A target chamber for recoil-distance lifetime measurements, Nucl. Instrum. Methods **81**, 22 (1970).

[20] L. Netterdon, V. Derya, J. Endres, C. Fransen, A. Hennig, J. Mayer, C. Müller-Gatermann, A. Sauerwein, P. Scholz, M. Spieker, and A. Zilges, The γ-ray spectrometer HORUS and its applications for nuclear astrophysics, Nucl. Instrum. Methods Phys. Res. A **754**, 94 (2014).

[21] J. K. Smith, A. D. MacLean, W. Ashfield, A. Chester, A. B. Garnsworthy, and C. E. Svensson, Gamma–gamma angular correlation analysis techniques with the Griffin spectrometer, Nucl. Instrum. Methods Phys. Res. A **922**, 47 (2019).

[22] L. Knafla, A. Esmaylzadeh, A. Harter, J. Jolie, U. Köster, M. Ley, C. Michelagnoli, and J.-M. Régis, Development of a new $\gamma-\gamma$ angular correlation analysis method using a symmetric

ring of clover detectors, Nucl. Instrum. Methods Phys. Res. A **1042**, 167463 (2022).

[23] H. J. Rose and D. M. Brink, Angular distributions of gamma rays in terms of phase-defined reduced matrix elements, Rev. Mod. Phys. **39**, 306 (1967).

[24] S. Robinson, How reliable are spins and δ-values derived from directional correlation experiments? Nucl. Instrum. Methods Phys. Res. A **292**, 386 (1990).

[25] G. M. Gowdy, A. C. Xenoulis, J. L. Wood, K. R. Baker, R. W. Fink, J. L. Weil, B. D. Kern, K. J. Hofstetter, E. H. Spejewski, R. L. Mlekodaj, H. K. Carter, W. D. Schmidt-Ott, J. Lin, C. R. Bingham, L. L. Riedinger, E. F. Zganjar, K. S. R. Sastry, A. V. Ramayya, and J. H. Hamilton, On-line mass separator investigation of the new isotope 2.9-sec ^{116}I, Phys. Rev. C **13**, 1601 (1976).

[26] K. Kitao, Nuclear Data Sheets for A = 118, Nucl. Data Sheets **75**, 99 (1995).

[27] K. Kitao, Y. Tendow, and A. Hashizume, Nuclear Data Sheets for A = 120, Nucl. Data Sheets **96**, 241 (2002).

[28] M. Beckers, A. Dewald, C. Fransen, L. Kornwebel, C.-D. Lakenbrink, and F. von Spee, Revisiting the measurement of absolute foil-separation for RDDS measurements and introduction of an optical measurement method, Nucl. Instrum. Methods Phys. Res. A **1042**, 167416 (2022).

[29] B. Saha, Bestimmung der Lebensdauern kollektiver Kernanregungen in ^{124}Xe und Entwicklung von entsprechender Analysesoftware, Ph.D. thesis, Universität zu Köln (2004).

[30] A. Esmaylzadeh, V. Karayonchev, K. Nomura, J. Jolie, M. Beckers, A. Blazhev, A. Dewald, C. Fransen, R.-B. Gerst, G. Häfner, A. Harter, L. Knafla, M. Ley, L. M. Robledo, R. Rodríguez-Guzmán, and M. Rudigier, Lifetime measurements to investigate γ softness and shape coexistence in ^{102}Mo, Phys. Rev. C **104**, 064314 (2021).

[31] J. Blachot, Nuclear Data Sheets for A = 114, Nucl. Data Sheets **113**, 515 (2012).

[32] T. Tamura, Nuclear Data Sheets for A = 122, Nucl. Data Sheets **108**, 455 (2007).

[33] J. Katakura and Z. Wu, Nuclear Data Sheets for A = 124, Nucl. Data Sheets **109**, 1655 (2008).

[34] A. Arima and F. Iachello, Interacting boson model of collective states I. The vibrational limit, Ann. Phys. **99**, 253 (1976).

[35] F. Iachello and A. Arima, *The Interacting Boson Model*, Cambridge Monographs on Mathematical Physics (Cambridge University Press, Cambridge, UK, 1987).

[36] S. Heinze, Eine Methode zur Lösung beliebiger bosonischer und fermionischer Vielteilchensysteme, Ph.D. thesis, Universität zu Köln (2008).

[37] C. Stahl, J. Leske, C. Bauer, D. Bazzacco, E. Farnea, A. Gottardo, P. R. John, C. Michelagnoli, N. Pietralla, M. Reese, E. Şahin, B. Birkenbach, A. Bracco, F. C. L. Crespi, G. de Angelis, P. Désesquelles, J. Eberth, A. Gadea, A. Görgen, J. Grebosz *et al.*, Population of the 2^+_{ms} mixed-symmetry state of ^{140}Ba with the α-transfer reaction, Phys. Rev. C **92**, 044324 (2015).

[38] C. E. Alonso, J. M. Arias, L. Fortunato, N. Pietralla, and A. Vitturi, Population of mixed-symmetry states via α transfer reactions, Phys. Rev. C **78**, 017301 (2008).

[39] A. Astier, P. Petkov, M.-G. Porquet, D. S. Delion, and P. Schuck, Novel manifestation of α-clustering structures: New "$\alpha + {}^{208}$Pb" states in ^{212}Po revealed by their enhanced $E1$ decays, Phys. Rev. Lett. **104**, 042701 (2010).

[40] A. Astier, P. Petkov, M.-G. Porquet, D. S. Delion, and P. Schuck, Coexistence of "$\alpha + {}^{208}$Pb" cluster structures and single-particle excitations in $^{212}_{84}$Po$_{128}$, Eur. Phys. J. A **46**, 165 (2010).

4.2 Experiments on ^{118}Te

The second nucleus that was studied is ^{118}Te, lying exactly at neutron mid-shell $N = 66$. This draws special attention to ^{118}Te in the search for shape coexistence in this region as possible $2p - 2h$ intruder configurations are expected to exhibit an energy minimum at mid-shell. In fact, lifetime measurements of yrast and off-yrast states in this nucleus have been already performed in Refs. [31, 36, 71]. However, the only half-life value reported for the 0_2^+ state of $t_{1/2}(0_2^+) = 55(45)$ ps [71] has an uncertainty of over 80% and is only a preliminary value. Also the lifetime value of the 2_1^+ state reported in Ref. [36] of $\tau = 8.8(14)$ ps has a relatively large uncertainty of 16%. The uncertainties of these experimental results limit the power of any conclusion drawn from them and thus motivate a more precise remeasurement of these lifetimes. In this study, two different RDDS lifetime measurements were performed on ^{118}Te. In a first measurement, the lifetimes of yrast states in ^{118}Te were measured following the ^{100}Mo(^{23}Na,4np)^{118}Te reaction and in a second experiment lifetimes of low-spin off-yrast states were studied following the ^{114}Sn(^{12}C,^{8}Be)^{118}Te α-transfer reaction.

4.2.1 Experimental details

Both experiments were conducted at the 10 MV FN tandem accelerator in Cologne. In the first experiment, the fusion-evaporation reaction ^{100}Mo(^{23}Na,4np)^{118}Te was used to produce ^{118}Te isotopes where the beam had an energy of 94 MeV. The target was a highly enriched, self-supporting ^{100}Mo foil with a thickness of 1.0 mg/cm². A 6.5 mg/cm² thick tantalum foil was used to stop the recoiling products of the fusion-evaporation reaction. Target and stopper foil were mounted in the Cologne coincidence plunger device. Data were taken for eleven different target-to-stopper distances between 300 μm and electrical contact. The target-to-stopper distances were monitored and held constant during the experiment using the capacitance method [41, 42]. A total of eleven High-purity germanium detectors were placed, divided into two rings at angles of 45° and 142°, to detect γ-rays following the fusion-evaporation reaction. The mean recoil velocity of ^{118}Te was determined to be $v/c = 1.46(7)$ % by measuring the Doppler-shift of in-flight emitted γ-rays.

For the second experiment, the ^{114}Sn(^{12}C,^{8}Be)^{118}Te α-transfer reaction with a beam energy of 44 MeV was used to populate nuclei of interest. The target material was 65 % isotopically enriched ^{114}Sn evaporated on a 1.5 mg/cm² thick tantalum foil. The stopper foil was a 4.0 mg/cm² thick tantalum foil. Data were recorded for six different target-to-stopper distances between 200 μm and electrical contact, where the distance was again monitored and held constant using the capacitance method [41, 42]. The Cologne CATHEDRAL spectrometer was used to record γ-rays following the α-transfer reaction. The spectrometer was equipped with 18 HPGe detectors, with six detectors placed in each of three different rings at 30°, 55° and 150°, respectively. Under backward angles, four solar cells were

installed inside the Cologne coincidence plunger device to record α particles stemming from the immediate decay of ^{8}Be into two α particles. The recoil velocity was determined to be $v/c = 1.0(1)\,\%$. The solar cells were again covered with a 40 µm aluminum foil, that prevented heavier charged particles from entering into the solar cells.

It has to be noted that during the second experiment, aluminum parts of the collimator that was positioned at the entrance of the plunger device were unintentionally exposed to the beam leading to a massive background of events stemming from fusion-evaporation reactions of the beam with the aluminum. This problem was unfortunately not identified during the experiment and could therefore not be corrected during the experiment. This negatively affected the measurement in two ways. The beam intensity had to be lowered to reduce the count rates and consequently dead times in the HPGe detectors. Furthermore, it lead to more random time coincidences that overall worsened the quality of the data.

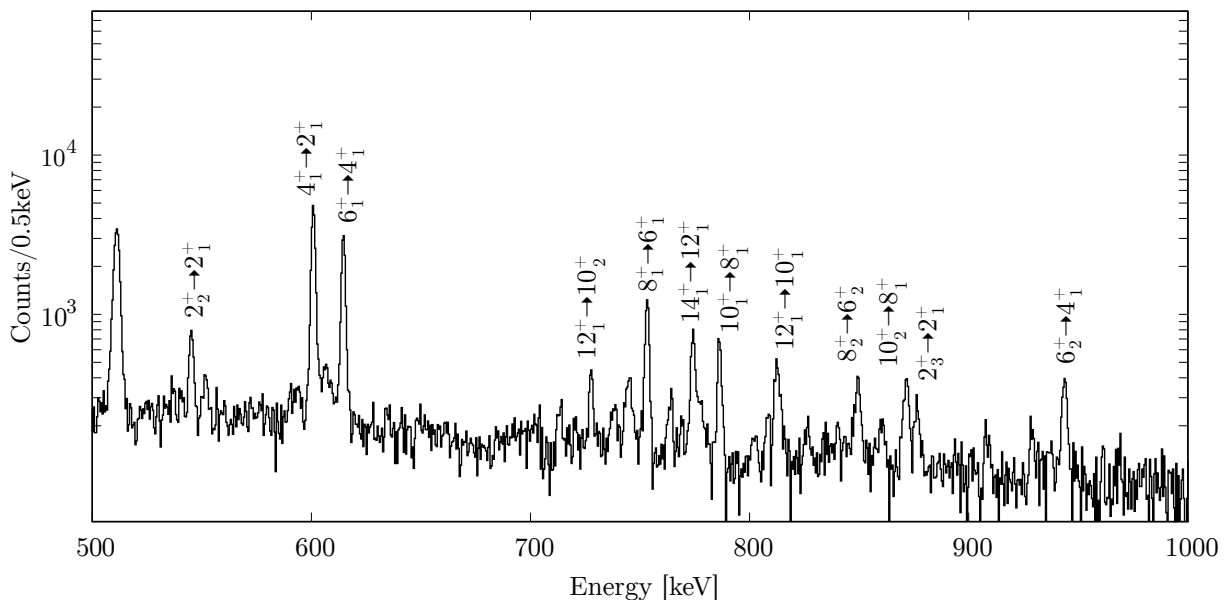### 4.2.2 Spectroscopic analysis of the fusion-evaporation experiment

Figure 4.1: Coincidence spectrum showing γ-rays observed in the ^{100}Mo(^{23}Na,4np)^{118}Te fusion-evaporation reaction at backward angles. A narrow energy gate was set on the unshifted component of the $2_1^+ \to 0_1^+$ (606 keV) transition avoiding contaminations from doublets. The relative target-to-stopper distance was 1 µm. Note the logarithmic scale of the y-axis.

The recorded data of the fusion-evaporation reaction are sorted ringwise in γ-γ matrices. In the ^{100}Mo(^{23}Na,4np)^{118}Te fusion-evaporation reaction, not only ^{118}Te, but also several other nuclei in the region are populated. The highest cross sections are observed for the 5n, 4n and 4np, 3np channels to the isotopes ^{118,119}I and ^{118,119}Te. Figure 4.1 shows a coincidence spectrum where a gate is set on the unshifted component of the $2_1^+ \to 0_1^+$ (606 keV) transition in ^{118}Te. The spectrum is obtained at the smallest relative target-to-

stopper distance of 1 µm. Since both ^{118}I and ^{118}Te are populated in the fusion-evaporation reaction, the observed γ-rays in ^{118}Te do not only stem from direct population in fusion-evaporation, but also from population in the β decay of ^{118}I. This explains for example the presence of the $2_2^+ \to 2_1^+$ (545 keV) and $2_3^+ \to 2_1^+$ (876 keV) transitions in Fig. 4.1 that are not expected to be strongly populated in such fusion-evaporation reactions. Figure 4.2 shows an excerpt of the observed level scheme of ^{118}Te in the ^{100}Mo(^{23}Na,X)Y reaction. Of all observed transitions in ^{118}Te, only transitions in the ground-state band show significant shifted components. A second band that has been identified as a two-quasi-particle band by Pasternak *et al.* [36] is populated in the ^{100}Mo(^{23}Na,4np)^{118}Te fusion-evaporation reaction, but there is no observable shifted component in any of the transitions for any target-to-stopper distance in this band. This is probably caused by delayed feeding; it is however not possible to identify the delayed feeder. A similar behavior is reported by Juutinen *et al.* [72] in the ^{104}Ru(^{18}O,4n)^{118}Te reaction.
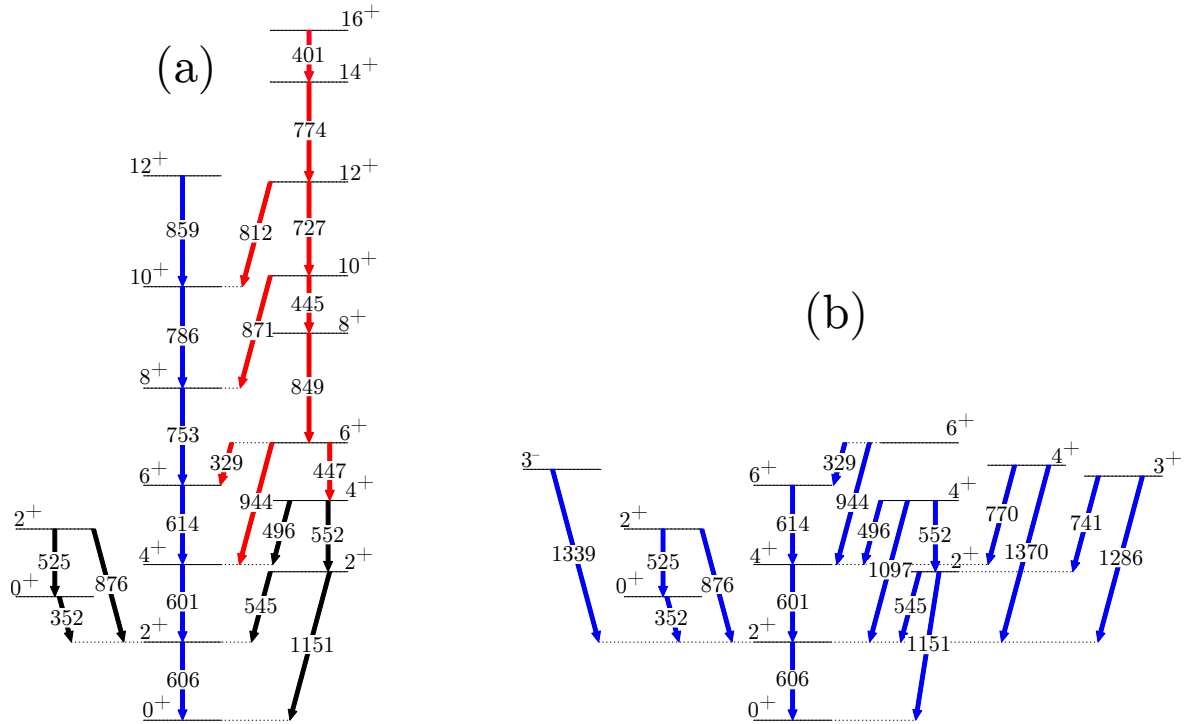
Figure 4.2: Excerpts of the observed level schemes of ^{118}Te in the ^{100}Mo(^{23}Na,4np)^{118}Te fusion-evaporation reaction (a) and the ^{114}Sn(^{12}C,^{8}Be)^{118}Te α-transfer reaction (b). For blue transitions, a shifted component was observed in the experiment. For red transitions no shifted component was observed, presumably because of delayed feeding. For black transitions, the initial states are mainly populated in β-decay and hence no shifted component was observed. Note that the different initial populations and observation limits lead to some transitions being observed in only one of the two experiments.

4.2.3 Lifetime analysis of the fusion-evaporation experiment

Figure 4.3: *Left*: Coincidence spectra for three different relative target-to-stopper distances showing the development of the shifted and unshifted component of the $2_1^+ \rightarrow 0_1^+$ transition (606 keV). The gate condition was set on the shifted component of the $4_1^+ \rightarrow 2_1^+$ transition (601 keV) for 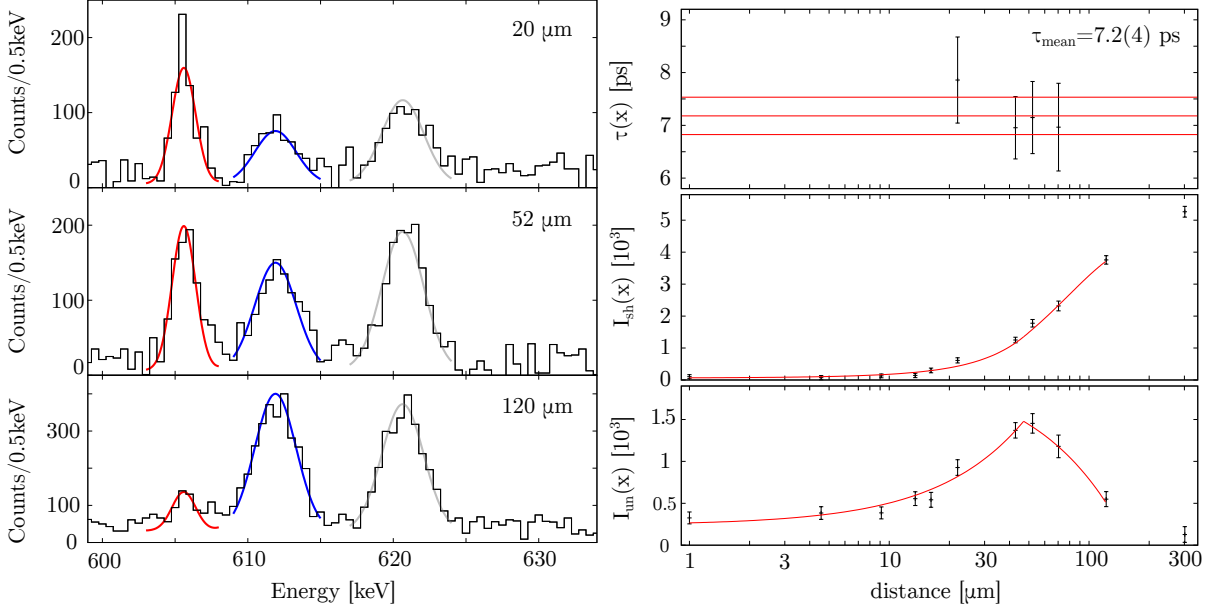HPGe detectors at backward angles. The spectra were recorded at forward angles. The fit of the unshifted component is shown in red, the fit of the shifted component is shown in blue. A fit of the shifted component of the $6_1^+ \rightarrow 4_1^+$ transition (614 keV) is shown in grey. Note that the unshifted component of the $6_1^+ \rightarrow 4_1^+$ transition (614 keV) is not present since the gate condition is set on the shifted component of the $4_1^+ \rightarrow 2_1^+$ transition (601 keV) only.
Right: Lifetime determination of the 2_1^+ state with NAPATAU [73]: For this analysis a gate was set on the shifted component of the $4_1^+ \rightarrow 2_1^+$ (601 keV) transition using HPGe detectors at backward angles. The top panel shows the different lifetime values obtained for different target-to-stopper distances. The middle and bottom panel show the development of the shifted and unshifted component of the $2_1^+ \rightarrow 0_1^+$ (606 keV) transition. Note that the uncertainty of the lifetime value shown in the top panel does only include the statistical uncertainty stemming from the different lifetime values obtained at different distances.

The lifetime analysis of the fusion-evaporation experiment is performed employing the DDC method using γ-γ matrices (compare Sec. 2.2). The presence of delayed feeding and population of ^{118}Te in β decay introduces large unshifted components of the transitions of interest. For the lifetime analysis, gates on shifted components of feeding transitions are used that avoid the subtraction of those unshifted components and additionally fix the feeding pattern. The high γ-ray line density in the region around 600 keV poses another challenge: the transition energies of the $2_1^+ \rightarrow 0_1^+$ (606 keV), $4_1^+ \rightarrow 2_1^+$ (601 keV) and $6_1^+ \rightarrow 4_1^+$ (614 keV) transitions are close. Therefore, it is not easy to find energy gates that contain only the flight component of only one transition and also produce clean coincidence

spectra with sufficient statistics.

To correct for the different beam intensities and measuring durations of the measurements with different target-to-stopper distances, a normalization is performed, where the relative amount of detected events were determined. Additionally, a width calibration of the shifted and unshifted components is performed using in-beam data that is used in the fit procedures of the lifetime analysis.

Lifetime analysis of the 2_1^+ *state*: To perform the lifetime analysis of the 2_1^+ state, a gate is set on the flight component of the $4_1^+ \rightarrow 2_1^+$ (601 keV) transition. This gate could only be set for HPGe detectors at backward angles. In forward angles, the flight component of the $4_1^+ \rightarrow 2_1^+$ (601 keV) transition overlaps with the stop component of the $2_1^+ \rightarrow 0_1^+$ (606 keV) transition. The analysis is only performed in forward angles, since in backward angles the flight component of the $6_1^+ \rightarrow 4_1^+$ (614 keV) transition overlaps with the stop component of the $2_1^+ \rightarrow 0_1^+$ (606 keV) transition. In forward angles, the flight component of the $2_1^+ \rightarrow 0_1^+$ (606 keV) transition would overlap with the stop component of the $6_1^+ \rightarrow 4_1^+$ (614 keV) transition, but the gate on the flight component of the $4_1^+ \rightarrow 2_1^+$ (601 keV) transition can only be in coincidence with the flight component of the $6_1^+ \rightarrow 4_1^+$ (614 keV) transition and a stop component is hence not present (compare Fig. 4.3). Thus, the forward angles can be used for the lifetime analysis. The left hand side of Fig. 4.3 shows exemplary spectra, where the development of the intensities of flight and stopped component can be observed. The decay curves are shown on the right hand side of Fig. 4.3. The analysis is performed with the help of the program NAPATAU [73] resulting in a lifetime value of 7.2(4) ps. The uncertainty calculated by NAPATAU includes only the statistical uncertainty stemming from the different lifetime values obtained at different distances. Taking into account also the uncertainty of the recoil velocity results in a final lifetime value of $\tau(2_1^+) = 7.2(6)$ ps.

Lifetime analysis of the 4^+ *state*: In this analysis, only the gate on the flight component of the $6_1^+ \rightarrow 4_1^+$ (614 keV) transition under forward angles is used. Again, the gate under backward angles is contaminated by the stop component of the $2_1^+ \rightarrow 0_1^+$ (606 keV) transition. In the coincidence spectra, the shifted component of the $4_1^+ \rightarrow 2_1^+$ (601 keV) transition overlaps with the unshifted component of the $2_1^+ \rightarrow 0_1^+$ (606 keV) transition at forward angles and the unshifted component of the $4_1^+ \rightarrow 2_1^+$ (601 keV) transition overlaps with the shifted component of the $2_1^+ \rightarrow 0_1^+$ (606 keV) transition at backward angles (compare Fig. 4.4). However, the total intensity of the $4_1^+ \rightarrow 2_1^+$ (601 keV) transition and $2_1^+ \rightarrow 0_1^+$ (606 keV) transition have to be equal if a gate condition is set on the $6_1^+ \rightarrow 4_1^+$ (614 keV) transition. This information can be used to determine the combined intensity of shifted and unshifted component of the $4_1^+ \rightarrow 2_1^+$ (601 keV) transition by integrating all components of the $2_1^+ \rightarrow 0_1^+$ (606 keV) transition and $4_1^+ \rightarrow 2_1^+$ (601 keV) transition together and dividing the result by two. This result is then used to obtain reliable values for the shifted and unshifted components of the $4_1^+ \rightarrow 2_1^+$ (601 keV) transition since a fit of the shifted component is possible. Spectra used in this analysis are shown in shown
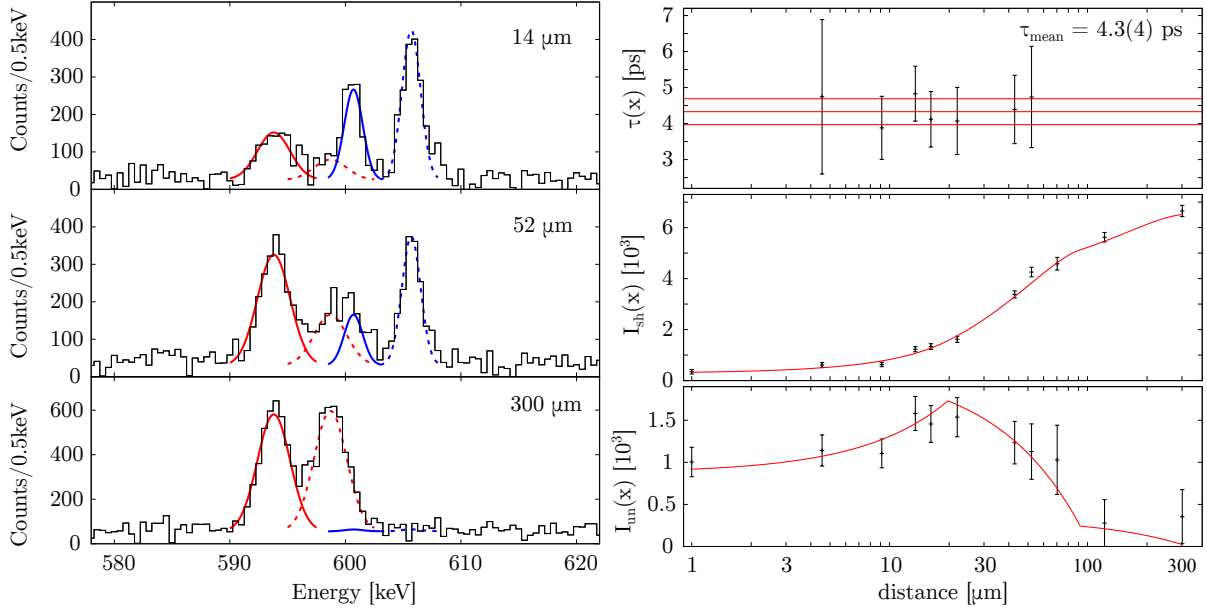
Figure 4.4: *Left*: Coincidence spectra for different relative target-to-stopper distances showing the development of the shifted and unshifted component of the $4_1^+ \to 2_1^+$ (601 keV) transition. The fit of the $4_1^+ \to 2_1^+$ (601 keV) transition is shown in solid lines. In dashed lines, the fit of the $2_1^+ \to 0_1^+$ (606 keV) transition is shown. Fits of shifted components are marked in blue, fits of unshifted components are marked in red. The gate condition was set on the shifted component of the $6_1^+ \to 4_1^+$ (614 keV) transition at forward angles. The spectra were recorded at backward angles.

Right: Lifetime determination of the 4_1^+ state: For this analysis a gate was set on the shifted component of the $6_1^+ \to 4_1^+$ (614 keV) transition. The top panel shows the different lifetime values obtained for different target-to-stopper distances. The middle and bottom panel show the development of the shifted and unshifted component of the $4_1^+ \to 2_1^+$ (601 keV)transition. Note that the uncertainty of the lifetime value shown in the top panel does only include the statistical uncertainty stemming from the different lifetime values obtained at different distances.

in Fig. 4.4. The resulting decay curves and the analysis with NAPATAU are also shown in Fig. 4.4. A lifetime value of 4.3(4) ps is determined using data recorded at backward angles while the analysis using data recorded at forward angles gives a lifetime value of 4.5(3) ps. Taking into account also the uncertainties stemming from the recoil velocity a final, mean lifetime value of $\tau(4_1^+) = 4.4(4)$ ps is determined.

Lifetime analysis of higher-lying states: For various reasons it is not possible to determine the lifetimes of higher-lying states. The $6_1^+ \to 4_1^+$ (614 keV) transition is again contaminated by the $2_1^+ \to 0_1^+$ (606 keV) transition and the higher-lying yrast states are less populated. Additionally, the determined offset of about 20 μm corresponds to a flight time of about 5 ps. All lifetimes of excited states that have an effective lifetime shorter than 5 ps are difficult to measure. In the coincidence spectra obtained through gates on flight components from above, the transitions in the yrast band show no observable stopped component even for short target-to-stopper distances. This means that the lifetimes of higher-lying yrast

states are too short to be measured with this setup and experimental conditions. This observation is in agreement with the lifetime values reported for yrast states in Ref. [36].

4.2.4 Spectroscopic analysis of the transfer experiment
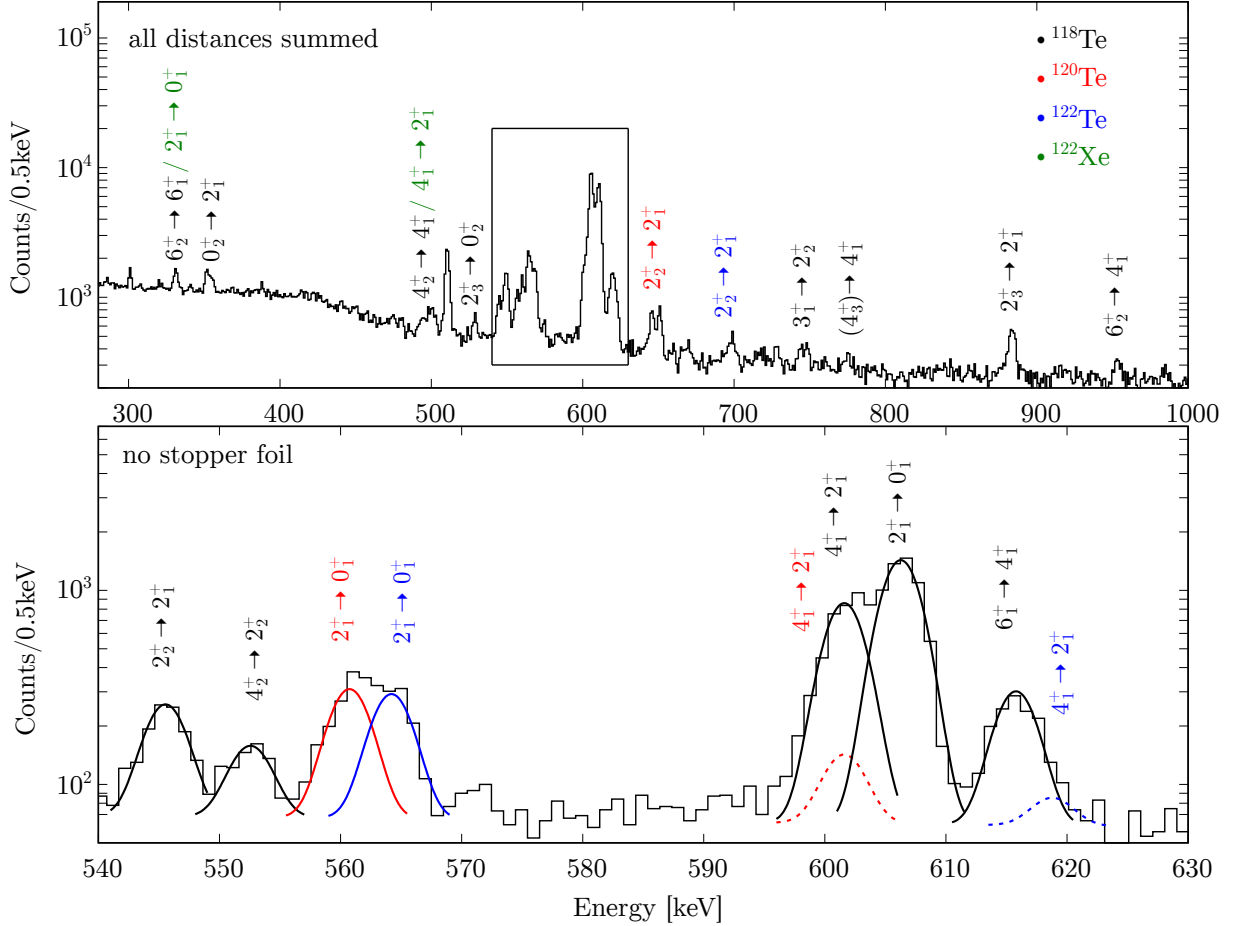
Figure 4.5: Coincidence spectra measured at 30° with respect to the beam axis with the CATHE-DRAL spectrometer in the ^{114}Sn(^{12}C,^{8}Be)^{118}Te α-transfer reaction. A gate condition is set on the detection of a particle in the solar-cell array:
Top: The spectra of all target-to-stopper distances were summed. In the resulting γ-ray spectrum, not only transitions in ^{118}Te were observed but also transitions belonging to ^{120}Te, ^{122}Te and ^{122}Xe. These transitions are marked with different colors. Lines show in general both shifted and unshifted component. The region between 540 keV and 630 keV has a very high line density and is highlighted by a box.
Bottom: Measurement with no stopper foil focussing on the region between 540 keV and 630 keV. Since there is not stopper foil present, all γ-rays are shifted and no stopped component were observed. This simplifies the spectrum significantly. For illustrative purposes, the shifted γ-rays are shown on their nominal position. (Note that this is not a proper Doppler correction that would take into account the different kinematics resulting from the detection in different solar cells.) Dotted fits mark lines that are assumed to be present, but were obscured by more intense lines.

For the analysis of the ^{114}Sn(^{12}C,^{8}Be)^{118}Te α-transfer reaction, data are sorted in particle-γ matrices. Unfortunately, the statistics are not sufficient for an analysis using particle-γ-γ matrices. Figure 4.5 shows γ-ray spectra in coincidence with particle detection. Since heavier particles are stopped in the aluminum foil screening the solar cells, only γ rays stemming from reactions involving the production of α particles can be observed in coincidence with particle detection. In the spectra, not only γ-ray transitions in ^{118}Te are visible, but also γ-ray transitions in ^{120}Te and ^{122}Te. These stem from ^{116}Sn and ^{118}Sn impurities of the ^{114}Sn target material that was only approx. 65 % isotopically enriched. Additionally, γ-ray transitions in ^{122}Xe are present stemming from the fusion-evaporation reaction ^{114}Sn(^{12}C,α)^{122}Xe. To determine the intensities of the observed γ lines in the ^{114}Sn(^{12}C,^{8}Be)^{118}Te α-transfer reaction, the measurement without a stopper is used. This measurement has the advantage, that the intensities of the γ-ray transitions are not spread over two components. Table 4.1 gives all observed γ-rays of ^{118}Te. The intensities of the $4_1^+ \to 2_1^+$ (601 keV) and $6_1^+ \to 4_1^+$ (614 keV) transitions in ^{118}Te have to be corrected for contaminations from the $4_1^+ \to 2_1^+$ (601 keV) and $6_1^+ \to 4_1^+$ (615 keV) transitions in ^{120}Te. These corrections are made using the known intensities of the $4_1^+ \to 2_1^+$ (601 keV) and $6_1^+ \to 4_1^+$ (615 keV) transitions in the α-transfer reaction ^{116}Sn(^{12}C,^{8}Be)^{120}Te (compare Sec. 4.3 and Tab. 4.4). The intensity of the $4_1^+ \to 2_1^+$ (617 keV) transition in ^{122}Te is estimated from the observed $2_1^+ \to 0_1^+$ (564 keV) transition in ^{122}Te and assuming a similar population pattern to the one observed in ^{120}Te. However, it is not possible to correct for contaminations stemming from transitions in ^{122}Xe. Unfortunately, the $2_1^+ \to 0_1^+$ (331 keV) transition and the $4_1^+ \to 2_1^+$ (497 keV) transition in ^{122}Xe contaminate the $6_2^+ \to 6_1^+$ (329 keV) transition and $4_2^+ \to 4_1^+$ (497 keV) transition in ^{118}Te. For the intensities of these transitions, only an upper limit was determined.

Table 4.1: Observed transitions in the α-transfer reaction ^{114}Sn(^{12}C,^{8}Be)^{118}Te. Transition intensities are given relative to the intensity of the $2_1^+ \to 0_1^+$ (606 keV) transition. Spin and parity assignments are adopted from Ref. [31]. The data for the transition energies are taken from Refs. [28, 31] and rounded to full keVs.

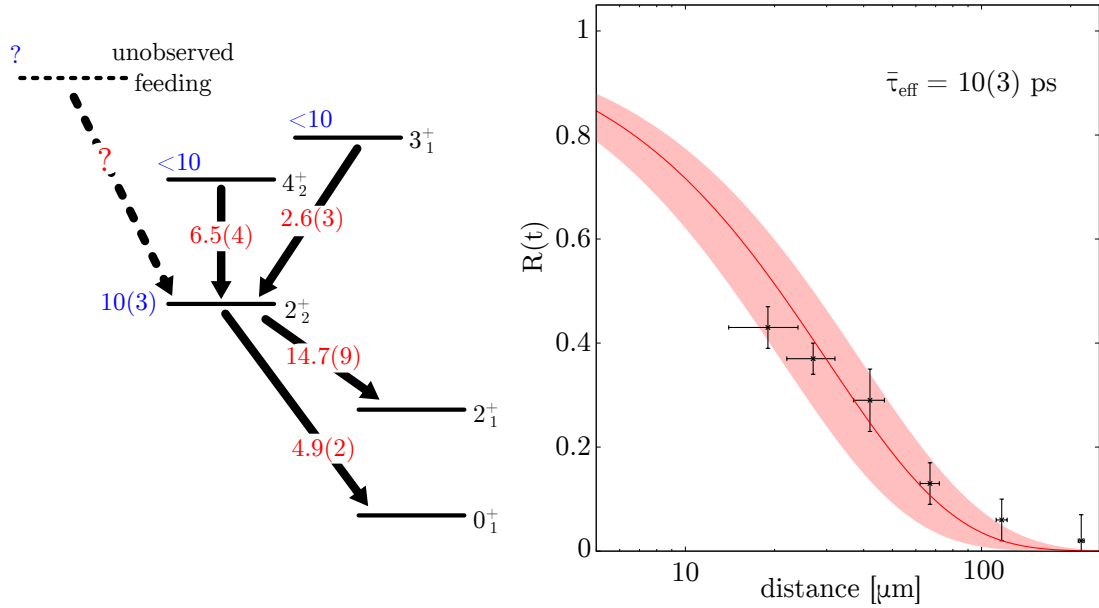| J_i^π	J_f^π	E_γ [keV]	rel. intensity	J_i^π	J_f^π	E_γ [keV]	rel. intensity
6_2^+	6_1^+	329	<4	4_3^+	4_1^+	770	1.5(2)
0_2^+	2_1^+	352	4.5(6)	2_3^+	2_1^+	876	6.3(19)
4_2^+	4_1^+	497	<5	6_2^+	4_1^+	943	1.6(4)
2_3^+	0_2^+	524	2.0(5)	4_2^+	2_1^+	1098	1.5(2)
2_2^+	2_1^+	545	14.7(9)	2_2^+	0_1^+	1151	4.9(2)
4_2^+	2_2^+	551	6.5(4)	$(1,2)^+$	2_1^+	1257	1.9(6)
4_1^+	2_1^+	601	56(5)	3_1^+	2_1^+	1286	1.3(6)
2_1^+	0_1^+	606	100(2)	3_1^-	2_1^+	1338	3.9(9)
6_1^+	4_1^+	614	14(5)	4_3^+	2_1^+	1370	4.9(10)
3_1^+	2_2^+	741	2.6(3)	$(2,3)^+$	2_1^+	1414	2.9(8)

4.2.5 Lifetime analysis of the transfer experiment

Figure 4.6: *Left*: Scheme of transitions populating and depopulating the 2_2^+ state in ^{118}Te observed in the ^{114}Sn(^{12}C,^{8}Be)^{118}Te α-transfer reaction. Intensities of the transitions (red) are given in percentages of the intensity of the $2_1^+ \rightarrow 0_1^+$ (606 keV) transition, information on effective lifetimes (blue) relevant to the lifetime analysis are given in picoseconds.
Right: Decay curve of the $2_2^+ \rightarrow 2_1^+$ (545 keV) transition in ^{118}Te observed in the ^{114}Sn(^{12}C,^{8}Be)^{118}Te transfer reaction resulting in an effective lifetime of 10(3) ps. Note that the uncertainties of the distances result from the uncertainty of the offset. The uncertainties of relative distances are much smaller. See text for details.

It is necessary to reliably determine the positions and intensities of shifted and unshifted components of a γ-ray transition in order to perform a successful lifetime analysis of an RDDS experiment. The many contaminations in the region around 600 keV unfortunately mean, that this is not possible for any of the populated yrast states in ^{118}Te. On the other hand, many of the transitions depopulating the off-yrast states did not show an unshifted component for any target-to-stopper distance for which a measurement was performed. In those cases, only an upper limit of the lifetime was determined. A determination of shifted and unshifted component was possible for the $0_2^+ \rightarrow 2_1^+$ (352 keV) transition and for the $2_2^+ \rightarrow 2_1^+$ (545 keV) transition. For the lifetime analysis of the 0_2^+ state and the 2_2^+ state, absolute target-to-stopper distances need to be known since an analysis with the DDCM was not possible. The offset is determined to be 17(5) μm using the capacitance method as described in Refs. [42, 43] and Sec. 2.1.1.

The decay curve of the $2_2^+ \rightarrow 2_1^+$ (545 keV) transition is determined using a combination of data from the ring at 30° and the ring at 150° that are placed the furthest from 90°. In forward angles, the shifted component is contaminated by the unshifted component

of the $4_2^+ \rightarrow 2_2^+$ (552 keV) transition. In backward angles, the unshifted component is contaminated by the shifted component of the $4_2^+ \rightarrow 2_2^+$ (552 keV) transition. Therefore, the intensity of the shifted component is determined from spectra recorded at backward angles and the unshifted component from spectra recorded at forward angles. These data are then corrected for the different efficiencies of the two rings. From these data, an effective lifetime of $\tau_{eff}(2_2^+) = 10(3)$ ps is determined (see Fig. 4.6).

The effective lifetime of the 2_2^+ state still has to be corrected for feeding to obtain a "real" lifetime value. The main feeding contributions stem from the $4_2^+ \rightarrow 2_2^+$ (552 keV) transition and $3_1^+ \rightarrow 2_2^+$ (741 keV) transition (see Fig. 4.6). For the lifetimes of the 3_1^+ state and 4_2^+ state, lower limits of $\tau(3_1^+) > 2.5$ ps and $\tau(4_2^+) > 1$ ps were determined by Mihai *et al* [31]. In this experiment, upper limits are determined for the lifetimes of the 3_1^+ state and 4_2^+ state. The intensity of the $3_1^+ \rightarrow 2_2^+$ (741 keV) transition is rather weak and no unshifted component is identified, even for the shortest target-to-stopper distance. Thus an upper limit of $\tau(3_1^+) < 10$ ps is determined for the lifetime of the 3_1^+ state. The $4_2^+ \rightarrow 2_2^+$ (552 keV) transition is flanked by the more intense $2_2^+ \rightarrow 2_1^+$ (545 keV) transition and $2_1^+ \rightarrow 0_1^+$ (560 keV) transition in ^{120}Te (compare Fig. 4.5). In spectra with shifted and unshifted components, both components of the $4_2^+ \rightarrow 2_2^+$ (552 keV) transition are thus contaminated. However, the relatively long effective lifetime of the $2_1^+ \rightarrow 0_1^+$ (560 keV) transition in ^{120}Te leads to small shifted components at short distances. Since these shifted components are the contaminations of the stopped component of the $4_2^+ \rightarrow 2_2^+$ (552 keV) transition in backward angles, a meaningful upper limit for the stopped component of the $4_2^+ \rightarrow 2_2^+$ (552 keV) transition can be estimated for the shortest relative distance of 2 μm. This allows to determine an upper limit of $\tau(4_2^+) < 10$ ps for the lifetime of the 4_2^+ state. Since also the $4_2^+ \rightarrow 4_1^+$ (497 keV) transition is contaminated by the $4_1 \rightarrow 2_1^+$ (497 keV) transition in ^{122}Xe, this upper limit is the only information on the lifetime of the 4_2^+ state.

With these upper limits of the lifetimes of the feeding states of the 2_2^+ state it is now possible to make some considerations regarding the lifetime of the 2_2^+ state. For example, if the lifetimes of the 3_1^+ state and the 4_2^+ state are assumed to be exactly equal to their respective lower limits and unobserved slow feeding is assumed not to be present, the lifetime value determined for the 2_2^+ state would be 9(2) ps. If the lifetimes of the 3_1^+ state and the 4_2^+ state are assumed to be exactly equal to their respective upper limits and unobserved slow feeding is assumed not to be present, the lifetime value determined for the 2_2^+ state would be 5(2) ps. If unobserved slow feeding could be ruled out, a meaningful lower limit could be determined. In general however, unobserved slow feeding with lifetimes in the order of single-digit picoseconds cannot be ruled out even if they are atypical in α-transfer experiments (compare Sec. 2.1.2). Therefore it is only possible to determine an upper limit of $\tau(2_2^+) < 13$ ps with a 2σ confidence. However, very short lifetime values around 1 ps seem unlikely.

The statistics of the $0_2^+ \rightarrow 2_1^+$ (352 keV) transition are not sufficient to reliably determine
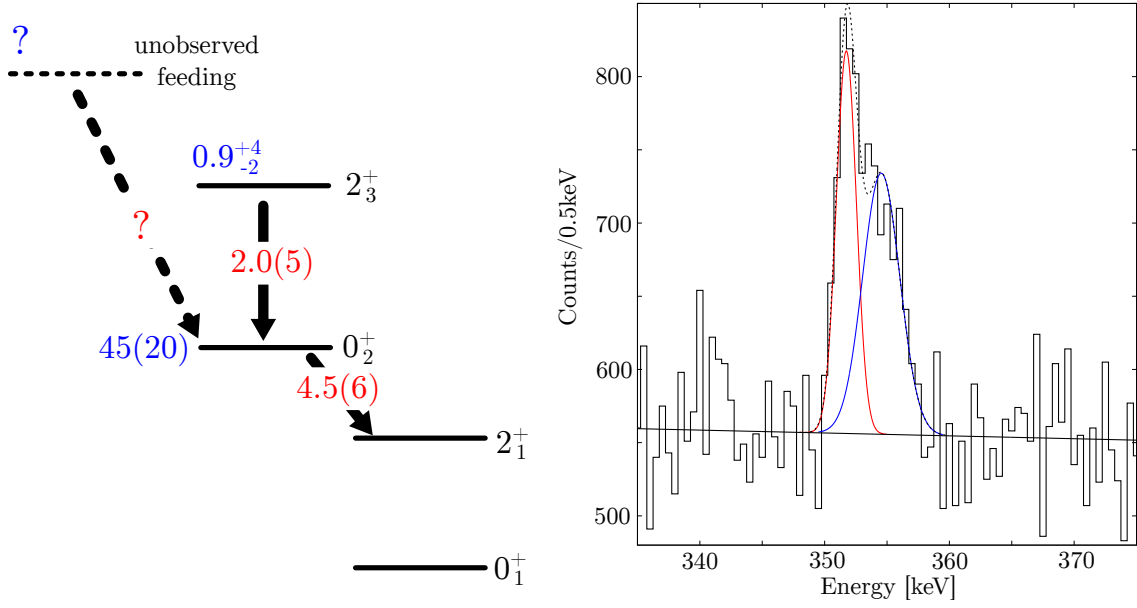
Figure 4.7: *Left*: Scheme of transitions populating and depopulating the 2_2^+ state in ^{118}Te observed in the ^{114}Sn(^{12}C,^{8}Be)^{118}Te α-transfer reaction. Intensities of the transitions (red) are given in percentages of the intensity of the $2_1^+ \rightarrow 0_1^+$ (606 keV) transition, information on lifetimes (blue) relevant to the lifetime analysis are given in picoseconds. The lifetime value of the 2_3^+ state is adopted from Ref. [31].
Right: Spectrum showing the $2_1^+ \rightarrow 0_1^+$ (352 keV) transition in ^{118}Te recorded with detectors at 30°. A gate condition is set on the solar cells. An unshifted and a shifted component are clearly visible. The statistics of all target-to-stopper distances are summed. The fit of the transition is shown as a dotted curve, the decomposition in shifted and unshifted component is shown in blue and red color, respectively.

a ratio of shifted and unshifted component for each distance. This is mainly caused by the background from Compton events that is especially large in this region. Summing all distances, it is possible to determine a ratio of shifted and unshifted component (see Fig. 4.7). This ratio can be used to determine a lifetime value for the 0_2^+ state as explained in Sec. 2.2. The determined lifetime value is $\tau(0_2^+) = 45(20)$ ps. The biggest contributions to the uncertainty arise from the determination of the ratio of unshifted component to the total intensity with a large background (compare Fig. 4.7) and the determination of the distance offset. In this analysis, the known fast feeding from the $2_3^+ \rightarrow 0_2^+$ (524 keV) transition has been accounted for using the lifetime value from Ref. [31] of $\tau(2_3^+) = 0.9^{+0.4}_{-0.2}$ ps. Given the nature of the α-transfer reaction (compare Sec. 2.1.2) and the relatively long lifetime of the 0_2^+ state, unobserved slow feeding is unlikely to have a significant effect. Consequently, the influence of unobserved slow feeding is considered negligible in this case.

4.2.6 Discussion

In Tab. 4.2, an overview of all determined lifetime values in ^{118}Te is given. The data are compared with literature values.

One motivation for the lifetime measurement in ^{118}Te was a reduction of the uncertainty of the lifetime value of the 2_1^+ state. At the start of this thesis project, the only known value of 8.8(14) ps [36] had a relatively large uncertainty. Very recently published values of 7.46(19) ps [74] and 8.2(5) ps [75] agree with the lifetime value of this work (7.2(6) ps) confirming that the lifetime appears to be slightly shorter than the previously measured 8.8(14) ps. The obtained lifetime value of the 4_1^+ state of 4.4(4) ps agrees very well with the previous value of $\tau(4_1^+) = 4.4(8)$ ps [36] and a very recent result of $\tau(4_1^+) = 4.25(23)$ ps [74]. The lifetime value determined for the 0_2^+ state of $\tau(0_2^+) = 45(20)$ ps agrees with the previous preliminary value of $t_{1/2}(0_2^+) = 55(45)$ ps [71] and significantly improves the uncertainty. The effective lifetime of $\tau_{eff}(2_2^+) = 10(3)$ ps obtained for the 2_2^+ is difficult to interpret. Previously, a lifetime of $1.2^{+0.4}_{-0.2}$ ps has been measured [31]. These two results can only be reconciled, if there is a very significant contribution of slow feeding to the 2_2^+ state in the present ^{114}Sn(^{12}C,^{8}Be)^{118}Te transfer reaction. This possibility cannot be excluded from the present data, but would be atypical as explained in the previous section. In this discussion a conservative upper limit of $\tau(2_2^+) < 13$ ps is therefore adopted. For all lifetimes of higher-lying states, only upper limits are determined in this work. Many of them have previously been measured using the DSA method [31].

Table 4.2: Lifetime values of excited states in ^{118}Te obtained in this work compared to previous measurements. Adopted lifetime values are given for the 2_1^+, 0_2^+, 2_2^+ and 4_1^+ states. The adopted lifetime values of the 2_1^+ and 4_1^+ states have been calculated using the weighted mean value. All lifetime values are given in picoseconds, all energies are given in keV. See text for details.

E_{level}	J_i^π	τ(this work)	τ [36]	τ [31]	τ [74]	τ [75]	τ_{adpt}
606	2_1^+	7.2(6)	8.8(14)		7.46(19)	8.2(5)	7.6(2)
957	0_2^+	45(20)					45(20)
1151	2_2^+	< 13		$1.2^{+0.4}_{-0.2}$			< 13
1206	4_1^+	4.4(4)	4.4(8)		4.25(23)		4.3(2)
1482	2_3^+	< 5		$0.9^{+0.4}_{-0.2}$			
1703	4_2^+	< 10		> 1			
1820	6_1^+		3.4(5)				
1863		< 10					
1891	3_1^+	< 10		> 2.5			
1944	3_1^-	< 15		0.95(20)			
1976	4_3^+	< 40		$1.2^{+0.3}_{-0.2}$			
2021		< 10		$0.35^{+0.35}_{-0.15}$			
2150	6_2^+	< 10		$1.0^{+0.4}_{-0.3}$			

With the lifetime values it is now possible to calculate absolute transition strengths. For the calculation of the $B(E2; 2_2^+ \to 2_1^+)$ value, it is necessary to know the $E2/M1$ mixing ratio δ of the $2_2^+ \to 2_1^+$ (545 keV) transition. This value has been measured two times. In Ref. [28] a $E2/M1$ mixing ratio of $\delta = 17_{-7}^{+27}$ is given, stemming from a measurement by Stone *et al.* [76]. Mihai *et al.* [31] determine two possible $E2/M1$ mixing ratios of $\delta = 11.0_{-0.5}^{+0.7}$ or $\delta = -0.35(2)$. Since the former result of Mihai *et al.* [31] agrees with the value given in Ref. [28], the result of $\delta = 11.0_{-0.5}^{+0.7}$ is adopted in this work. Unfortunately, details on the measurement by Stone *et al.* [76] have never been published and a final confirmation of the value of the $E2/M1$ mixing ratio through a measurement is therefore desirable.

The calculated $B(E2)$ strengths of transitions between the 4_1^+, 2_2^+, 0_2^+, 2_1^+ and 0_1^+ states are shown in Tab. 4.3, along with $B(E2)$ values calculated in the U(5) limit of the IBM-1 using the ratios given in Eq. (1.6) and normalized to the experimental $B(E2; 2_1^+ \to 0_1^+)$ value. The predicted transition strengths in the U(5) limit agree well with the measured $B(E2; 4_1 \to 2_1^+)$ and $B(E2; 0_2 \to 2_1^+)$ values, as well as with the experimental lower limit of the $B(E2; 2_2 \to 2_1^+)$ value. However, the lower limit determined for the $B(E2; 2_2 \to 2_1^+)$ value and the relatively large uncertainty of the $B(E2; 0_2 \to 2_1^+)$ value allow only limited conclusions. To achieve a better understanding, more precise lifetime values of the 2_2^+ and 0_2^+ states are needed. A more precise lifetime measurement of these states is, in principle, possible with the same setup and using the same reaction mechanism if the practical issues described in Sec. 4.2.1 can be avoided.

Table 4.3: $B(E2)$ values of transitions between the first four excited states in ^{118}Te. The used lifetime values of 2_1^+ and 4_1^+ states are weighted mean values of all experiments. See text for details. Energy levels and branching ratios are taken from Ref. [28].

E_{level} [keV]	J_i^π	E_γ [keV]	E_f [keV]	J_f^π	b	τ [ps]	δ	$B(E2)$ [W.u.]	U(5)
606	2_1^+	606	0	0_1^+	100	7.6(2)		38(1)	38
957	0_2^+	352	606	2_1^+	100	45(20)		90_{-30}^{+70}	68
1151	2_2^+	545	606	2_1^+	100(2)	< 13	$11.0_{-0.5}^{+0.7}$	> 28	68
		1151	0	0_1^+	27(2)			> 0.2	0.0
1206	4_1^+	601	606	2_1^+	100	4.3(2)		70(3)	68

The measurement of the lifetime of the 0_2^+ state also allows the determination of the $\rho^2(E0; 0_2^+ \to 0_1^+)$ value. The $0_2^+ \to 0_1^+$ E0 transition has been observed by Walker *et al.* [47] who determined a value of $X(E0/E2) = 0.009(2)$ for the E0 and E2 decays of the 0_2^+ state to the 0_1^+ and 2_1^+ states. With Eq. (2.5) a value of $\rho^2(E0; 0_2^+ \to 0_1^+) \cdot 10^3 = 24_{-8}^{+18}$ is calculated. The order of magnitude of the absolute E0 transition strength is comparable to E0 transition strengths of $0_2^+ \to 0_1^+$ transitions in the Cd isotopes, where the 0_2^+ is considered to be an intruder state [20].

The determined absolute transition strengths can be used to get closer to an answer regarding the nature of the 0_2^+ state in ^{118}Te. The 0_2^+ state is a potential member of the

two-phonon triplet in the U(5) limit of the IBM-1 model and on the other hand also a candidate for the band head of an intruding structure. The measured $B(E2; 0_2^+ \rightarrow 2_1^+)$ value is still in agreement with the prediction of the U(5) limit, but the enhanced E0 transition strength of the $0_2^+ \rightarrow 0_1^+$ transition does not fit in the picture. The strength of the E0 transition can instead be interpreted as a sign of shape coexistence. For a more complete picture of shape coexistence in ^{118}Te it is necessary to identify the related collective structures on top of the band head. Previous studies have identified two different candidate states for the first excited state of this collective structure. An earlier study notes that the energy spacing between the 2_2^+ state and the 0_2^+ suggests this state as a candidate [14]. The necessary in-band transition has not been observed so far. A very recent review notices that the large $B(E2; 2_3^+ \rightarrow 0_2^+)$ value can be interpreted as a hint that the 2_3^+ state is a member of the intruding structure [5] even though the energy spacing is relatively large. The enhanced $\rho^2(E0; 0_2^+ \rightarrow 0_1^+)$ value can also hint at mixing between the intruder structure and the normal configuration. This mixing of normal and intruder configuration is also suspected by other studies (Ref. [14, 35]). Furthermore, if the 0_2^+ state is indeed an intruding state, a candidate for the 0^+ state belonging to the two-phonon triplet of the normal configuration needs to be found. In Ref. [47] a 0^+ state is identified at 1517 keV that is not identified in any other study. Other excited 0^+ states are not known.

The present data show, that an unambiguous identification of the expected shape coexistence in ^{118}Te is not easy. The excitation energies and absolute transition strengths calculated from measured lifetimes are compatible with shape coexistence but agree as well with the predictions of the U(5) limit of the IBM-1. Only the enhanced $\rho^2(E0; 0_2^+ \rightarrow 0_1^+)$ values hint at shape coexistence and mixing of intruder and normal configuration. For a more complete picture, experimental data is missing or inconclusive.

4.3 Experiment on ^{120}Te

The only stable nucleus that is investigated in this work is ^{120}Te with a neutron number of $N = 68$ which has two neutrons more than ^{118}Te at mid shell $N = 66$ and thus the same number of valence nucleons as ^{116}Te if no distinction is made between particle-like and hole-like valence nucleons. Since the natural abundance of ^{120}Te is only 0.09 % [77], there is less experimental data on this isotope than on more abundant Te isotopes. The most detailed spectroscopic analysis of ^{120}Te was performed by Vanhoy *et al.* [32] who are able to describe experimental excitation energies and relative $B(E2)$ values within the U(5) limit of the IBM-1. Some $B(E2)$ values have been determined through Coulomb excitation [37] and lifetime measurements [38, 78]. The absolute transition strength of the $0_2^+ \rightarrow 2_1^+$ transition and the $\rho^2(E0; 0_2^+ \rightarrow 0_1^+)$ value were not determined in these studies. However, these observables are key signatures for the nuclear structure (compare Sec. 1.1 and 1.2). In the experiment described here, information on the lifetime of the 0_2^+ are obtained using an RDDS measurement in combination with an ^{116}Sn(^{12}C,^{8}Be)^{120}Te α-transfer reaction. The experimental results allow first conclusions on the $B(E2; 0_2^+ \rightarrow 2_1^+)$ and $\rho^2(E0; 0_2^+ \rightarrow 0_1^+)$ values.

4.3.1 Experiment

The ^{116}Sn(^{12}C,^{8}Be)^{120}Te α-transfer experiment was performed at the FN tandem accelerator in Cologne using the Cologne Plunger spectrometer. The beam energy was 44 MeV. The target foil was mounted together with a stopper foil inside the Cologne coincidence plunger device to measure lifetimes with the RDDS method. The target consisted of highly enriched 0.5 mg/cm^2 ^{116}Sn evaporated on a 1.5 mg/cm^2 fronting where the latter was facing the beam. The stopper foil was a 7.1 mg/cm^2 thick Ta foil. Data were taken for seven different target-to-stopper distances between 250 µm and electrical contact. One measurement without a stopper foil was performed. For the detection of γ rays, the Cologne Plunger spectrometer was equipped with eleven HPGe detectors mounted in two rings at 45° and 142° with respect to the beam axis consisting of six and five detectors, respectively. In addition, the Cologne coincidence plunger device was equipped with a solar-cell array at backward angles for the detection of α particles stemming from the decay of ^{8}Be. The four solar cells of the array were covered with a 40 µm thick aluminum foil. The aluminum foil prevented heavier charged particles from entering into the particle detectors.

4.3.2 Data analysis - observed transitions

The data from the experiment are sorted into particle-γ matrices. The absorption of heavier beam-like fragments in the aluminum foil results in particle spectra containing mainly events stemming from the detection of α particles in the solar cells. A gating
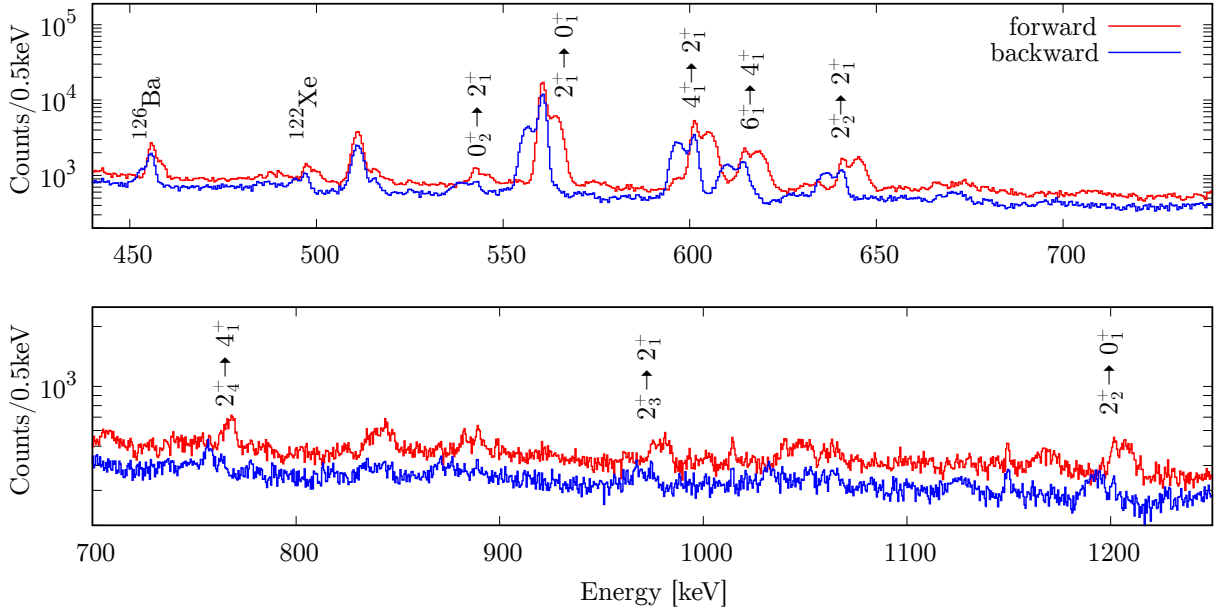
Figure 4.8: Spectrum showing γ-ray transitions observed in the ^{116}Sn(^{12}C,^{8}Be)^{120}Te α-transfer reaction. The lower panel is the continuation of the upper panel for higher energies. Due to the large velocity distribution and the consequent broadening of peaks, it is difficult to identify transitions both with lower intensities and at higher energies, where HPGe detector efficiency decreases.

condition accepting any γ-ray event coincident to a hit in a solar cell is thus set to obtain γ-ray spectra of ^{120}Te. The resulting spectra shown in Fig. 4.8 are relatively clean, only small contaminations from fusion-evaporation reactions can be found. However, during the experiment, partial stopping of the nuclei of interest in the target foil was observed (compare Sec. 2.1.3 and Fig. 2.2) which makes further analysis of the data more difficult. In an RDDS experiment, the intensity of an observed γ-ray transition is usually distributed over two distinct components: an unshifted and a shifted component. The width of the unshifted component corresponds roughly to the detector resolution. The width of the shifted component is increased by the velocity distribution, since different velocities will lead to different Doppler shifts. The shifted component can often still be modelled by a Gaussian if the velocity distribution is centered around a mean velocity. However, in the case of partial stopping in the target, the velocity distribution ranges from zero to a maximal velocity and is not centered around a mean velocity. The shifted component will instead be broad and smeared out.

An overview over the identified transitions is given in Tab. 4.4. In general, the population scheme observed in this experiment resembles those observed in the α-transfer experiments on ^{116,118}Te: The populated states were rather low-lying and low-spin states, including the 0_2^+ state. However, considerably fewer transitions can be identified in this α-transfer experiment than in the transfer experiments on ^{116,118}Te, probably because — as mentioned

above — the shifted components observed in this experiment are rather smeared out making an identification of low-intensity transitions depopulating short-lived states difficult (see Figs. 4.8 and 4.9).

Table 4.4: Observed intensities in the ^{116}Sn(^{12}C,^{8}Be)^{120}Te α-transfer reaction. Intensities are corrected for the spectrometer efficiency and normalized to the intensity of the $2_1^+ \rightarrow 0_1^+$ (560 keV) ground-state transition. The quantity $\sum R(t)$ gives the ratio of the stopped component to the total intensity summed over all target-to-stopper distances. See text for details.

$E_\gamma [keV]$	J_i^π	E_i [keV]	J_f^π	E_f [keV]	I	$\sum R(t)$
542.8	0_2^+	1103.1	2_1^+	560.4	4.0(3)	0.42(14)
560.4	2_1^+	560.4	0_1^+	0.0	100(1)	0.61(3)
601.1	4_1^+	1161.6	2_1^+	560.4	39.7(5)	0.41(2)
614.6	6_1^+	1776.2	4_1^+	1161.6	18(1)	0.34(2)
640.9	2_2^+	1201.3	2_1^+	560.4	11.1(3)	0.35(1)
762.8	2_4^+	1924.4	4_1^+	1161.6	1.9(3)	0.2(1)
974.6	2_3^+	1535.1	2_1^+	560.4	1.5(3)	0.28(7)
1040.0	6_2^+	2201.5	4_1^+	1161.6	1.1(3)	-
1201.2	2_2^+	1201.2	0_1^+	0.0	1.7(3)	0.27(5)
1523.0	3_1^-	2083.1	2_1^+	560.4	<4	-
1534.9	2_3^+	1534.9	0_1^+	0.0	<4	-

4.3.3 Data analysis - lifetimes

The partial stopping in the target foil (compare Sec. 2.1.3 and Fig. 2.2) has also severe consequences for the lifetime analysis. Since the nuclei are partially stopped already in the target foil, every observed transition will have a stopped component that is independent from the target-to-stopper distance. This adds an artificial offset to the observed decay curve $R(t)$ (compare Eq. (2.7)). On the other hand, the broad velocity distribution implies that some nuclei will consistently be relatively slow. These nuclei then have longer flight times, leading to flight components at small distances. This effect further distorts the decay curve. Finally, Eq. 2.11 requires a mean velocity and with the partial stopping of the nuclei of interest in the target foil, there is in general no well defined mean velocity. This also means that the flight time for a given target-to-stopper distance is not well defined. In consequence, any decay curves obtained in this experiment are of little use for a lifetime determination using conventional analysis approaches.

The ratio of shifted and unshifted components — and thus also the decay curves — of a γ-ray transition can however still be determined by integrating the total intensity of the transition and then fitting the intensity of the stopped component of the transition with a Gaussian (see Fig. 4.9). This is possible since the width and position of the stopped component are known from an energy and width calibration using a ^{226}Ra source and
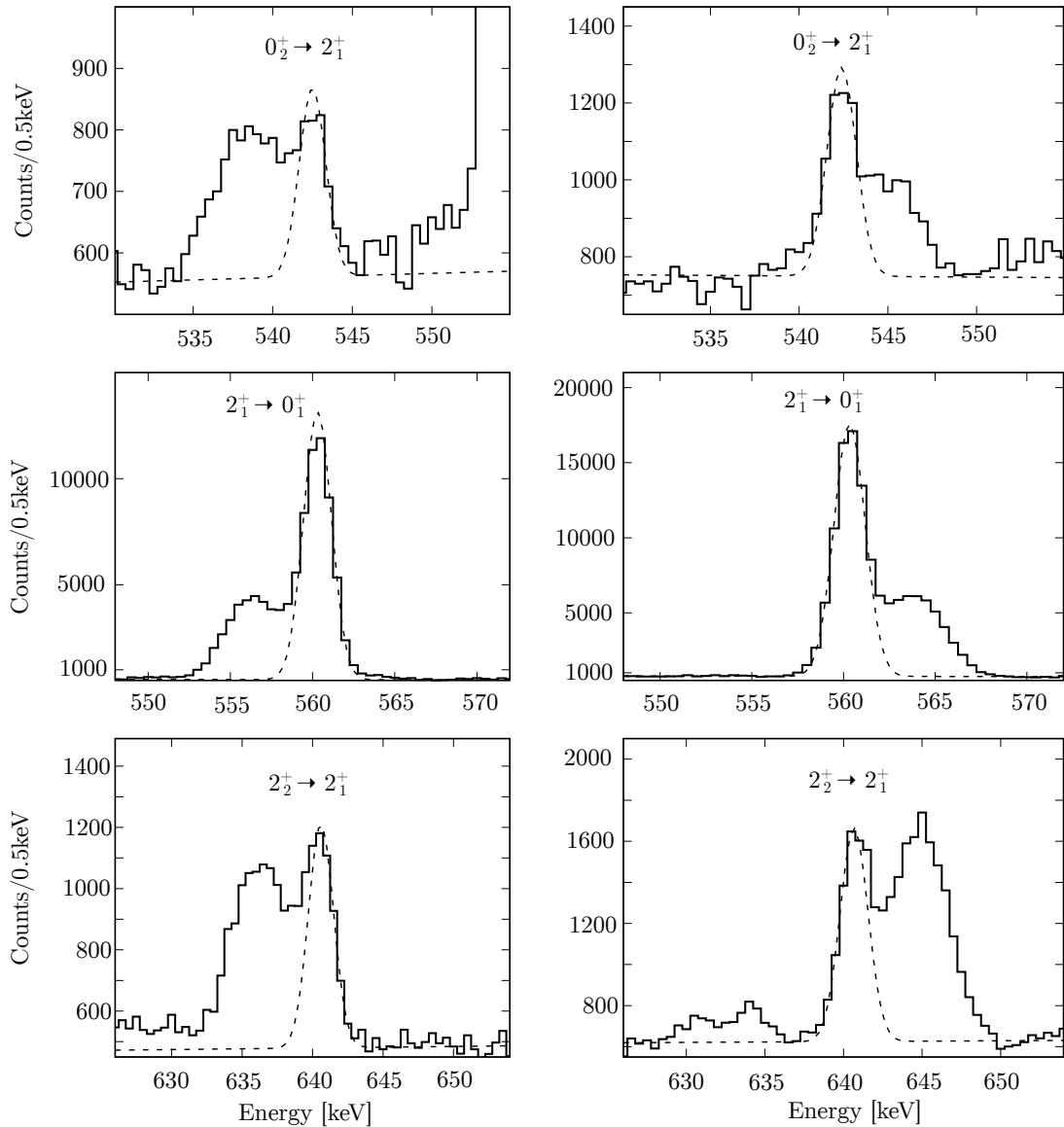
Figure 4.9: Observed γ-ray transitions in ^{120}Te using the ^{116}Sn(^{12}C,^{8}Be)^{120}Te α-transfer reaction. Spectra on the left are recorded with the backward ring at 142°, spectra on the right are recorded using the forward ring at 45°. Data for all target-to-stopper distances are summed. A shifted component is visible for all transitions. The fit of the stopped component is shown in dotted lines. A fit of the shifted component is not performed since it cannot be assumed to have a Gaussian shape. Instead, the intensity is calculated by subtracting the stopped intensity from the integrated total intensity.

from β-decay data that were observed during the experiment. Here, $R(t)$ values were determined for spectra where all target-to-stopper distances were summed. This increases the statistics for the determination of the intensities of shifted and unshifted component. The ratio of unshifted to total intensity for these spectra will be denoted with $\sum R(t)$. Spectra showing stopped and flight components of different γ-ray transitions are shown in

Fig. 4.9. The determined $\sum R(t)$ values are also listed in Tab. 4.4.

Now it is important to realize that the $\sum R(t)$ value of a transition depopulating an excited state depends on the effective lifetime (compare Sec. 2.2.1) of this state. Shorter effective lifetimes will be reflected in smaller $\sum R(t)$ values and longer effective lifetimes in larger $\sum R(t)$ values. An exact quantification of these effective lifetimes from the $\sum R(t)$ values is not possible, but it is possible to determine which effective lifetime must be longer than another effective lifetime by comparing the measured $\sum R(t)$ values. From Fig. 4.9 and Tab. 4.4 it is evident, that the $\sum R(t)$ value of the $0_2^+ \rightarrow 2_1^+$ (543 keV) transition is smaller than the $\sum R(t)$ value of the $2_1^+ \rightarrow 0_1^+$ (560 keV)transition. The effective lifetime of the 0_2^+ is thus shorter than the effective lifetime of the 2_1^+ state. Since the effective lifetime of an excited state observed in an experiment is always longer than the "real" lifetime of the excited state, the effective lifetime of the 2_1^+ state constitutes an upper limit for the lifetime of the 0_2^+ state.

An upper limit of the lifetime of the 0_2^+ state can now be determined by reconstructing the effective lifetime of the 2_1^+ state observed in this experiment. For this reconstruction, the feeding intensities of transitions feeding the 2_1^+ state observed in this experiment, the lifetime values of all feeders of the 2_1^+ state and the lifetime value of the 2_1^+ state are needed. The feeding intensities of all observed feeders are already presented in Tab. 4.4. The excited states whose depopulating transitions contribute the most to the feeding of the 2_1^+ state are the 4_1^+, 2_2^+ and 6_1^+ states. Their respective lifetimes have been measured in different experiments [37, 38, 78][1]. The literature values used for the reconstruction are given in Tab. 4.5. The values used for the reconstruction are the upper limits of the adopted experimental lifetime values. The lifetimes of the 2_3^+, 2_4^+ and 6_1^+ state that contribute less to the feeding of the 2_1^+ state are not known but seem to be short given their $\sum R(t)$ values (see Tab. 4.4). Contributions from unobserved, long-lived feeding are unlikely due to the nature of the direct transfer reaction and are here neglected.

With these inputs it is now possible to reconstruct a decay curve of the $2_1^+ \rightarrow 0_1^+$ (560 keV) transition using the Bateman equations. It is found that a decay curve from an effective lifetime of $\tau_{eff} = 25$ ps produces a decay curve that is larger than the decay curve simulated for the 2_1^+ state. This means that 25 ps is an upper limit of the effective lifetime of the 2_1^+ state. Consequently, an upper limit of $\tau(0_2^+) < 25$ ps can be determined for the lifeitme of the 0_2^+ state.

---

[1]The lifetimes from Ref. [37] have been calculated from the given $B(E2)$ values. In the case of the lifetime of the 2_2^+ state, Ref [37] gives a $B(E2; 2_2^+ \rightarrow 2_1^+)$ and a $B(E2; 2_2^+ \rightarrow 0_1^+)$ value. To calculate the lifetime of the 2_2^+ state, additionally the $E2/M1$ multipole mixing ratio of the $2_2^+ \rightarrow 2_1^+$ (641 keV) transition or the branching need to be known. In the literature, very different values can be found for both quantities. The Nuclear Data Sheets [29] give $\delta = -0.92(9)$ and a branching of 27(3)% of the decay branch to the ground state relative to the decay branch to the 2_1^+ state. In Ref. [32], two possible solutions are given for the multipole mixing ratio: $\delta = 0.27(15)$ or $\delta = 1.19(19)$ and also two branching ratios are reported: 12% and 48%. The reconstructed lifetime value varies with the choice of these experimental values. The largest lifetime value is obtained with a mixing ratio of 1.19(19) or a branching ratio of 12% and is 2.6(3) ps. Since here an upper limit of the effective lifetime is of interest, an upper limit of 3 ps is adopted.

Table 4.5: Literature lifetimes used to calculate the effective lifetimes observed in the ^{116}Sn(^{12}C,^{8}Be)^{120}Te α-transfer reaction. Since only an upper limit can be calculated, the upper limits of the lifetimes were determined, and with the upper limits the effective lifetimes were calculated. All values are given in ps.

	Saxena *et al.* [37]	von Spee [38]	Werner *et al.* [78]	τ_{adp}	τ_{max}
2^+_1	11.0 (1)	10.1(3)	10.4(2)	10.8(1)	11.0
4^+_1	4.8(1)	4.8(3)	-	4.8(1)	5.0
2^+_2	<3	-	-	-	3
6^+_1	3(1)	4.6(2)	-	4.5(2)	4.9

4.3.4 Discussion

Although only an upper limit of the lifetime of the 0^+_2 state can be determined, valuable conclusions can still be drawn about the nuclear structure of ^{120}Te. Using this upper limit, a lower limit for the $B(E2; 0^+_2 \rightarrow 2^+_1)$ value of 19 W.u. can be calculated. In Fig. 4.10 $B(E2)$ values between low lying states in ^{120}Te are shown. A comparison of the $B(E2)$ values shows, that the $B_{0/2}$ ratio is much larger than zero and $B_{0/2} > 0.5$. This is in agreement with the predictions of the U(5) limit in the IBM-1 model as described in Sec. 1.1. Both the S(U3) and the O(6) limits of the IBM-1 would predict $B_{0/2} = 0$ and thus do not provide an explanation for the observed decay of the 0^+_2 state.
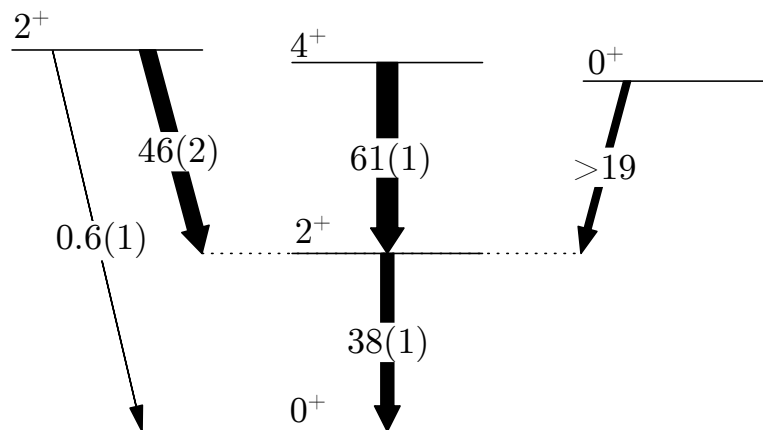

Figure 4.10: $B(E2)$ values in ^{120}Te for the lowest-lying states. The lower limit for the $B(E2; 0^+_2 \rightarrow 2^+_1)$ value is obtained in this work. The other values are mean values from [37,38,78]. All values are given in W.u.

Additionally, a lower limit of $\rho^2(E0, 0^+_2 \rightarrow 0^+_1) \cdot 10^3 > 7$ is determined using $X(E0/E2) = 0.016(4)$ given in Ref. [47]. Enhanced $\rho^2(E0)$ values are often an indicator of shape coexistence and mixing of shapes (compare Sec. 1.2). Typical $\rho^2(E0; 0^+_2 \rightarrow 0^+_1) \cdot 10^3$ values in mid-shell Cd isotopes that are associated with shape coexistence are $\rho^2(E0; 0^+_2 \rightarrow 0^+_1) \cdot 10^3 = 37^{+9}_{-11}$ in ^{112}Cd and $\rho^2(E0; 0^+_2 \rightarrow 0^+_1) \cdot 10^3 = 19(2)$ in ^{114}Cd. Thus the lower

limit obtained here for ^{120}Te would seem to make it likely that the value can indeed be regarded as an indicator of shape coexistence. The suggested shape coexistence could also provide an explanation for the low lying 0_2^+ state and its relatively strong decay to the 2_1^+ state.

It is evident, that the data collected in this work cannot give a clear answer to the question of the structure of ^{120}Te. The quality of the data which is significantly worsened by the partial stopping of the recoiling nuclei in the target foil is not sufficiently good for this scope. The data collected here show that the lifetime of the 0_2^+ is measurable — provided a good target foil — with the same setup and the same reaction mechanism. A repetition of the measurement is therefore highly desirable.

Chapter 5

Discussion of the results

In the previous chapter, the experimental results of this work are presented. The core subject of the performed experiments are experimental values for the lifetimes of excited states in ^{116,118,120}Te. To obtain the most complete picture of the nuclear structure of mid-shell Te isotopes, it is appropriate not only to consider the newly obtained experimental results on lifetimes presented here but also to incorporate other measurements. This includes the work of Refs. [31, 36–38, 78], as well as very recent results from Refs. [74, 75]. In Tab. 5.1, all lifetime values for low-lying states in ^{116,118,120}Te are listed and adopted lifetimes are presented. In most cases all experimental results agree reasonably well. Then the adopted value is calculated using the weighted mean. The only exception is the lifetime value of the 2_2^+ in ^{118}Te where the results obtained by Mihai *et al.* [31] and the data presented in this work do not align well with each other. In this case, the result from this work is adopted, which is a conservative upper limit of $\tau(2_2^+) < 13$ ps. A consistent reconstruction of the lifetime of the 2_2^+ state in ^{120}Te from $B(E2)$ values given in Ref. [37] was not possible.

Table 5.1: Adopted lifetime values of excited states in ^{116,118,120}Te and experimental results used for the calculation of the adopted lifetimes. Note that the experimental result of $t_{1/2}(0_2^+) = 55(45)$ ps in ^{118}Te from Ref. [71] is not considered here since the authors themselves describe their result as preliminary.

J^π	Nucleus	τ [ps]		
		this work	other results	adopted value
2_1^+	^{116}Te	5(2)	5.1(3) [75]	5.1(3)
2_1^+	^{118}Te	7.2(6)	8.8(14) [36], 8.2(5) [75], 7.46(19) [74]	7.6(2)
2_1^+	^{120}Te	-	11.0(1) [37], 10.1(3) [38], 10.4(2) [78]	10.8(1)
0_2^+	^{116}Te	69(9)	-	69(9)
0_2^+	^{118}Te	45(20)	-	45(20)
0_2^+	^{120}Te	<25	-	<25
2_2^+	^{116}Te	12.3(15)	-	12.3(15)
2_2^+	^{118}Te	<13	$1.1^{+0.4}_{-0.2}$ [31]	<13
2_2^+	^{120}Te	-	-	-
4_1^+	^{116}Te	$1 < \tau < 9$	-	$1 < \tau < 9$
4_1^+	^{118}Te	4.4(4)	4.4(8) [36], 4.25(23) [74]	5.1(3)
4_1^+	^{120}Te	-	4.8(1) [37], 4.8(3) [38]	4.8(1)

With the adopted lifetime values it is possible to determine $B(E2)$ and $\rho^2(E0)$ values in ^{116,118,120}Te. An overview of results obtained with the help of these adopted lifetime values is given in Fig. 5.1. Details on the determination of the $B(E2)$ and $\rho^2(E0)$ values are given in Secs. 4.1, 4.2 and 4.3.
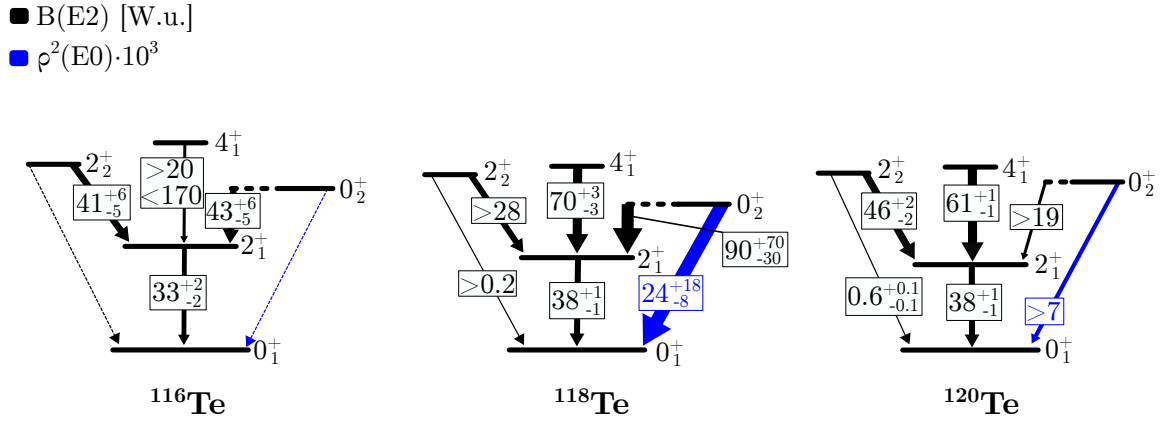
- ■ B(E2) [W.u.]
- ■ $\rho^2(E0){\cdot}10^3$

Figure 5.1: $B(E2)$ and $\rho^2(E0)$ values for transitions in ^{116,118,120}Te calculated using the adopted lifetime values given in Tab. 5.1. Only transitions between the 0_1^+, 2_1^+, 0_2^+, 2_2^+ and 4_1^+ states are shown. Details on the determination of the $B(E2)$ and $\rho^2(E0)$ values are given in Secs. 4.1, 4.2 and 4.3. Transitions shown in black (blue) are $E2$ ($E0$) transitions. Dotted transitions have not been observed so far.

In the following sections, the conclusions that can be drawn from the results of the performed experiments are summarized. The nuclear structure of the mid-shell Te isotopes is discussed in this context.

5.1 Conclusions

5.1.1 Lifetime measurements using α-transfer reactions in combination with Doppler-shift methods

The main focus of this thesis was the measurement of lifetimes of excited states with the RDDS method in mid-shell tellurium isotopes. Special interest was focused on the lifetimes of excited 0^+ states, as those states play a crucial role in the identification of shape coexistence [18]. However, lifetimes of excited 0^+ states are difficult to measure: it is difficult to populate these states in general, and, even more, with sufficient recoil velocity needed for a lifetime measurement using Doppler-shift techniques. This work shows, that the (^{12}C,^{8}Be) α-transfer reaction is an excellent tool to populate lower-lying low-spin excited states and also transfer sufficient momentum to the nucleus of interest, that the resulting recoil velocity is sufficient for an RDDS measurement: for all three studied nuclei ^{116,118,120}Te information on the lifetime of the 0_2^+ state could be deduced from the respective experiments. Furthermore, all observed γ-ray transitions in all performed

α-transfer experiments showed shifted components, underlining the advantage of the direct population mechanism of transfer reactions that avoids possible higher-lying isomers. Unfortunately, not all experiments conducted within the scope of this thesis yielded optimal results, and repeating the α-transfer experiments on ^{118}Te and ^{120}Te could significantly enhance the outcomes of this study. Furthermore, many of the populated states were shown to have lifetimes shorter than what could be measured with the employed RDDS setup. The lifetimes of at least some of these states can be measured instead using the Doppler-shift attenuation method (DSAM) with the same α-transfer reactions and setup, by replacing the RDDS target and stopper with a DSAM target.
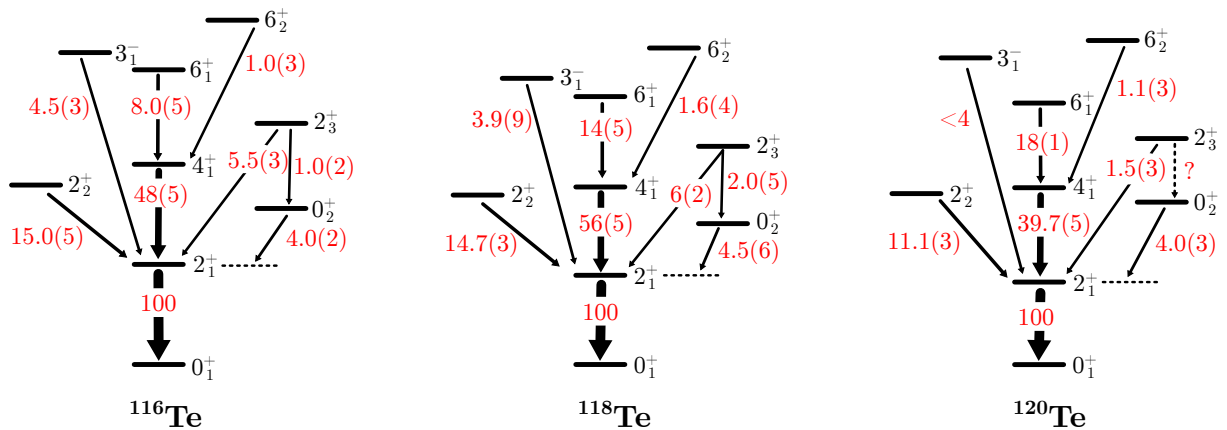

Figure 5.2: Observed intensities of selected γ-ray transitions in mid-shell Te isotopes populated in $(^{12}C,^{8}Be)$ α-transfer reactions on tin. The intensities are normalized on the intensity of the $2_1^+ \rightarrow 0_1^+$ transition of each nucleus. Note that in some cases not all depopulating transitions of observed excited states are shown. Data on all observed transitions can be found in Secs. 4.1,4.2 and 4.3.

The direct population mechanism also allows for another observation: In transfer reactions the cross section for the population of different excited states depends on the structure of these states [79]. Therefore, measuring these cross sections can provide additional understanding of the structure of the nucleus. Since the performed transfer experiments were optimized for lifetime measurements, exact information on relative or absolute cross sections cannot be obtained. Information of this kind is often extracted from precise measurements of the scattering angle and kinetic energy of the beam-like fragment. In the case of the performed α-transfer experiments, the information on the exact energy and scattering angle of the beam-like particles is lost due to the large opening angle of the solar cells, the rather thick target layer and the straggling in the fronting material and aluminum foil shielding the particle detector.

Determining cross sections of excited states through γ-ray information is prone to errors, as feeding contributions below the observation limit cannot be identified, though they are likely present. Fortunately, the energy systematics of many low-lying states in mid-shell Te isotopes evolve rather smoothly along the isotopic chain, and the branching ratios of

transitions connecting these states are similar. Therefore, in Fig. 5.2 the intensities of the observed γ-ray transitions following the α-transfer reactions are directly compared. It is apparent, that the population patterns are similar. In the yrast band, states are populated up to the 6_1^+ state, but the 8^+ state is not observed. In all three cases also the 6_2^+ state is populated; the intensities of the $0_2^+ \rightarrow 2_1^+$ states are also similar. This might hint at the fact, that the direct population patterns and hence the cross sections of single states for these three nuclei in the α-transfer reaction are also similar. Together with the similar level energies of excited states and similar absolute transition strengths between excited states, this might provide another indication, that nuclear structure evolves smoothly along the isotopic chain in the mid-shell tellurium region.

5.1.2 Reinvestigation of γ-ray spectroscopy following β decay

Historically, most nuclei that are populated in β decay have been thus studied using γ-ray spectroscopy following β decay. These types of experiments are relatively easy to perform and allow the study of many excited states, that are not populated in other mechanisms such as fusion-evaporation reactions. For example, if the ground-state spin of the mother nucleus is sufficiently low, typically also low-spin off-yrast states are populated. Also studies on ^{116,118,120}Te following the β decay of ^{116,118,120}I have been performed in the past. In this study, the population of excited states in ^{116}Te after the β decay of ^{116}I has been reinvestigated. Significantly more information was extracted than in previous measurements: In the present study, over 30 γ-ray transitions were identified in ^{116}Te, while in previous experiments only 13 γ-ray transition are reported by Zimmerman [46]. The main reason for this is that the last measurement by Zimmerman [46] was made 30 years ago: the HPGe detectors available for that experiment were fewer and less efficient than those used in this work. The additional information obtained in this study of the population after β decay significantly helped to improve the understanding of the nuclear structure of ^{116}Te. A similar study has been conducted already by Vanhoy *et al.* [32] for ^{120}Te and should encourage studies of excited states in ^{114}Te and ^{118}Te after the β decay of ^{114,118}I that have not been studied as thoroughly.

5.1.3 Systematics of energy levels

The parabolic dependency of the excitation energy of the 0_2^+ state on the neutron number in Te isotopes has been the first indicator, that these states might be intruder states [35]. The spins of the 0_2^+ and 2_3^+ states in ^{116}Te, which were previously uncertain, were firmly validated in this work. This extends the parabolic shape of the energy systematics of both the 0_2^+ and 2_3^+ state in Te isotopes towards lower neutron numbers, suggesting that these states are good candidates for an intruding structure (compare Fig. 11 of the publication shown in Sec. 4.1). A similar measurement for ^{112,114}Te would be able to extend this
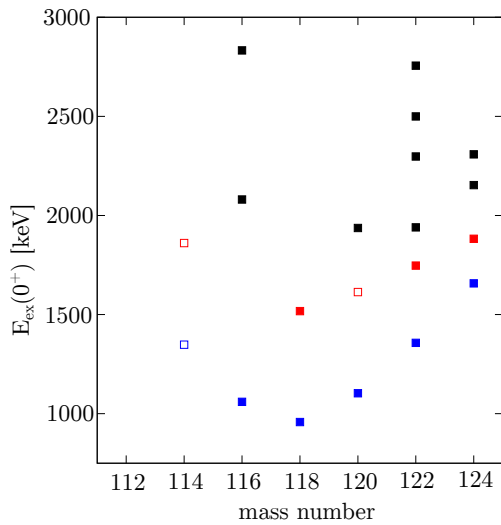
picture even further.

Figure 5.3: Experimental data on excited 0^+ states in Te isotopes. Empty squares are used for tentative or disputed assignments. Blue (red) color marks the candidate 0_2^+ (0_3^+) intruder states. Data is taken from Refs. [26–30, 32, 70, 80, 81].

It must be mentioned at this point, that no experiment performed in this work, and especially not the study of ^{116}Te following the β decay of ^{116}I was able to identify or confirm a 0_3^+ level lying in the region with excitation energies between around 1.5 and 1.8 MeV. Such states are reported in ^{118,120}Te by Refs. [28, 29] and tentatively reported in ^{114}Te by Ref. [26] as shown in Fig. 5.3. These states were in all three cases observed in β-decay experiments. In ^{114}Te, the level at 1860 keV has been observed only by Zimmerman [46] who tentatively assigns 0^+. In ^{118}Te, the level at 1517 keV is observed only by Walker *et al.* [47]. Other measurements using different reaction mechanisms did not observe the level. In the same study, Walker *et al.* [47] observe a 0^+ state at 1614 keV in ^{120}Te that is populated in β decay. In another experiment

also studying the β decay of ^{120}I, Vanhoy *et al.* questioned the existence of this level [32]. As these excited 0^+ states play an important role in the identification of shape coexistence, a clarification of these experimental data is highly desirable.

5.1.4 Systematics of absolute transition strengths

A look at the systematics of absolute transition strengths can improve the understanding of the evolution of nuclear structure in the Te isotopes. With the newly measured lifetimes, these systematics can be extended to lower neutron numbers. In Fig. 5.4, the $B(E2; 2_1^+ \rightarrow 0_1^+)$ values along the Te isotopic chain are shown. With increasing valence neutron number, the $B(E2; 2_1^+ \rightarrow 0_1^+)$ values are expected to rise and exhibit a maximum at neutron mid-shell $N = 66$ — in this case ^{118}Te. In the neighboring tin isotopes some experimental data suggest a small decrease of the $B(E2; 2_1^+ \rightarrow 0_1^+)$ values around mid-shell that is supported by calculations [83]. Such behavior was also hypothesized for the tellurium isotopes (compare Ref. [84]). The present data for the Te isotopes show, that the maximum is slightly shifted with respect to mid-shell, but do not support a dip similar to the one observed in the tin isotopes. Instead, the $B(E2; 2_1^+ \rightarrow 0_1^+)$ values in the Te isotopes are very similar to the values measured in the Cd isotopes, if the values are corrected for the difference in proton and mass number supporting the valence proton symmetry [82].
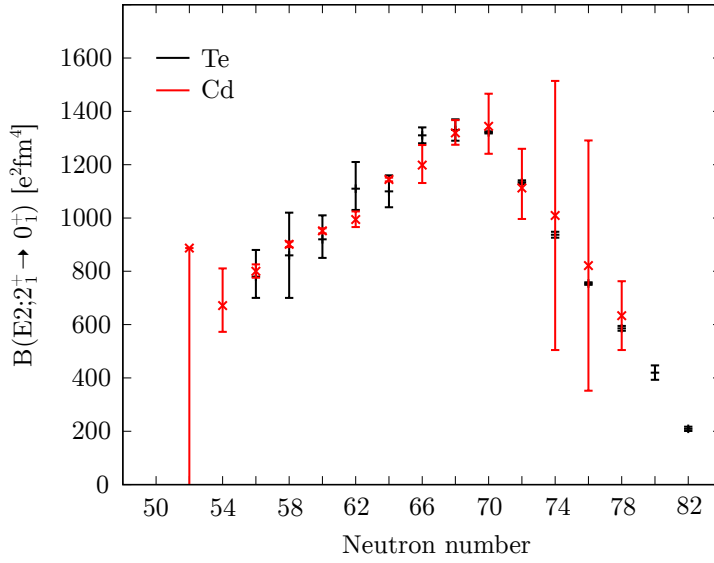
Figure 5.4: Comparison of $B(E2; 2_1^+ \rightarrow 0_1^+)$ values in Te and Cd isotopes. Note that the $B(E2; 2_1^+ \rightarrow 0_1^+)$ values of Cd isotopes are multiplied by $52^2/48^2 \cdot A_{Te}/A_{Cd}$ to account for the difference in proton and mass number according to Ref. [82].

5.1.5 Comparison with the U(5) limit of the IBM-1

An intuitive explanation for the low-energy part of the level scheme in mid-shell Te isotopes is a description with an anharmonic vibrator or a description in the U(5) limit of the IBM-1. The level energies of excited states of ^{118,120}Te have indeed already been described in the U(5) limit by Kern *et al.* [12], with relatively good agreement, except for the 3_1^+ state. The level energies of excited states in ^{116}Te have also been described within the U(5) limit in Sec. 4.1, with good agreement. It is therefore of great interest to compare also the newly obtained absolute transition strengths with predictions of the U(5) limit. If other phenomena like shape coexistence play a role, a deviation of the experimental values from the U(5) limit is likely. In Sec. 1.1.1 it is mentioned, that the $B_{4/2}$, $B_{2/2}$ and $B_{0/2}$ ratios in the U(5) limit are all given by $2\frac{N-1}{N}$. Since the number of valence nucleon pairs N is 8 for ^{116,120}Te and 9 for ^{118}Te, the ratios are given as 1.75 or 1.78 respectively. Notably, both other limits of the IBM-1 predict the $B_{0/2}$ to be equal to zero. In Tab. 5.2 all measured $B(E2)$ values between low-lying states in ^{116,118,120}Te and the predictions of the U(5) limit are shown. The large $B_{0/2}$ ratios, the small $B(E2; 2_2^+ \rightarrow 0_1^+)$ values and the more precisely known $B_{4/2}$ ratios agree relatively well with the predictions of the U(5) limit — especially considering that the model is only normalized to the experimental $B(E2; 2_1^+ \rightarrow 0_1^+)$ values and is not fitted to any additional experimental information. However, there are some gaps and uncertainties in the experimental data: Lifetime values for the 4_1^+ state in ^{116}Te and the 0_2^+ state in ^{120}Te are not available, and there are several differing measurements for the $E2/M1$ mixing ratio of the $2_2^+ \rightarrow 2_1^+$ transitions in ^{118,120}Te.

The most significant discrepancy lies in the observed $\rho^2(E0; 0_2^+ \rightarrow 0_1^+)$ values, which are

predicted to be zero by the U(5) limit of the IBM-1. Wood et al. conclude that the IBM-1 is not suitable for accurately describing E0 transition strengths [19]. They also note that typical $\rho^2(E0; 0_2^+ \rightarrow 0_1^+)$ values for vibrational nuclei near the Z=50 proton shell closure are around $\rho^2(E0; 0_2^+ \rightarrow 0_1^+) \cdot 10^3 = 4$ [19], which do not match the experimental values observed in ^{118,120}Te in this work.

Table 5.2: Comparison of experimental $B(E2)$ and $\rho^2(E0)$ values and model predictions. $B(E2)$ values are given in W.u. and $\rho^2(E0)$ values are given in units of 10^{-3}. The experimental values are mean values from this work and from Refs. [31, 36–38, 74, 75]. The values in column U(5) are calculated using the $B_{4/2}$, $B_{2/2}$ and $B_{0/2}$ ratios given in Sec. 1.1 and normalizing on the respective experimental $B(E2; 2_1^+ \rightarrow 0_1^+)$ value. In column EDF_m preliminary results are presented from calculations in Refs. [85, 86] using the quadrupole collective Hamiltonian based on the results of energy density functionals.

	^{116}Te			^{118}Te			^{120}Te		
	Exp.	U(5)	EDF_m	Exp.	U(5)	EDF_m	Exp.	U(5)	EDF_m
$B(E2; 2_1^+ \rightarrow 0_1^+)$	33(2)	33	50	38(1)	38	43	38(1)	38	39
$B(E2; 4_1^+ \rightarrow 2_1^+)$	-	58	117	70(3)	68	94	61(1)	67	68
$B(E2; 2_2^+ \rightarrow 2_1^+)$	41^{+6}_{-5}	58	55	> 28	68	72	46(2)	67	-
$B(E2; 0_2^+ \rightarrow 2_1^+)$	43^{+6}_{-5}	58	160	90^{+70}_{-30}	68	139	> 19	67	33
$B(E2; 2_2^+ \rightarrow 0_1^+)$	< 0.1	0	2.5	> 0.2	0	1.2	0.6(1)	0	-
$\rho^2(E0, 0_2^+ \rightarrow 0_1^+)$	-	0	85	24^{+18}_{-8}	0	60	> 7	0	32

5.1.6 Evidences for shape coexistence

It is in general not simple to assess shape coexistence. As explained in Sec. 1.2 it is often necessary to look at multiple experimental observables. This requires a lot of experimental data and even though the present results improve the experimental knowledge on mid-shell Te isotopes significantly, experimental data on mid-shell Te isotopes are still more scarce than experimental data in regions, where shape coexistence is well established (e.g. Cd isotopes or Sn isotopes). To gain new insights into shape coexistence in Te isotopes, the experimental findings are first categorized using qualitative signs of shape coexistence presented in Sec. 1.2 that are based on the reviews [5, 14, 15]. Subsequently, a quantitative comparison will be made with very recent calculations performed by Suzuki and Nomura [85].

With the help of the present results, the systematics of the excitation energies of the 0_2^+ and 2_3^+ states were extended beyond mid-shell to ^{116}Te. Minima of both these energies at mid-shell ^{118}Te are confirmed. This behavior is expected for states belonging to intruder structures. In fact, these states have been discussed as possible intruder states already by

Rikovska *et al.* [35].

One of the main goals of this work was the determination of lifetime values of the 0_2^+ states in mid-shell Te isotopes. The information on the lifetimes is necessary for the determination of $\rho^2(E0)$ values. In ^{118}Te and ^{120}Te the E0 transition has been observed by Walker *et al.* [47]. Together with these data a value of $\rho^2(E0; 0_2^+ \to 0_1^+) \cdot 10^3 = 22_{-8}^{+18}$ in ^{118}Te and a lower limit of $\rho^2(E0; 0_2^+ \to 0_1^+) \cdot 10^3 > 7$ in ^{120}Te were determined. Unfortunately, the intensity of the direct E0 transition has not been published in ^{116}Te. The experimental data obtained in this study suggest that the $\rho^2(E0; 0_2^+ \to 0_1^+)$ values in ^{118,120}Te are increased, which may indicate a mixing of two shapes. In fact, similar values (^{112}Cd: $\rho^2(E0; 0_2^+ \to 0_1^+) \cdot 10^3 = 37_{-11}^{+9}$, ^{114}Cd: $\rho^2(E0; 0_2^+ \to 0_1^+) \cdot 10^3 = 19.0(20)$) [20]) are reported in the mid-shell Cd isotopes where the 0_2^+ states are firmly established as intruder states [5].

In this study, upper limits were determined for the lifetimes of the 2_3^+ states in ^{116,118}Te. The upper limit determined for the lifetime of the 2_3^+ state in ^{118}Te agrees with the lifetime of $\tau(2_3^+) = 0.9_{-0.2}^{+0.4}$ ps reported in Ref. [31]. From these data, a lower limit of of $B(E2; 2_3^+ \to 0_2^+) > 20$ W.u. was determined in ^{116}Te and a value of $B(E2; 2_3^+ \to 0_2^+) = 60_{-17}^{+35}$ W.u. was determined in ^{118}Te. These transition strengths are rather large and make the 2_3^+ states in mid-shell Te isotopes candidate states for a first collective 2^+ state built on top of a possibly intruding 0_2^+ state. Unfortunately, the lifetime of the 2_3^+ state in ^{120}Te has not been measured so far.

These observations suggest that there is shape coexistence in mid-shell Te isotopes. However, such an interpretation contradicts an interpretation of mid-shell Te isotopes using the U(5) limit of the IBM-1 that was discussed in the previous section. Specifically, the 0_2^+ state cannot be both a member of the two-phonon triplet of the normal configuration and at the same time belong to an intruder configuration. In order to resolve this apparent contradiction, it is desirable to compare the experimental results also with quantitative predictions of models that include shape coexistence. Such models can be built using very different approaches. The first study of this kind was performed by Rikovska *et al.* [35] using mixed configurations IBM-2 calculations. This study predicted also the resulting level schemes, but many absolute transition strengths were not calculated, including the $B(E2; 0_2^+ \to 2_1^+)$ and $\rho^2(E0; 0_2^+ \to 0_1^+)$ values. The number of fit parameters in the mixed configurations IBM-2 calculations in Ref. [35] is also rather large, limiting the significance of the good agreement of calculated and experimental data. Since then several other studies have predicted shape coexistence in mid-shell Te isotopes but have not included theoretical level schemes and transition strengths [87, 88].

Very recently, a study by Suzuki and Nomura that performed calculations using a quadrupole collective Hamiltonian based on relativistic energy density functionals (EDFs) was published [85]. The results of these calculations are in fact still preliminary and an effort to optimize the calculations is ongoing [86]. The calculations predict shape coexistence in the mid-shell Te isotopes and provide theoretical level energies and transition strengths.

An advantage of these calculations is that — unlike in the case of the IBM-2 calculations performed by Rikovska *et al.* [35] — the experimental data on level energies and transition strengths are not used to fit any model parameters. Instead, the parameters of the quadrupole collective Hamiltonian are "completely determined by the constrained SCMF [self-consistent mean field] calculation employing a relativistic EDF" ([85] p. 2). In their study, Suzuki and Nomura then go on to extensively compare their results on ^{116}Te and ^{118}Te with the experimental data presented in Ref. [70] (also Sec. 4.1) and Ref. [31]. The calculations are in general able to reproduce the experimental level schemes. Absolute transition strengths from their theoretical study are compared to absolute transition strengths obtained from this work in Tab. 5.2. Additionally, the absolute transition strengths from the U(5) limit in the IBM-1 are presented. While the theoretical absolute transition strengths by Suzuki and Nomura [85] lie in the same order of magnitude of the experimental ones, they tend to overestimate the experimental values, especially the $B(E2; 0_2^+ \rightarrow 2_1^+)$ and $\rho^2(E0; 0_2^+ \rightarrow 0_1^+)$ values. This could implicate, that the calculation so far overestimates the influence of shape coexistence or mixing in this region [85].

5.2 Outlook and upcoming experiments

The present data give valuable insight into the nuclear structure of mid-shell tellurium isotopes and provide relevant methods to gain even more information. However, up to now some key questions are still not answered. A clear identification of intruding structures has not been possible, also because alternative approaches to explain experimentally observed excited 0_2^+ states cannot be ruled out. In this section, possible future experiments are presented, that can play a key role to help with the search for such intruding structures and to deepen the understanding of the nuclear structure of mid-shell Te isotopes.

5.2.1 Identification of excited 0⁺ states through β-decay experiments and two-proton transfer experiment

The identification of excited 0^+ states plays a key role in the search for shape coexistence. In their study on intruder states in Te, Rikovska *et al.* [35] regard — in addition to the 0_2^+ and 2_3^+ state — also a 0_3^+ state as a possible intruder state. In contrast to the 0_2^+ state, experimental evidence for the existence of these 0_3^+ and additional data on these 0_3^+ has not increased. They have been identified in ^{120}Te in β decay [47] and n ^{118}Te through (^{3}He,n) reactions [48] and β decay [47]. However, a more recent experiment on ^{120}Te where states were populated in β-decay does not find evidence for a 0_3^+ state and doubts its existence [32]. Also in the present study, the 0_3^+ state in ^{116}Te observed after β decay is found at a higher excitation energy than would be expected based on the 0_3^+ levels in ^{118,120}Te observed by Walker *et al.* [47]. A clarification of the experimental data is thus very desirable. As a first step a measurement of γ rays of ^{118}Te following the β decay of ^{118}I is proposed,

since in this reaction the 0_3^+ was observed by Walker *et al* [47]. A suitable reaction for this experiment is the ^{109}Ag(^{12}C,3n)^{118}I fusion-evaporation reaction with a beam energy 55 MeV that can be provided by the 10 MV FN tandem accelerator at Cologne. A similar experiment can be performed to identify possible intruder states in ^{114}Te, where up to now no such states have been unambiguously identified. The performed experiment on ^{116}Te shows that such experiments are feasible at the FN Tandem accelerator in Cologne if the mother nucleus can be populated with sufficient statistics. The ^{106}Cd(^{11}B,3n)^{114}I reaction with a beam energy of 37 MeV that can be performed at the FN Tandem in Cologne is one possibility to carry out such an experiment. Additionally, in these experiments the critical $E2/M1$ mixing ratios of the $2_2^+ \rightarrow 2_1^+$ and $2_3^+ \rightarrow 2_1^+$ transitions can be measured. For the identification of 0^+ states and the determination of $E2/M1$ mixing ratios, angular correlation measurements employed in this study have proven to be a powerful tool.

Another approach to find excited 0^+ states are (^{3}He,n) reactions to reproduce and improve the findings of Fielding *et al.* [48], possibly with the help of modern γ-ray spectroscopy. The cross sections of excited states in these reactions can also give valuable information on possible shape coexistence as has been shown in similar studies on the Cd and Sn isotopes [14, 89]. In theory, also these types of reactions can be performed at the FN Tandem accelerator in Cologne, even if such experiments have not been tested so far.

5.2.2 Direct measurements of E0 transitions

Experimental information on E0 transitions are especially scarce in the mid-shell Te region. Further measurements of E0 transitions are thus needed to extract $\rho^2(E0)$ values that play a major role for the identification of shape coexistence. Unfortunately, many of the needed conversion electrons have energies too high to be measured at the Cologne Orange. Experiments at other facilities (e.g. the Super-e spectrometer at the Australian National University Heavy Ion Accelerator Facility [90]) are therefore needed.

5.2.3 Measurement of lifetimes of excited states in mid-shell tellurium isotopes in the sub-picosecond range

Many excited states populated in the (^{12}C,^{8}Be) α-transfer reactions showed lifetimes that were too short to be measured with the RDDS method. Many of those lifetime will lie instead in the sub-picosecond regime and are expected to be measurable with the DSA method. Especially the lifetimes of the 2_3^+ states in ^{116,120}Te are of interest as they are candidate states for the intruding structure. The population mechanism of the (^{12}C,^{8}Be) α-transfer reaction also suites DSA experiments, as contributions from delayed feeding are in many cases small. The setup needed for these experiments is the same that was used for the RDDS measurements that can thus be performed at the Cologne CATHEDRAL spectrometer.

Chapter 6

Summary

The aim of this work consisted in finding experimental evidence for shape coexistence in mid-shell ^{116,118,120}Te isotopes. A main focus was the determination of lifetimes of low-lying states, especially of the first excited 0^+ states. For this purpose, the nuclei were populated for the first time in (^{12}C,^{8}Be) α-transfer reactions. Here it was shown that such reactions present a valuable possibility for the determination of lifetimes of such states using Doppler-shift methods. In ^{116,118}Te, lifetime values of the 0_2^+ state were determined, while in ^{120}Te it was possible to determine an upper limit for the lifetime of the 0_2^+ state. Additionally, lifetime values of the 2_1^+ and 2_2^+ states in ^{116}Te and an upper limit of the lifetime of the 2_2^+ state in ^{118}Te were measured. In ^{118}Te, lifetimes of the yrast 2_1^+ and 4_1^+ states were also determined using a fusion-evaporation reaction.

Excited states in ^{116}Te were also populated in β decay from ^{116}I. An analysis of the angular correlations of these data allowed the determination of the spins of many excited states and in particular the first unambiguous identification of excited 0^+ states in ^{116}Te. In addition, for the first time $E2/M1$ mixing ratios of transitions connecting low-lying states in ^{116}Te were determined.

The experimental results obtained in this work agree with the expected signatures of shape coexistence. The energy systematics of the 0_2^+ and 2_3^+ states, which were extended to ^{116}Te in this work, follow a parabolic trend expected for candidate intruder states. The measured $\rho^2(E0; 0_2^+ \to 0_1^+)$ values seem to be enhanced even if the experimental uncertainty of these values is still relatively large. The obtained $B(E2; 0_2^+ \to 2_1^+)$ values can additionally be interpreted as a sign of mixing between the intruding configuration and the normal configuration.

However, the data cannot be treated as conclusive evidence of shape coexistence because they also agree reasonably well with the predictions of the U(5) limit of the IBM-1 that can be associated with an anharmonic vibrator model. For a better understanding of the structure of mid-shell Te isotopes both a theoretical effort to better describe the possible shape coexistence in mid-shell Te isotopes and additional, more precise experimental data can help. Research projects on both of these approaches are currently being carried out.

Appendix A

Detector positions of the used spectrometers

In this work, three different γ-ray spectrometers are used that are presented in Sec. 3.1. The detector positions of these spectrometers are listed in this appendix. The detector positions are given in polar coordinates with the beam axis as the polar axis. The zenith angle is then called Θ and the azimuth angle Φ. For spectrometers that are used for RDDS measurements, the common ring nomenclature is given where detectors with the same zenith angle Θ are grouped into the same ring. Note that the ring 3 in the CATHEDRAL spectrometer consists of Lanthanum-Bromide detectors that are typically not used for RDDS measurements. The angular groups of the HORUS spectrometer and the CATHEDRAL spectrometer used in angular correlation measurements are also presented. The angle of each angular group consisting of $N_{a.g.}$ detector pairs is given as $\theta_{a.g.}$. Some angular groups in the CATHEDRAL spectrometer lie relatively close together and can usually be combined.

Table A.1: Detector positions of the Plunger spectrometer. See text for details.

detector ID	Θ	Φ	ring
0	0°		
1	142°	0°	rng2
2	142°	72°	rng2
3	142°	144°	rng2
4	142°	216°	rng2
5	142°	288°	rng2
6	45°	0°	rng1
7	45°	60°	rng1
8	45°	120°	rng1
9	45°	180°	rng1
10	45°	240°	rng1
11	45°	300°	rng1

Table A.2: Detector positions and angular groups of the HORUS spectrometer. See text for details.

detector positions			angular groups		
Name	Θ	Φ	$\theta_{a.g.}$	$N_{a.g.}$	detector combinations
0	90°	0°	55°	24	[0,1][0,5][0,10][0,13][1,8][1,9]
1	90°	55°			[2,3][2,10][2,11][3,4][3,11][3,12]
2	90°	125°			[4,6][4,7][5,6][5,7][6,10][6,11]
3	90°	180°			[7,12][7,13][8,12][8,13][9,10][9,11]
4	90°	235°	70°	12	[1,2][1,10][1,13][2,11][2,12][4,5]
5	90°	305°			[4,11][4,12][5,10][5,13][10,11][12,13]
6	135°	270°	90°	12	[0,6][0,7][0,8][0,9][3,6][3,7]
7	45°	270°			[3,8][3,9][6,7][6,9][7,8][8,9]
8	45°	90°	110°	12	[1,5][1,11][1,12][2,4][2,10][2,13]
9	135°	90°			[4,10][4,13][5,11][5,12][10,13][11,12]
10	145°	0°	125°	24	[0,2][0,4][0,11][0,12][1,3][1,6]
11	145°	180°			[1,7][2,6][2,7][3,5][3,10][3,13]
12	35°	180°			[4,8][4,9][5,8][5,9][6,12][6,13]
13	35°	0°			[7,10][7,11][8,10][8,11][9,12][9,13]
			180°	7	[0,3][1,4][2,5][6,8]
					[7,9][10,12][11,13]

Table A.3: Detector positions and angular groups of the CATHEDRAL spectrometer. See text for details.

detector positions				angular groups		
detector ID	Θ	Φ	ring	$\theta_{a.g.}$	$N_{a.g.}$	detector combinations
0	30°	240°	rng1	28.96°	12	[0,1][1,2][2,3][3,4][4,5][5,0]
1	30°	300°	rng1			[18,19][19,20][20,21][21,22][22,23][23,18]
2	30°	0°	rng1	31.63°	24	[0,6][0,11][1,6][1,7][2,7][2,8]
3	30°	60°	rng1			[3,8][3,9][4,9][4,10][5,10][5,11]
4	30°	120°	rng1			[12,18][12,19][13,19][13,20][14,20][14,21]
5	30°	180°	rng1			[15,21][15,22][16,22][16,23][17,23][17,18]
6	55°	270°	rng2	48.36 °	12	[6,7][7,8][8,9][9,10][10,11][11,6]
7	55°	330°	rng2			[12,13][13,14][14,15][15,16][16,17][17,12]
8	55°	30°	rng2	51.32°	12	[0,2][0,4][1,3][1,5][2,4][3,5]
9	55°	90°	rng2			[18,20][18,22][19,21][19,23][20,22][21,23]
10	55°	150°	rng2	60.00°	6	[0,3][1,4][2,5][18,21][19,22][20,23]
11	55°	210°	rng2	60.22°	24	[0,7][0,10][1,8][1,11][2,9][2,6]
12	125°	270°	rng4			[3,7][3,10][4,8][4,11][5,9][5,6]
13	125°	330°	rng4			[12,20][12,23][13,18][13,21][14,19][14,22]
14	125°	30°	rng4			[15,20][15,23][16,18][16,21][17,19][17,22]
15	125°	90°	rng4	70.00°	6	[6,12][7,13][8,14][9,15][10,16][11,17]
16	125°	150°	rng4	81.83°	24	[0,8][0,9][1,9][1,10][2,10][2,11]
17	125°	210°	rng4			[3,6][3,11][4,6][4,7][5,7][5,8]
18	150°	240°	rng5			[12,21][12,22][13,22][13,23][14,18][14,23]
19	150°	300°	rng5			[15,18][15,19][16,19][16,20][17,20][17,21]
20	150°	0°	rng5	89.63°	12	[6,13][6,17][7,12][7,14][8,13][8,15]
21	150°	60°	rng5			[9,14][9,16][10,15][10,17][11,16][11,12]
22	150°	120°	rng5	90.37°	12	[6,8][6,10][7,9][7,11][8,10][9,11]
23	150°	180°	rng5			[12,14][12,16][13,15][13,17][14,16][15,17]
LaBr00	90°	270°	rng3	98.17°	24	[0,12][0,17][1,12][1,13][2,13][2,14]
LaBr01	90°	315°	rng3			[3,14][3,15][4,15][4,16][5,16][5,17]
LaBr02	90°	0°	rng3			[6,18][6,19][7,19][7,20][8,20][8,21]
LaBr03	90°	45°	rng3			[9,21][9,22][10,22][10,23][11,23][11,18]
LaBr04	90°	90°	rng3	110.00°	6	[6,9][7,10][8,11][12,15][13,16][14,17]
LaBr05	90°	135°	rng3	119.87°	24	[0,13][0,16][1,14][1,17][2,12][2,15]
LaBr06	90°	180°	rng3			[3,13][3,16][4,14][4,17][5,12][5,15]
LaBr07	90°	225°	rng3			[6,20][6,23][7,18][7,21][8,19][8,22]
						[9,20][9,23][10,18][10,21][11,19][11,22]
				120.00°	6	[0,18][1,19][2,20][3,21][4,22][5,23]
				128.68°	12	[0,19][0,23][1,18][1,20][2,19][2,21]
						[3,20][3,22][4,21][4,23][5,18][5,22]
				131.64°	12	[6,14][6,16][7,15][7,17][8,12][8,16]
						[9,13][9,17][10,14][10,12][11,15][11,13]
				148.37°	24	[0,14][0,15][1,15][1,16][2,16][2,17]
						[3,12][3,17][4,12][4,13][5,13][5,14]
						[6,21][6,22][7,22][7,23][8,18][8,23]
						[9,18][9,19][10,19][10,20][11,20][11,21]
				151.04°	12	[0,20][0,22][1,21][1,23][2,18][2,22]
						[3,19][3,23][4,18][4,20][5,19][5,21]
				180.00°	12	[0,21][1,22][2,23][3,18][4,19][5,20]
						[6,15][7,16][8,17][9,12][10,13][11,14]

Bibliography

[1] M. Göppert-Mayer, "Nuclear Configurations in the Spin-Orbit Coupling Model. I. Empirical Evidence," *Phys. Rev.*, vol. 78, pp. 16–21, Apr 1950.

[2] J. H. D. Jensen, H. E. Suess, and O. Haxel, "Modellmäßige Deutung der ausgezeichneten Nucleonenzahlen im Kernbau," *Naturwissenschaften*, vol. 36, pp. 155–156, May 1949.

[3] A. Bohr and B. Mottelson, *Nuclear Structure II.* Redding: W. A. Benjamin, 1975.

[4] H. Morinaga, "Interpretation of Some of the Excited States of $4n$ Self-Conjugate Nuclei," *Phys. Rev.*, vol. 101, pp. 254–258, Jan 1956.

[5] P. E. Garrett, M. Zielińska, and E. Clément, "An experimental view on shape coexistence in nuclei," *Progress in Particle and Nuclear Physics*, vol. 124, p. 103931, 2022.

[6] A. Arima and F. Iachello, "Collective Nuclear States as Representations of a SU(6) Group," *Phys. Rev. Lett.*, vol. 35, pp. 1069–1072, Oct 1975.

[7] A. Arima and F. Iachello, "Interacting boson model of collective states I. The vibrational limit," *Annals of Physics*, vol. 99, no. 2, pp. 253–317, 1976.

[8] A. Arima and F. Iachello, "Interacting boson model of collective nuclear states II. The rotational limit," *Annals of Physics*, vol. 111, no. 1, pp. 201–238, 1978.

[9] A. Arima and F. Iachello, "Interacting boson model of collective nuclear states IV. The O(6) limit," *Annals of Physics*, vol. 123, no. 2, pp. 468–492, 1979.

[10] F. Iachello and A. Arima, *The interacting boson model.* Cambridge University Press, 1987.

[11] D. D. Warner and R. F. Casten, "Predictions of the interacting boson approximation in a consistent Q framework," *Phys. Rev. C*, vol. 28, pp. 1798–1806, Oct 1983.

[12] J. Kern, P. Garrett, J. Jolie, and H. Lehmann, "Search for nuclei exhibiting the U(5) dynamical symmetry," *Nuclear Physics A*, vol. 593, no. 1, pp. 21–47, 1995.

[13] R. F. Casten, *Nuclear Structure from a Simple Perspective; 2nd ed.* New York, NY: Oxford Univ. Press, 2000.

Bibliography

[14] J. Wood, K. Heyde, W. Nazarewicz, M. Huyse, and P. van Duppen, "Coexistence in even-mass nuclei," *Physics Reports*, vol. 215, no. 3, pp. 101–201, 1992.

[15] K. Heyde and J. L. Wood, "Shape coexistence in atomic nuclei," *Rev. Mod. Phys.*, vol. 83, pp. 1467–1521, Nov 2011.

[16] L. P. Gaffney, M. Hackstein, R. D. Page, T. Grahn, M. Scheck, P. A. Butler, P. F. Bertone, N. Bree, R. J. Carroll, M. P. Carpenter, C. J. Chiara, A. Dewald, F. Filmer, C. Fransen, M. Huyse, R. V. F. Janssens, D. T. Joss, R. Julin, F. G. Kondev, P. Nieminen, J. Pakarinen, S. V. Rigby, W. Rother, P. Van Duppen, H. V. Watkins, K. Wrzosek-Lipska, and S. Zhu, "Shape coexistence in neutron-deficient Hg isotopes studied via lifetime measurements in ^{184,186}Hg and two-state mixing calculations," *Phys. Rev. C*, vol. 89, p. 024307, Feb 2014.

[17] K. Heyde, J. Jolie, J. Moreau, J. Ryckebusch, M. Waroquier, P. Van Duppen, M. Huyse, and J. Wood, "A shell-model description of 0^+ intruder states in even-even nuclei," *Nuclear Physics A*, vol. 466, no. 2, pp. 189–226, 1987.

[18] S. Leoni, B. Fornal, A. Bracco, Y. Tsunoda, and T. Otsuka, "Multifaceted character of shape coexistence phenomena in atomic nuclei," *Progress in Particle and Nuclear Physics*, vol. 139, p. 104119, 2024.

[19] J. Wood, E. Zganjar, C. De Coster, and K. Heyde, "Electric monopole transitions from low energy excitations in nuclei," *Nuclear Physics A*, vol. 651, no. 4, pp. 323–368, 1999.

[20] T. Kibédi, A. Garnsworthy, and J. Wood, "Electric monopole transitions in nuclei," *Progress in Particle and Nuclear Physics*, vol. 123, p. 103930, 2022.

[21] P. E. Garrett, T. R. Rodríguez, A. D. Varela, K. L. Green, J. Bangay, A. Finlay, R. A. E. Austin, G. C. Ball, D. S. Bandyopadhyay, V. Bildstein, S. Colosimo, D. S. Cross, G. A. Demand, P. Finlay, A. B. Garnsworthy, G. F. Grinyer, G. Hackman, B. Jigmeddorj, J. Jolie, W. D. Kulp, K. G. Leach, A. C. Morton, J. N. Orce, C. J. Pearson, A. A. Phillips, A. J. Radich, E. T. Rand, M. A. Schumaker, C. E. Svensson, C. Sumithrarachchi, S. Triambak, N. Warr, J. Wong, J. L. Wood, and S. W. Yates, "Multiple Shape Coexistence in ^{110,112}Cd," *Phys. Rev. Lett.*, vol. 123, p. 142502, Oct 2019.

[22] A. Aprahamian, D. S. Brenner, R. F. Casten, R. L. Gill, and A. Piotrowski, "First observation of a near-harmonic vibrational nucleus," *Phys. Rev. Lett.*, vol. 59, pp. 535–538, Aug 1987.

[23] H. T. Motz, "Slow-Neutron Capture Gamma Rays from Sodium and Cadmium," *Phys. Rev.*, vol. 104, pp. 1353–1364, Dec 1956.

[24] B. L. Cohen and R. E. Price, "Studies of Low-Lying Levels of Even-Even Nuclei with (d,p) and (d,t) Reactions," *Phys. Rev.*, vol. 118, pp. 1582–1590, Jun 1960.

[25] N. Gavrielov, J. E. García-Ramos, P. Van Isacker, and A. Leviatan, "Persistent vibrational structure in $^{110--116}$Cd," *Phys. Rev. C*, vol. 108, p. L031305, Sep 2023.

[26] J. Blachot, "Nuclear Data Sheets for A = 114," *Nuclear Data Sheets*, vol. 113, no. 2, pp. 515–714, 2012.

[27] J. Blachot, "Nuclear Data Sheets for A = 116," *Nuclear Data Sheets*, vol. 111, no. 3, pp. 717–895, 2010.

[28] K. Kitao, "Nuclear Data Sheets Update for A = 118," *Nuclear Data Sheets*, vol. 75, no. 1, pp. 99–198, 1995.

[29] K. Kitao, Y. Tendow, and A. Hashizume, "Nuclear Data Sheets fo A = 120," *Nuclear Data Sheets*, vol. 96, no. 2, pp. 241–390, 2002.

[30] T. Tamura, "Nuclear Data Sheets for A = 122," *Nuclear Data Sheets*, vol. 108, no. 3, pp. 455–632, 2007.

[31] C. Mihai, A. A. Pasternak, S. Pascu, D. Filipescu, M. Ivaşcu, D. Bucurescu, G. C ăta Danil, I. C ăta Danil, D. Deleanu, D. G. Ghiţă, T. Glodariu, N. Mărginean, R. Mărginean, A. Negret, T. Sava, L. Stroe, G. Suliman, and N. V. Zamfir, "Lifetime measurements by the Doppler-shift attenuation method in the ^{115}Sn$(\alpha,n\gamma)^{118}$Te reaction," *Phys. Rev. C*, vol. 83, p. 054310, May 2011.

[32] J. R. Vanhoy, R. T. Coleman, K. A. Crandell, S. F. Hicks, B. A. Sklaney, M. M. Walbran, N. V. Warr, J. Jolie, F. Corminboeuf, L. Genilloud, J. Kern, J.-L. Schenker, and P. E. Garrett, "Structure of ^{120}Te from the ^{118}Sn$(\alpha, 2n\gamma)$ reaction and ^{120}I decay," *Phys. Rev. C*, vol. 68, p. 034315, Sep 2003.

[33] S. F. Hicks, G. K. Alexander, C. A. Aubin, M. C. Burns, C. J. Collard, M. M. Walbran, J. R. Vanhoy, E. Jensen, P. E. Garrett, M. Kadi, A. Martin, N. Warr, and S. W. Yates, "Intruder structures observed in ^{122}Te through inelastic neutron scattering," *Phys. Rev. C*, vol. 71, p. 034307, Mar 2005.

[34] J. Rikovska, N. J. Stone, and P. M. Green, V. R.and Walker, "IBA-2 model calculation on even mass tellurium isotopes compared with results of recent nuclear orientation experiments," *Hyperfine Interactions*, vol. 22, pp. 405–412, Mar 1985.

[35] J. Rikovska, N. Stone, P. Walker, and W. Walters, "Intruder states in even-even Te nuclei," *Nuclear Physics A*, vol. 505, no. 2, pp. 145–172, 1989.

[36] A. A. Pasternak, J. Srebrny, A. D. Efimov, V. M. Mikhajlov, E. O. Podsvirova, C. Droste, T. Morek, S. Juutinen, G. B. Hagemann, M. Piiparinen, S. Törmänen, and A. Virtanen, "Lifetimes in the ground-state band and the structure of $^{1}18$Te," *The European Physical Journal A - Hadrons and Nuclei*, vol. 13, pp. 435–448, Apr 2002.

[37] M. Saxena, R. Kumar, A. Jhingan, S. Mandal, A. Stolarz, A. Banerjee, R. K. Bhowmik, S. Dutt, J. Kaur, V. Kumar, M. Modou Mbaye, V. R. Sharma, and H.-J. Wollersheim, "Rotational behavior of ^{120,122,124}Te," *Phys. Rev. C*, vol. 90, p. 024316, Aug 2014.

[38] F. von Spee, "Lifetimes of excited states in ^{120}Te," Master's thesis, University of Cologne, 2020.

[39] O. Möller, N. Warr, J. Jolie, A. Dewald, A. Fitzler, A. Linnemann, K. O. Zell, P. E. Garrett, and S. W. Yates, "E2 transition probabilities in ^{114}Te: A conundrum," *Phys. Rev. C*, vol. 71, p. 064324, Jun 2005.

[40] J. O. Rasmussen, "Theory of E0 transitions of spheroidal nuclei," *Nuclear Physics*, vol. 19, pp. 85–93, 1960.

[41] A. Dewald, O. Möller, and P. Petkov, "Developing the Recoil Distance Doppler-Shift technique towards a versatile tool for lifetime measurements of excited nuclear states," *Progress in Particle and Nuclear Physics*, vol. 67, no. 3, pp. 786–839, 2012.

[42] T. Alexander and A. Bell, "A target chamber for recoil-distance lifetime measurements," *Nuclear Instruments and Methods*, vol. 81, no. 1, pp. 22–26, 1970.

[43] M. Beckers, A. Dewald, C. Fransen, L. Kornwebel, C.-D. Lakenbrink, and F. von Spee, "Revisiting the measurement of absolute foil-separation for RDDS measurements and introduction of an optical measurement method," *Nuclear Instruments and Methods in Physics Research Section A: Accelerators, Spectrometers, Detectors and Associated Equipment*, vol. 1042, p. 167416, 2022.

[44] A. Sharma, J. Singh, H. Kaur, J. Goswamy, D. Mehta, N. Singh, P. N. Trehan, E. S. Paul, and R. K. Bhowmik, "High spin states in ^{116,118}Te," *Zeitschrift für Physik A Hadrons and Nuclei*, vol. 354, pp. 347–357, Dec 1996.

[45] P. Chowdhury, W. F. Piel, and D. B. Fossan, "Collective properties of $1g_{\frac{9}{2}}$ proton-hole excitations: High-spin states in ^{116,118,120,122}Te and ^{120}Xe nuclei," *Phys. Rev. C*, vol. 25, pp. 813–827, Feb 1982.

[46] B. E. Zimmerman, *The energy level structures of even-even tellurium and odd-odd iodine and antimony nuclei: ^{114}Te, ^{116}Te, ^{114}I, and ^{114}Sb.* PhD thesis, University of Maryland, 1 1992.

[47] P. M. Walker, C. J. Ashworth, I. S. Grant, V. R. Green, J. Rikovska, T. L. Shaw, and N. J. Stone, "E0 transitions in the light tellurium isotopes: evidence for intruder states," *Journal of Physics G: Nuclear Physics*, vol. 13, p. L195, sep 1987.

[48] H. Fielding, R. Anderson, P. Kunz, D. Lind, C. Zafiratos, and W. Alford, "A study of the (^{3}He, n) reaction on isotopes of tin," *Nuclear Physics A*, vol. 304, no. 2, pp. 520–532, 1978.

[49] C. Stahl, J. Leske, C. Bauer, D. Bazzacco, E. Farnea, A. Gottardo, P. R. John, C. Michelagnoli, N. Pietralla, M. Reese, E. Şahin, B. Birkenbach, A. Bracco, F. C. L. Crespi, G. de Angelis, P. Désesquelles, J. Eberth, A. Gadea, A. Görgen, J. Grebosz, H. Hess, J. Jolie, A. Jungclaus, W. Korten, S. M. Lenzi, S. Lunardi, R. Menegazzo, D. Mengoni, V. Modamio, D. R. Napoli, A. Pullia, B. Quintana, F. Recchia, P. Reiter, D. Rosso, M. D. Salsac, P.-A. Söderström, O. Stezowski, C. Theisen, C. A. Ur, and J. J. Valiente-Dobón, "Population of the 2^+_{ms} mixed-symmetry state of ^{140}Ba with the α-transfer reaction," *Phys. Rev. C*, vol. 92, p. 044324, Oct 2015.

[50] O. Tarasov and D. Bazin, "LISE++: Radioactive beam production with in-flight separators," *Nuclear Instruments and Methods in Physics Research Section B: Beam Interactions with Materials and Atoms*, vol. 266, no. 19, pp. 4657–4664, 2008. Proceedings of the XVth International Conference on Electromagnetic Isotope Separators and Techniques Related to their Applications.

[51] H. Bateman, "Solution of a system of differential equations occurring in the theory of radioactive transformations," *Proc. Cambirdge Philos Soc*, vol. 15(V), pp. 423–427, 1910.

[52] A. Dewald, S. Harissopulos, and P. von Brentano, "The differential plunger and the differential decay curve method for the analysis of recoil distance Doppler-shift data," *Zeitschrift für Physik A Atomic Nuclei*, vol. 334, pp. 163–175, Jun 1989.

[53] J. M. Litzinger, *Nuclear structure studies of neutron-rich selenium isotopes*. PhD thesis, Universität zu Köln, München, 2018.

[54] C. Fransen et al., 2024. to be submitted.

[55] S. Zhu and E. McCutchan, "Nuclear Data Sheets for A=214," *Nuclear Data Sheets*, vol. 175, pp. 1–149, 2021.

[56] D. R. Hamilton, "On Directional Correlation of Successive Quanta," *Phys. Rev.*, vol. 58, pp. 122–131, Jul 1940.

[57] M. E. Rose, "The Analysis of Angular Correlation and Angular Distribution Data," *Phys. Rev.*, vol. 91, pp. 610–615, Aug 1953.

[58] R. M. Steffen and K. Alder, *Angular distribution and correlation of gamma rays.* Netherlands: North-Holland, 1975.

[59] S. Robinson, "How reliable are spins and δ-values derived from directional correlation experiments?," *Nuclear Instruments and Methods in Physics Research Section A: Accelerators, Spectrometers, Detectors and Associated Equipment*, vol. 292, no. 2, pp. 386–400, 1990.

[60] J. K. Smith, A. D. MacLean, W. Ashfield, A. Chester, A. B. Garnsworthy, and C. E. Svensson, "Gamma–gamma angular correlation analysis techniques with the GRIFFIN spectrometer," *Nuclear Instruments and Methods in Physics Research Section A: Accelerators, Spectrometers, Detectors and Associated Equipment*, vol. 922, pp. 47–63, 2019.

[61] A. Linnemann, *Das HORUS-Würfelspektrometer und Multiphononanregungen in ^{106}Cd.* PhD thesis, Universität zu Köln, 2006.

[62] L. Netterdon, V. Derya, J. Endres, C. Fransen, A. Hennig, J. Mayer, C. Müller-Gatermann, A. Sauerwein, P. Scholz, M. Spieker, and A. Zilges, "The γ-ray spectrometer HORUS and its applications for nuclear astrophysics," *Nuclear Instruments and Methods in Physics Research Section A: Accelerators, Spectrometers, Detectors and Associated Equipment*, vol. 754, pp. 94–100, 2014.

[63] D. Kocheva, G. Rainovski, J. Jolie, N. Pietralla, C. Stahl, P. Petkov, A. Blazhev, A. Hennig, A. Astier, T. Braunroth, M. L. Cortés, A. Dewald, M. Djongolov, C. Fransen, K. Gladnishki, V. Karayonchev, J. Litzinger, C. Müller-Gatermann, M. Scheck, P. Scholz, R. Stegmann, P. Thöle, V. Werner, W. Witt, D. Wölk, and P. Van Isacker, "Low-lying isovector 2^+ valence-shell excitations of ^{212}Po," *Phys. Rev. C*, vol. 93, p. 011303, Jan 2016.

[64] D. Kocheva, G. Rainovski, J. Jolie, N. Pietralla, A. Blazhev, A. Astier, R. Altenkirch, S. Ansari, T. Braunroth, M. L. Cortés, A. Dewald, F. Diel, M. Djongolov, C. Fransen, K. Gladnishki, A. Hennig, V. Karayonchev, J. M. Keatings, E. Kluge, J. Litzinger, C. Müller-Gatermann, P. Petkov, M. Rudigier, M. Scheck, P. Scholz, P. Spagnoletti, M. Spieker, C. Stahl, R. Stegmann, M. Stoyanova, P. Thöle, N. Warr, V. Werner, W. Witt, D. Wölk, K. O. Zell, P. Van Isacker, and V. Y. Ponomarev, "A revised $B(E2, 2_1^+ \rightarrow 0_1^+)$ value in the semi-magic nucleus ^{210}Po," *The European Physical Journal A*, vol. 53, p. 175, Sep 2017.

[65] V. Karayonchev, J. Jolie, A. Blazhev, A. Dewald, A. Esmaylzadeh, C. Fransen, G. Häfner, L. Knafla, J. Litzinger, C. Müller-Gatermann, J.-M. Régis, K. Schomacker, A. Vogt, N. Warr, A. Leviatan, and N. Gavrielov, "Tests of collectivity in ^{98}Zr by absolute transition rates," *Phys. Rev. C*, vol. 102, p. 064314, Dec 2020.

[66] A. Esmaylzadeh, V. Karayonchev, K. Nomura, J. Jolie, M. Beckers, A. Blazhev, A. Dewald, C. Fransen, R.-B. Gerst, G. Häfner, A. Harter, L. Knafla, M. Ley, L. M. Robledo, R. Rodríguez-Guzmán, and M. Rudigier, "Lifetime measurements to investigate γ softness and shape coexistence in ^{102}Mo," *Phys. Rev. C*, vol. 104, p. 064314, Dec 2021.

[67] A. Esmaylzadeh, V. Karayonchev, G. Häfner, J. Jolie, M. Beckers, A. Blazhev, A. Dewald, C. Fransen, A. Goldkuhle, L. Knafla, and C. Müller-Gatermann, "Triaxiality in the mid-shell nucleus ^{112}Pd," *Phys. Rev. C*, vol. 103, p. 054324, May 2021.

[68] D. Kalaydjieva, D. Kocheva, G. Rainovski, V. Karayonchev, J. Jolie, N. Pietralla, M. Beckers, A. Blazhev, A. Dewald, M. Djongolov, A. Esmaylzadeh, C. Fransen, K. A. Gladnishki, A. Goldkuhle, C. Henrich, I. Homm, K. E. Ide, P. R. John, R. Kern, J. Kleemann, T. Kröll, C. Müller-Gatermann, M. Scheck, P. Spagnoletti, M. Stoyanova, K. Stoychev, V. Werner, A. Yaneva, S. S. Dimitrova, G. De Gregorio, H. Naïdja, and A. Gargano, "Microscopic structure of the one-phonon 2^+ states of ^{208}Po," *Phys. Rev. C*, vol. 104, p. 024311, Aug 2021.

[69] A. Esmaylzadeh, A. Blazhev, K. Nomura, J. Jolie, M. Beckers, C. Fransen, R.-B. Gerst, A. Harter, V. Karayonchev, L. Knafla, M. Ley, and F. von Spee, "Investigation of γ softness: Lifetime measurements in ^{104,106}Ru," *Phys. Rev. C*, vol. 106, p. 064323, Dec 2022.

[70] F. von Spee, M. Beckers, A. Blazhev, A. Dewald, F. Dunkel, A. Esmaylzadeh, C. Fransen, G. Hackenberg, J. Jolie, L. Knafla, C.-D. Lakenbrink, M. Schiffer, N. Warr, and M. Weinert, "Structure of low-lying states in ^{116}Te," *Phys. Rev. C*, vol. 109, p. 024325, Feb 2024.

[71] J. Kumpulainen, R. Julin, J. Kantele, A. Passoja, and E. Verho, "Systematical Study of 0^+ States in $^{116-122}$Te," *JYFL Ann. Rept.*, p. 52, 1986.

[72] S. Juutinen, A. Savelius, P. T. Greenlees, K. Helariutta, P. Jones, R. Julin, P. Jämsen, H. Kankaanpää, M. Muikku, M. Piiparinen, S. Törmänen, and M. Matsuzaki, "Rotational features of vibrator nucleus ^{118}Te," *Phys. Rev. C*, vol. 61, p. 014312, Dec 1999.

[73] B. Saha, *Bestimmung der Lebensdauern kollektiver Kernanregungen in ^{124}Xe und Entwicklung von entsprechender Analysesoftware*. PhD thesis, Universität zu Köln, 2004.

[74] E. A. Cederlöf, T. Bäck, J. Nyberg, C. Qi, A. Ataç, H. Badran, T. Braunroth, T. Calverley, D. M. Cox, M. Doncel, T. Grahn, P. Greenlees, J. Hilton, R. Julin, S. Juutinen, J. Konki, H. Li, S. Matta, V. Modamio, B. S. N. Singh, J. Pakarinen, P. Papadakis, J. Partanen, P. Rahkila, P. Ruotsalainen, M. Sandzelius, J. Sarén,

C. Scholey, S. Stolze, P. Subramaniam, J. Uusitalo, and J. J. Valiente-Dobón, "Lifetime measurement of the yrast 2^+ state in ^{118}Te," *The European Physical Journal A*, vol. 59, p. 300, Dec 2023.

[75] C. B. Li, Y. Zheng, T. X. Li, X. G. Wu, H. Y. Wu, M. Zheng, Z. H. Zhao, Y. Q. Li, R. Hong, Z. Y. He, J. Z. Li, J. L. Wang, C. Y. Guo, Z. X. Zhou, L. Ni, G. S. Li, X. H. Zhou, B. Guo, S. Y. Wang, M. L. Liu, Y. H. Zhang, C. Y. He, F. L. Liu, S. Wang, and L. H. Zhu, "Lifetime measurements of the first 2^+ states in ^{116,118}Te," *Phys. Rev. C*, vol. 109, p. 034310, Mar 2024.

[76] N. Stone, 1985. priv. comm.

[77] F. Kondev, M. Wang, W. Huang, S. Naimi, and G. Audi, "The NUBASE2020 evaluation of nuclear physics properties *," *Chinese Physics C*, vol. 45, p. 030001, mar 2021.

[78] V. Werner, J. R. Terry, M. Bunce, and Z. Berant, "Signatures of shell-effects in collective excitations," *Journal of Physics: Conference Series*, vol. 205, p. 012025, jan 2010.

[79] C. E. Alonso, J. M. Arias, L. Fortunato, N. Pietralla, and A. Vitturi, "Population of mixed-symmetry states via α transfer reactions," *Phys. Rev. C*, vol. 78, p. 017301, Jul 2008.

[80] S. Lalkovski and F. Kondev, "Nuclear Data Sheets for A = 112," *Nuclear Data Sheets*, vol. 124, pp. 157–412, 2015.

[81] J. Katakura and Z. Wu, "Nuclear Data Sheets for A = 124," *Nuclear Data Sheets*, vol. 109, no. 7, pp. 1655–1877, 2008.

[82] A. Dewald, K. Starosta, P. Petkov, M. Hackstein, W. Rother, P. Adrich, A. M. Amthor, T. Baumann, D. Bazin, M. Bowen, A. Chester, A. Dunomes, A. Gade, D. Galaviz, T. Glasmacher, T. Ginter, M. Hausmann, J. Jolie, B. Melon, D. Miller, V. Moeller, R. P. Norris, T. Pissulla, M. Portillo, Y. Shimbara, A. Stolz, C. Vaman, P. Voss, and D. Weisshaar, "Collectivity of neutron-rich palladium isotopes and the valence proton symmetry," *Phys. Rev. C*, vol. 78, p. 051302, Nov 2008.

[83] A. Jungclaus, J. Walker, J. Leske, K.-H. Speidel, A. Stuchbery, M. East, P. Boutachkov, J. Cederkäll, P. Doornenbal, J. Egido, A. Ekström, J. Gerl, R. Gernhäuser, N. Goel, M. Górska, I. Kojouharov, P. Maier-Komor, V. Modamio, F. Naqvi, N. Pietralla, S. Pietri, W. Prokopowicz, H. Schaffner, R. Schwengner, and H.-J. Wollersheim, "Evidence for reduced collectivity around the neutron mid-shell in the stable even-mass Sn isotopes from new lifetime measurements," *Physics Letters B*, vol. 695, no. 1, pp. 110–114, 2011.

[84] M. Doncel, T. Bäck, D. M. Cullen, D. Hodge, C. Qi, B. Cederwall, M. J. Taylor, M. Procter, K. Auranen, T. Grahn, P. T. Greenlees, U. Jakobsson, R. Julin, S. Juutinen, A. Herzán, J. Konki, M. Leino, J. Pakarinen, J. Partanen, P. Peura, P. Rahkila, P. Ruotsalainen, M. Sandzelius, J. Sarén, C. Scholey, J. Sorri, S. Stolze, and J. Uusitalo, "Lifetime measurement of the first excited 2^+ state in ^{112}Te," *Phys. Rev. C*, vol. 91, p. 061304, Jun 2015.

[85] K. Suzuki and K. Nomura, "Shape transition and coexistence in Te isotopes studied with the quadrupole collective Hamiltonian based on a relativistic energy density functional," *arXiv*, 2024.

[86] K. Nomura, 2024. priv. comm.

[87] S. Sharma, R. Devi, and S. Khosa, "Microscopic study of evolution of shape change across even-even mass chain of tellurium isotopes using relativistic Hartree-Bogoliubov model," *Nuclear Physics A*, vol. 988, pp. 9–23, 2019.

[88] D. Bonatsos, K. E. Karakatsanis, A. Martinou, T. J. Mertzimekis, and N. Minkov, "Islands of shape coexistence from single-particle spectra in covariant density functional theory," *Phys. Rev. C*, vol. 106, p. 044323, Oct 2022.

[89] H. Fielding, R. Anderson, C. Zafiratos, D. Lind, F. Cecil, H. Wieman, and W. Alford, "0^+ states observed in Cd and Sn nuclei with the (^{3}He, n) reaction," *Nuclear Physics A*, vol. 281, no. 3, pp. 389–404, 1977.

[90] T. Kibédi, G. Dracoulis, and A. Byrne, "Lens-mode operation of a superconducting electron spectrometer in (HI, xn) reactions," *Nuclear Instruments and Methods in Physics Research Section A: Accelerators, Spectrometers, Detectors and Associated Equipment*, vol. 294, no. 3, pp. 523–533, 1990.

List of publications

[O1] M. Beckers, A. Dewald, C. Fransen, K. Arnswald, C. Müller-Gatermann, and F. von Spee. Development of the multi-purpose Cologne Compact Differential Plunger (CoCoDiff) for the measurement of nuclear level lifetimes with the Recoil Distance Doppler-shift method. *Nuclear Instruments and Methods in Physics Research Section A: Accelerators, Spectrometers, Detectors and Associated Equipment*, 1042:167418, 2022.

[O2] M. Beckers, A. Dewald, C. Fransen, L. Kornwebel, C.-D. Lakenbrink, and F. von Spee. Revisiting the measurement of absolute foil-separation for RDDS measurements and introduction of an optical measurement method. *Nuclear Instruments and Methods in Physics Research Section A: Accelerators, Spectrometers, Detectors and Associated Equipment*, 1042:167416, 2022.

[O3] M. Beckers, C. Müller-Gatermann, K. Arnswald, T. Braunroth, A. Dewald, C. Fransen, A. Goldkuhle, and F. von Spee. Lifetime measurement of the 2_1^+, 4_1^+ states in semi-magic ^{60}Ni. *The European Physical Journal A*, 59(6):129, Jun 2023.

[O4] M. Beckers, C. Müller-Gatermann, A. Blazhev, T. Braunroth, A. Dewald, C. Fransen, A. Goldkuhle, L. Kornwebel, J. Litzinger, F. von Spee, and K.-O. Zell. Lifetime measurement of excited states in ^{144}Ce: Enhanced $E1$ strengths in a candidate for octupole deformation. *Phys. Rev. C*, 102:014324, Jul 2020.

[O5] A. Esmaylzadeh, A. Blazhev, K. Nomura, J. Jolie, M. Beckers, C. Fransen, R.-B. Gerst, A. Harter, V. Karayonchev, L. Knafla, M. Ley, and F. von Spee. Investigation of γ softness: Lifetime measurements in ^{104,106}Ru. *Phys. Rev. C*, 106:064323, Dec 2022.

[O6] A. Goldkuhle, C. Fransen, A. Dewald, K. Arnswald, M. Bast, M. Beckers, A. Blazhev, T. Braunroth, G. Hackenberg, G. Häfner, J. Litzinger, J. Jolie, C. Müller-Gatermann, F. von Spee, N. Warr, D. Werner, and K. O. Zell. Lifetime measurement of excited states in ^{46}Ti. *The European Physical Journal A*, 55(4):53, Apr 2019.

[O7] A. Harter, A. Esmaylzadeh, L. Knafla, C. Fransen, F. von Spee, J. Jolie, M. Ley, V. Karayonchev, J. Fischer, and A. Pfeil. Lifetime measurements in low yrast states and spectroscopic peculiarities in ^{182}Os. *Phys. Rev. C*, 108:024305, Aug 2023.

[O8] G. Jaworski, M. Palacz, A. Goasduff, M. Ciemala, J. Greboszc, M. Kowalczyk, I. Kuti, J. Molnar, N. Toniolo, T. Abraham, A. Astier, M. Beckers, P. Bednarczyk, G. Colucci, F. Dunkel, A. Fijalkowska, C. Fransen, K. Hadynska-Kleka, M. Kisielinski, M. Komorowska, M. Kopec, A. Korgul, J. Kowalska, A. Krako, B. Kruzsicz, P. Kulessa, C. Lakenbrink, M. A., M. Matejska-Minda, M. Matuszewski, N. P.J., A. Nalecz-Jawecki, W. Oklinski, A. Otreba, P. S., C. Petrache, I. Pietka, W. Poklepa, J. Samorajczyk-Pysk, B. Saygi, P. Sekrecka, K. Solak, F. von Spee, A. Stolarz, J. Srebrny, K. Szlezak, A. Spacek, A. Tucholski, and K. Wrzosek-Lipska. Sailing with NEEDLE Beyond the Horizon. *Acta Phys. Polon. Supp.*, 17(3):3–A12, 2024.

[O9] L. Knafla, A. Harter, M. Ley, A. Esmaylzadeh, J.-M. Régis, D. Bittner, A. Blazhev, F. von Spee, and J. Jolie. Improving fast-timing time-walk calibration standards: Lifetime measurement of the 2_1^+ state in ^{152}Gd. *Nuclear Instruments and Methods in Physics Research Section A: Accelerators, Spectrometers, Detectors and Associated Equipment*, 1052:168279, 2023.

[O10] L. Knafla, K. Nomura, A. Esmaylzadeh, A. Harter, J. Jolie, V. Karayonchev, Y. H. Kim, U. Köster, M. Ley, C. Michelagnoli, A. Pfeil, J.-M. Régis, and F. von Spee. Investigating the prolate-to-oblate shape phase transition: Lifetime measurements and γ spectroscopy of the low-lying negative parity structure in ^{193}Os. *Phys. Rev. C*, 109:014313, Jan 2024.

[O11] D. Kocheva, G. Rainovski, J. Jolie, M. Beckers, A. Blazhev, A. Esmaylzadeh, C. Fransen, K. A. Gladnishki, N. Pietralla, M. Scheck, F. von Spee, M. Stoyanova, V. Werner, G. D. Gregorio, A. Gargano, and B. A. Brown. Study the structure of the low-lying states of ^{206}Po. *Physica Scripta*, 99(6):065307, may 2024.

[O12] C.-D. Lakenbrink, M. Beckers, A. Blazhev, A. Dewald, F. Dunkel, A. Esmaylzadeh, C. Fransen, J. Jolie, L. Knafla, C. Müller-Gatermann, F. von Spee, and K.-O. Zell. Lifetime measurement of excited states in ^{116}Xe. *The European Physical Journal A*, 59(12):290, Dec 2023.

[O13] C. Müller-Gatermann, A. Dewald, C. Fransen, M. Beckers, A. Blazhev, T. Braunroth, A. Goldkuhle, J. Jolie, L. Kornwebel, W. Reviol, F. F. von Spee, and K. O. Zell. Evolution of collectivity in ^{118}Xe. *Phys. Rev. C*, 102:064318, Dec 2020.

[O14] C. Müller-Gatermann, A. Dewald, C. Fransen, T. Braunroth, J. Jolie, J. Litzinger, J. M. Régis, F. von Spee, N. Warr, K. O. Zell, T. Grahn, P. T. Greenlees, K. Hauschild, U. Jakobsson, R. Julin, S. Juutinen, S. Ketelhut, P. Nieminen, M. Nyman, P. Peura, P. Rahkila, P. Ruotsalainen, M. Sandzelius, J. Sarén, C. Scholey, J. Sorri, S. Stolze, J. Uusitalo, and P. Petkov. Low-lying electromagnetic transition strengths in ^{180}Pt. *Phys. Rev. C*, 97:024336, Feb 2018.

[O15] F. von Spee, M. Beckers, A. Blazhev, A. Dewald, F. Dunkel, A. Esmaylzadeh, C. Fransen, G. Hackenberg, J. Jolie, L. Knafla, C.-D. Lakenbrink, M. Schiffer, N. Warr, and M. Weinert. Structure of low-lying states in ^{116}Te. *Phys. Rev. C*, 109:024325, Feb 2024.

[O16] C. Müller-Gatermann, F. von Spee, A. Goasduff, D. Bazzacco, M. Beckers, T. Braunroth, A. Boso, P. Cocconi, G. de Angelis, A. Dewald, C. Fransen, A. Goldkuhle, A. Gottardo, A. Gozzelino, K. Hadynska-Klek, G. Jawroski, P. John, J. Jolie, S. Lenzi, J. Litzinger, R. Menegazzo, D. Mengoni, D. Napoli, F. Recchia, M. Siciliano, D. Testov, S. Thiel, J. Valiente-Dobón, and K. Zell. A new dedicated plunger device for the GALILEO γ-ray detector array. *Nuclear Instruments and Methods in Physics Research Section A: Accelerators, Spectrometers, Detectors and Associated Equipment*, 920:95–99, 2019.

[O17] J. Valiente-Dobón, R. Menegazzo, A. Goasduff, D. Agguiaro, P. Aguilera, F. Angelini, M. Balogh, D. Bazzacco, J. Benito, G. Benzoni, N. Bez, M. Bolognesi, S. Bottoni, D. Brugnara, S. Carollo, P. Cocconi, A. Cogo, J. Collado, F. Crespi, A. Ertoprak, R. Escudeiro, F. Galtarossa, E. Gamba, A. Gambalonga, B. G. Servín, A. Gottardo, A. Gozzelino, M. Gulmini, Z. Huang, T. Marchi, D. Mengoni, P. Modanese, D. Napoli, J. Pellumaj, R. Pérez-Vidal, S. Pigliapoco, E. Pilotto, L. Ramina, M. Rampazzo, W. Raniero, M. Rebeschini, K. Rezynkina, D. Rosso, M. Scarcioffolo, D. Scarpa, M. Sedlák, R. Smith, N. Toniolo, F. Veronese, V. Volpe, L. Zago, I. Zanon, G. Zhang, R. Abels, M. Allegrini, C. Aufranc, G. Baulieu, C. Belkhiria, M. Benettoni, D. Benini, M. Bentley, M. Biasotto, M. Blaizot, J. B. Miquel, C. Boiano, A. Boston, H. Boston, A. Boujrad, P. Bourgault, A. Bracco, S. Brambilla, I. Burrows, F. Camera, S. Capra, A. Capsoni, R. Cash, J. Civera, E. Clément, S. Coelli, M. Cordwell, L. Corradi, S. Coudert, G. De Angelis, L. De Ruvo, G. Debras, M. Del Fabbro, J. Diklić, N. Dosme, G. Duchene, B. Duclos, J. Dudouet, J. Eberth, S. Elloumi, C. Everett, S. Fantinel, M. Fillinger, E. Fioretto, C. Fransen, A. Gadea, L. Gibelin, V. González, J. Goupil, C. Görgen, A. Grant, K. Green, J. Ha, T. Hartnett, K. Henseler, H. Hess, R. Hirsch, C. Houarner, J. Jacob, T. Joannem, D. Judson, N. Karkour, M. Karolak, M. Kebbiri, J. Kieffer, M. Labiche, X. Lafay, P. Le Jeannic, A. Lefevre, E. Legay, F. Legruel, S. Lenzi, S. Leoni, D. Linget, M. Liptrot, A. López-Martens, A. Lotodé, L. Manara, L. Ménager, T. Mijatović, B. Million, A. Minarello, G. Montagnoli, P. Morrall, I. Mullacrane, J. Nyberg, G. Philippon, M. Polettini, F. Popieul, A. Pullia, F. Recchia, P. Reiter, G. Richardt, M. Rocchini, A. Roger, F. Saillant, E. Sanchis, M. Laskar, G. Secci, M.-H. Sigward, J. Simpson, N. Solenne, F. von Spee, A. Stefanini, O. Stézowski, S. Szilner, N. Templeton, C. Theisen, S. Thiel, F. Tomasi, S. Tzvetkov, D. Vigano, E. Viscione, O. Wieland, K. Wimmer, G. Wittwer, and M. Zielińska. Conceptual design of the AGATA 2π array at LNL. *Nuclear Instru-*

ments and Methods in Physics Research Section A: Accelerators, Spectrometers, Detectors and Associated Equipment, 1049:168040, 2023.

List of Figures

List of Figures

List of Tables

Danksagungen

Diese Arbeit wäre ohne die Unterstützung vieler nicht möglich gewesen. Deswegen möchte ich all denen danken, die mich in den letzten Jahren inbesonderer Weise begleitet haben.

An erster Stelle möchte ich Prof. Alfred Dewald meinen Dank dafür aussprechen, dass er die Betreuung dieser Arbeit übernommen und mich auch weit in seinen Ruhestand hinein unterstützt hat.

Außerdem danke ich Prof. Reiter und Prof. Schadschneider für ihre Bereitschaft, als Zweitkorrektor und als Vorsitzender des Prüfungsausschusses zur Verfügung zu stehen.

Mein besonderer Dank gilt Dr. Christoph Fransen für die erfahrene Leitung der Plungergruppe, aber auch für unzählige sichtbare und unsichbare Tätigkeiten. Ohne sie hätten weder meine Experimente so durchgeführt werden können, noch wäre diese Arbeit zustande gekommen.

Ein großes Dankeschön geht an Dr. Andrey Blazhev für die pünktliche Fertigstellung vieler komplizierter Targets und an Dr. Claus Müller-Gatermann, der — egal wo gerade er sich auf dem Globus befand — immer als Ansprechpartner für Plungerfragen und Targetfragen zur Verfügung stand.

Prof. Jolie und Dr. Nigel Warr möchte ich für ihre Einblicke in die theoretischeren Seiten der Kernphysik danken und den Operateuren des Tandems für viele Stunden stabilen Strahl und gute Gesellschaft.

Mein Dank gilt auch den ehemaligen (Marcel, Alina und Lisa) und derzeitigen (Casper, Arwin, Felix und Richard) Mitgliedern der Plungergruppe — sowohl für die vielen Diskussionen zum Plungerhandwerk als auch für die Bereitschaft, sich die ein oder andere Nacht für noch eine Tellurmessung um die Ohren zu schlagen. Für die gleiche Bereitschaft, für den selten verwehrten Geleitschutz zum Getränkeautomaten oder Kicker und für die Ratschläge zu Soco und anderen Themen muss ich auch der wechselnden Belegschaft des Kölschkiosks (Mario, Arwin, Lukas, Andreas, Julia und Aaron) danken.

Besonders möchte ich Masha und Heinrich danken. Ihr wart mir eine große Stütze in diesen Jahren und ich hoffe Euch auch weiter als Stütze zu haben wenn wir alle keine Physikdoktoranden mehr sind.

Als letztes möchte ich meiner Familie und vielen Freunden danken, die mich unterstützt haben, die mir zugehört haben auch wenn ich unverständliches erzählt habe und die mir in dieser Zeit oft Zuflucht geboten haben wenn ich mich in Köln nicht mehr konzentrieren konnte.

Erklärung zur Dissertation

Hiermit versichere ich an Eides statt, dass ich die vorliegende Dissertation selbstständig und ohne die Benutzung anderer als der angegebenen Hilfsmittel und Literatur angefertigt habe. Alle Stellen, die wörtlich oder sinngemäß aus veröffentlichten und nicht veröffentlichten Werken dem Wortlaut oder dem Sinn nach entnommen wurden, sind als solche kenntlich gemacht. Ich versichere an Eides statt, dass diese Dissertation noch keiner anderen Fakultät oder Universität zur Prüfung vorgelegen hat; dass sie - abgesehen von unten angegebenen Teilpublikationen und eingebundenen Artikeln und Manuskripten - noch nicht veröffentlicht worden ist sowie, dass ich eine Veröffentlichung der Dissertation vor Abschluss der Promotion nicht ohne Genehmigung des Promotionsausschusses vornehmen werde. Die Bestimmungen dieser Ordnung sind mir bekannt. Darüber hinaus erkläre ich hiermit, dass ich die Ordnung zur Sicherung guter wissenschaftlicher Praxis und zum Umgang mit wissenschaftlichem Fehlverhalten der Universität zu Köln gelesen und sie bei der Durchführung der Dissertation zugrundeliegenden Arbeiten und der schriftlich verfassten Dissertation beachtet habe und verpflichte mich hiermit, die dort genannten Vorgaben bei allen wissenschaftlichen Tätigkeiten zu beachten und umzusetzen. Ich versichere, dass die eingereichte elektronische Fassung der eingereichten Druckfassung vollständig entspricht.

Teilpublikation

- F. von Spee *et al.* "Structure of low-lying states in ^{116}Te".
  Phys. Rev. C 109 024325 (2024)

Die Dissertation beinhaltet die Gewinnung und Analyse von Primärdaten. Diese sind auf den Servern des Instituts für Kernphysik gesichert und auf Anfrage zugänglich.

Köln, den 1. September 2024

_____

(Franziskus Graf von Spee)